博士論文（要約）

Study of novel superconducting states in iron chalcogenides by laser-based angle-resolved photoemission spectroscopy

(レーザー角度分解光電子分光による
鉄カルコゲナイドで発現する新奇な超伝導状態の研究)

橋本　嵩広

本論文は、博士論文「Study of novel superconducting states in iron chalcogenides by laser-based angle-resolved photoemission spectroscopy (レーザー角度分解光電子分光による鉄カルコゲナイドで発現する新奇な超伝導状態の研究)」の第3章、第5章、第6章のうち、近い将来において雑誌掲載の可能性がある部分を除外した内容となっている。

Contents

Introduction

Superconductivity has been a major source of fascinating phenomena and unsolved puzzles in condensed matter physics for more than a century. Unconventional superconductors are superconductors which cannot be explained by a conventional theory for superconductivity, BCS theory, and their superconducting mechanisms have been investigated for a long time. Among unconventional superconductors, iron-based superconductors shed new light on superconductivity by adding another perspective; nematicity. A nematic state breaks rotational symmetry but preserves translational symmetry. The relationship between nematicity and superconductivity attracts interest, however, it was not clear because the antiferromagnetic ordering occurred at a temperature close to a nematic transition in most iron-based superconductors. In an iron chalcogenide superconductor $FeSe_{1-x}S_x$, nematicity appears without magnetic ordering at ambient pressure, making it an ideal material for investigating the relationship between the nematicity and superconductivity.

Angle-resolved photoelectron spectroscopy (ARPES) enables the direct observation of band structures of solids. Incident photons, with energy higher than the work function of a sample, induce photoelectron effect, and by analyzing the kinetic energy and the momentum of the photoelectrons one can directly measure the one-particle spectral function. In particular, we used ultralow temperature and ultrahigh resolution laser-based ARPES (laser ARPES) to probe the electronic structures in the superconducting states of $FeSe_{1-x}S_x$. In this thesis, we explored novel superconducting states arising due to nematicity in $FeSe_{1-x}S_x$.

This thesis is organized as follows. In Chapter 1, we describe basics of conventional and unconventional superconductivity. In Chapter 2, we explain the principles of ARPES, and in Chapter 3, we describe the laser ARPES system used in this thesis. In Chapter 4, we present the superconducting gap anisotropy data of FeSe. The gap anisotropy sensitively depends on the presence of nematic twin domain walls, which suggests time-reversal symmetry breaking around the domain walls. In Chapter 5, we present the substitution dependence of the band dispersions of $FeSe_{1-x}S_x$ in the superconducting states. Evidence of BEC superconductivity is shown, and it was found that the nematicity controls the BCS-BEC crossover in this system. Finally, we present concluding remarks in Chapter 6.

1 Superconductivity

We describe the central phenomenon in this thesis, superconductivity, in this chapter [1, 2]. The conventional flamework of superconductivity called BCS theory is explained in Sec. 1.1 and several important concepts including superconducting gap, Bogoliubov quasiparticle dispersion, and gap equation are introduced. Superconducting gap and Bogoliubov quasiparticle dispersion are observed in this thesis, and are governed by gap equation. In Sec. 1.2, we discuss unconventional superconductivity, which can not be understood by the BCS theory. In Sec. 1.3, we discuss iron-based superconductors. The target material in this thesis, $FeSe_{1-x}S_x$, belongs to them.

1.1 BCS theory

Superconductivity is important for both application and pure scientific sense. Superconducting materials are good for application because of zero resistivity. Researchers try to find superconducting materials with high transition temperature and with other characteristics appropriate for application. Also, superconductivity is interesting for its quantum many-body effect represented by Meissner effect. Therefore, researchers try to understand its mechanism.

In 1911, superconductivity was experimentally discovered by Kamerlingh Onnes in Netherlands. In 1957, it was theoretically explained in BCS theory by Bardeen, Cooper, and Schrieffer. In the BCS theory, electron pairs are created by electron-electron interaction intermediated by phonon, and these electron pairs (Cooper pairs) condensate to superconducting state. The BCS theory gave qualitative explanation for many experimental facts. Here, the electronic state of the BCS theory is explained.

1.1.1 Superconducting gap equation

An attractive interaction is necessary for superconductivity. This comes in only when one takes the motion of the ion cores into account. The physical idea is that the first electron polarizes the medium by attracting positive ions; these excess positive ions in turn attract the second electron, giving an effective attractive interaction between the electrons.

An eigenstate that includes the scattering of two electrons at the Fermi surface (FS) is selected as the ground state. In the BCS theory, only $(\boldsymbol{k}\uparrow, -\boldsymbol{k}\downarrow) \rightarrow (\boldsymbol{k}'\uparrow, -\boldsymbol{k}'\downarrow)$

scatterings are selected. This corresponds to superconductivity by spin singlet Cooper pairing. The BCS approximated Hamiltonian is given by

$$H_{\rm BCS} = \Sigma_{\boldsymbol{k},\sigma}\xi(\boldsymbol{k})c^\dagger_{\boldsymbol{k}\sigma}c_{\boldsymbol{k}\sigma} + \Sigma_{\boldsymbol{k},\boldsymbol{k}'}V(\boldsymbol{k},\boldsymbol{k}')c^\dagger_{\boldsymbol{k}\downarrow}c^\dagger_{-\boldsymbol{k}\uparrow}c_{\boldsymbol{k}'\uparrow}c_{\boldsymbol{k}'\downarrow}, \tag{1.1}$$

where $\xi(\boldsymbol{k}) = \epsilon(\boldsymbol{k}) - \mu$ is the band dispersion of electron, $\epsilon(\boldsymbol{k})$, with respect to the chemical potential, μ. In the BCS theory, $V(\boldsymbol{k},\boldsymbol{k}')$ is an attractive interaction intermediated by phonon. Then, the Hamiltonian is rewritten using the mean field approximation as follows

$$H_{\rm BCS} = \Sigma_{\boldsymbol{k},\omega}\xi(\boldsymbol{k})c^\dagger_{\boldsymbol{k}\omega}c_{\boldsymbol{k}\omega} - \Sigma_{\boldsymbol{k}}(\Delta(\boldsymbol{k})c^\dagger_{-\boldsymbol{k}\downarrow}c^\dagger_{\boldsymbol{k}\uparrow} + \Delta^*(\boldsymbol{k})c_{\boldsymbol{k}\downarrow}c_{-\boldsymbol{k}\downarrow}) + \Sigma_{\boldsymbol{k}}\Delta(\boldsymbol{k})\langle c^\dagger_{-\boldsymbol{k}\downarrow}c^\dagger_{\boldsymbol{k}\uparrow}\rangle, \tag{1.2}$$

where $\Delta(\boldsymbol{k})$ is BCS gap function given by

$$\Delta(\boldsymbol{k}) = -\Sigma_{\boldsymbol{k}'}V(\boldsymbol{k},\boldsymbol{k}')\langle c_{\boldsymbol{k}'\uparrow}c_{-\boldsymbol{k}'\downarrow}\rangle. \tag{1.3}$$

$\Delta(\boldsymbol{k})$ breaks Gauge symmetry, because it changes if Gauge transformation $c \to ce^{i\phi}$, $c^\dagger e^{-i\phi}$ is applied. To diagonalize the Hamiltonian, a linear transformation called Bogoliubov transformation is defined by

$$\begin{cases} \alpha_{\boldsymbol{k}\uparrow} = u_{\boldsymbol{k}}c_{\boldsymbol{k}\uparrow} - v_{\boldsymbol{k}}c^\dagger_{-\boldsymbol{k}\downarrow} \\ \alpha^\dagger_{-\boldsymbol{k}\downarrow} = u_{\boldsymbol{k}}c^\dagger_{-\boldsymbol{k}\downarrow} + v^*_{\boldsymbol{k}}c_{\boldsymbol{k}\uparrow}. \end{cases} \tag{1.4}$$

To fulfill the commutation relation of Fermion, $\{\alpha^\dagger_{\boldsymbol{k}\sigma}, \alpha_{\boldsymbol{k}\sigma}\} = 1$, $u_{\boldsymbol{k}}$ and $v_{\boldsymbol{k}}$ obey the relation

$$u^2_{\boldsymbol{k}} + |v_{\boldsymbol{k}}|^2 = 1. \tag{1.5}$$

The inverse transformation of Eq. (1.4) is substituted to $H_{\rm BCS}$. $H_{\rm BCS}$ is diagonal if

$$2\xi(\boldsymbol{k})u_{\boldsymbol{k}}v^*_{\boldsymbol{k}} - \Delta(\boldsymbol{k})v^{*2}_{\boldsymbol{k}} + \Delta^*(\boldsymbol{k})u^2_{\boldsymbol{k}} = 0. \tag{1.6}$$

Equations (1.5) and (1.6) turn into

$$u^2_{\boldsymbol{k}} = \frac{1}{2}\left[1 + \frac{\xi(\boldsymbol{k})}{E(\boldsymbol{k})}\right], \quad |v^2_{\boldsymbol{k}}| = \frac{1}{2}\left[1 - \frac{\xi(\boldsymbol{k})}{E(\boldsymbol{k})}\right], \tag{1.7}$$

where

$$E(\boldsymbol{k}) = \sqrt{\xi(\boldsymbol{k})^2 + |\Delta(\boldsymbol{k})|^2}. \tag{1.8}$$

The Hamiltonian is diagonalized using Eqs. (1.7) and (1.8) as follows

$$H_{\mathrm{BCS}} = E_{\mathrm{GS}} + \Sigma_{\boldsymbol{k}} E(\boldsymbol{k})(\alpha^\dagger_{\boldsymbol{k}\uparrow}\alpha_{\boldsymbol{k}\uparrow} + \alpha^\dagger_{-\boldsymbol{k}\downarrow}\alpha_{-\boldsymbol{k}\downarrow}), \tag{1.9}$$

where

$$E_{\mathrm{GS}} = \Sigma_{\boldsymbol{k}}[2\xi(\boldsymbol{k})|v_{\boldsymbol{k}}|^2 + 2\Delta(\boldsymbol{k})u_{\boldsymbol{k}}v^*_{\boldsymbol{k}} + \Delta(\boldsymbol{k})\langle c^\dagger_{-\boldsymbol{k}\downarrow}c^\dagger_{\boldsymbol{k}\uparrow}\rangle]. \tag{1.10}$$

In equations (1.9) and (1.10), E_{GS} gives the energy of the vacuum state for the quasiparticle operator $\alpha_{\boldsymbol{k}\sigma}$, and the second term in H_{BCS} gives the excitation energy of a quasiparticle from the vacuum state. Evidently, the energies of these excitations are $E(\boldsymbol{k})$ in Eq. 1.8. $E(\boldsymbol{k})$ is called Bogoliubov quasiparticle dispersion. Thus, $\Delta(\boldsymbol{k})$ plays the role of an energy gap since even at the FS, where $\xi(\boldsymbol{k}) = 0$, $E(\boldsymbol{k}) = |\Delta(\boldsymbol{k})| > 0$.

$|\Psi_{\mathrm{BCS}}\rangle$ is a vacuum of the quasiparticle, and obeys $\alpha_{\boldsymbol{k}\uparrow}|\Psi_{\mathrm{BCS}}\rangle = \alpha_{-\boldsymbol{k}\downarrow}|\Psi_{\mathrm{BCS}}\rangle$. The BCS wave function, therefore, is written as

$$|\Psi_{\mathrm{BCS}}\rangle = \Pi_{\boldsymbol{k}}(u_{\boldsymbol{k}} + v_{\boldsymbol{k}}c^\dagger_{\boldsymbol{k}\uparrow}c^\dagger_{-\boldsymbol{k}\downarrow})|0\rangle\,. \tag{1.11}$$

Next, we will calculate $\Delta(\boldsymbol{k})$. The Bogoliubov quasiparticle is a non-interacting Fermion. The average number of the Bogoliubov quasiparticles is given by the Fermi distribution function $f(E(\boldsymbol{k}))$,

$$\langle\alpha^\dagger_{\boldsymbol{k}\uparrow}\alpha_{\boldsymbol{k}\uparrow}\rangle = \langle\alpha^\dagger_{-\boldsymbol{k}\downarrow}\alpha_{-\boldsymbol{k}\downarrow}\rangle = f(E(\boldsymbol{k})) \equiv 1/(e^{\beta E} + 1), \tag{1.12}$$

where $\beta \equiv 1/k_{\mathrm{B}}T_{\mathrm{c}}$. Here, k_{B} is Boltzmann constant and T_{c} is superconducting transition temperature. Equations (1.4) and (1.12) turn into

$$\langle c_{\boldsymbol{k}\uparrow}c_{-\boldsymbol{k}\downarrow}\rangle = \frac{\Delta(\boldsymbol{k})}{2E(\boldsymbol{k})}\tanh\left[\frac{1}{2}\beta E(\boldsymbol{k})\right]. \tag{1.13}$$

From Eqs. (1.3) and (1.13), we obtain the gap equation

$$\Delta(\boldsymbol{k}) = -\Sigma_{\boldsymbol{k}'}V(\boldsymbol{k},\boldsymbol{k}')\frac{\Delta(\boldsymbol{k}')}{2E(\boldsymbol{k}')}\tanh\left[\frac{1}{2}\beta E(\boldsymbol{k}')\right]. \tag{1.14}$$

The electron-electron interaction is approximated as the average value at the FS as $V(\boldsymbol{k},\boldsymbol{k}') = -V \equiv \langle V(\boldsymbol{k},\boldsymbol{k}')\rangle_{\mathrm{FS}}$. In the BCS theory V is effective attractive interaction

$-V > 0$. Therefore, the superconducting gap equation within the BCS theory is given by

$$\Delta = V\Sigma_{\boldsymbol{k}'} \frac{\Delta}{2E(\boldsymbol{k}')} \tanh\left[\frac{1}{2}\beta E(\boldsymbol{k}')\right], \tag{1.15}$$

note that we assume $\Delta(\boldsymbol{k})$ is momentum independent.

1.1.2 Temperature dependence

To make the BCS superconducting gap equation in Eq. (1.15) easier to handle, we convert the sum along $\boldsymbol{k}$ to an integral along energy. Assuming the range of the integral is within the maximum energy of phonon, $\omega_{\rm D}$, then, we obtain

$$\Delta \cong \lambda \int_{-\omega_{\rm D}}^{\omega_{\rm D}} d\xi \frac{\Delta}{2\sqrt{\xi^2+\Delta^2}} \tanh\left[\frac{1}{2}\frac{\sqrt{\xi^2+\Delta^2}}{k_{\rm B}T}\right]. \tag{1.16}$$

The density of states of electrons, $D(E)$, is approximated as constant, $D(E_{\rm F})$, the value at $E_{\rm F}$, assuming that $\omega_{\rm D}$ is smaller than energy scale of the electrons. $\lambda \equiv VD(E_{\rm F})$ is a dimensionless interaction.

We will determine $T_{\rm c}$, below which Δ is finite. The both sides Eq. (1.16) are divided by Δ, and $\Delta \to 0$, then, we obtain

$$1 \cong \lambda \int_0^{\omega_{\rm D}} d\xi \frac{1}{\xi} \tanh\left[\frac{1}{2}\frac{\xi}{k_{\rm B}T_{\rm c}}\right] \cong \lambda \log\left(\frac{2\gamma\omega_{\rm D}}{\pi k_{\rm B}T_{\rm c}}\right). \tag{1.17}$$

In calculating the integral in Eq. (1.17), variable conversion $x \equiv \xi/2k_{\rm B}T_{\rm c}$ is used for a partial integration, and we assumed

$$k_{\rm B}T_{\rm c} << \omega_{\rm D}, \tag{1.18}$$

and we also used the following approximation

$$\int_0^{\omega_{\rm D}/2k_{\rm B}T_{\rm c}} dx \frac{\log x}{\cosh^2 x} \cong \int_0^{\infty} \frac{\log x}{\cosh^2 x} = -\log\frac{4\gamma}{\pi}, \tag{1.19}$$

where $\log\gamma = 0.577\cdots$ is the Euler's constant. $T_{\rm c}$ is finite only when the interaction is attractive ($\lambda < 0$), and it is given by

$$k_{\rm B}T_{\rm c} = 1.13\omega_{\rm D} \exp\left(-\frac{1}{\lambda}\right). \tag{1.20}$$

Then, we will calculate the superconducting gap at zero temperature, $\Delta_0 \equiv \Delta(T=0)$. Putting $T=0$ in Eq. (1.16) and conducting similar algebra as above, one obtains

$$1 = \lambda \int_{-\omega_{\rm D}}^{\omega_{\rm D}} \frac{d\xi}{2\sqrt{\xi^2+\Delta_0^2}} \cong \lambda \log \frac{2\omega_{\rm D}}{\Delta_0}. \tag{1.21}$$

Therefore, Δ_0 is given by

$$\Delta_0 = 2\omega_{\rm D} \exp\left(-\frac{1}{\lambda}\right) \tag{1.22}$$

By considering equations (1.20) and (1.22), we can conclude an universal relation between Δ_0 and $T_{\rm c}$,

$$\frac{2\Delta_0}{k_{\rm B}T_{\rm c}} = 3.53. \tag{1.23}$$

For example, if $T_{\rm c} = 10$ K, $\Delta_0 = 1.5$ meV since $k_{\rm B} = 0.086$ meV/K.

The temperature dependence of Δ is calculated numerically from Eq.(1.16). Physically speaking, Δ is almost constant until a significant number of quasiparticles are thermally excited. On the other hand, near $T_{\rm c}$, $\Delta(T)$ drops to zero with a vertical tangent, approximately as

$$\frac{\Delta(T)}{\Delta_0} \approx 1.74\sqrt{1-\frac{T}{T_{\rm c}}} \quad (T \approx T_{\rm c}). \tag{1.24}$$

Numerical calculation and approximation near $T_{\rm c}$ for $\Delta(T)$ are shown in Fig. 1.1(a).

Table (1.1) shows a comparison between $T_{\rm c}$ and the temperature scale of $\omega_{\rm D}$, $T_{\rm D}$. We can confirm that the assumption in inequality (1.18) is valid.

Table 1.1: $T_{\rm c}$ and $T_{\rm D}$ for elemental metals

Material	$T_{\rm c}$ (K)	$T_{\rm D}$ (K)
Al	1.14	428
Sn	3.72	200
Nb	9.50	275

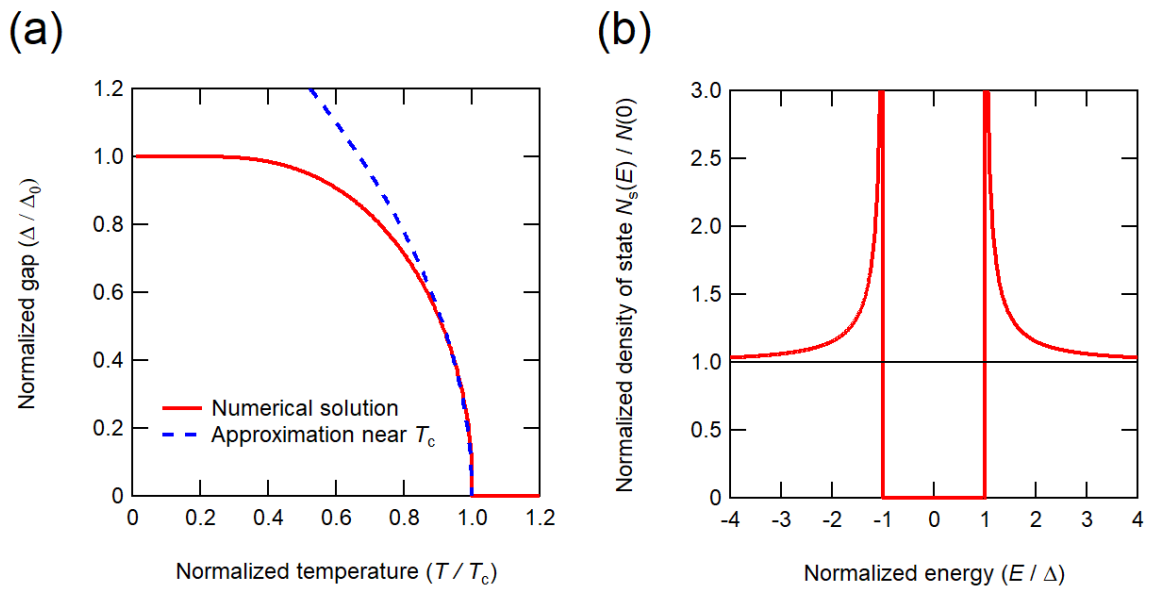

Figure 1.1: Characteristic of the BCS theory: (a) Temperature dependence of the superconducting gap, Δ. The red line is the numerical solution of Eq. (1.16). The blue dotted line is the approximation near T_c shown in Eq. (1.24). (b) Density of states in the superconducting state shown in Eq. (1.26).

1.1.3 Density of states

In Sec. 1.1, we have seen that the quasiparticle excitations can be simply described as fermions created by the $\alpha^\dagger$, which are equivalent of the $c^\dagger$ in the normal state. The density of states in the superconducting state, $N_s(E)$ and that in the normal state, $N_n(\xi)$, therefore, have following relation

$$N_s(E)dE = N_n(\xi)d\xi. \tag{1.25}$$

Within a few milli-electron volts from E_F, we can take $N_n = N(0)$, a constant. This leads directly to the simple result

$$\frac{N_s(E)}{N(0)} = \frac{d\xi}{dE} = \begin{cases} \frac{|E|}{\sqrt{E^2-\Delta^2}}, & (|E| > \Delta) \\ 0, & (|E| < \Delta). \end{cases} \tag{1.26}$$

with a gap of 2Δ in the density of states. Of course, the total number of states is conserved because of the one-to-one correspondence between the $\alpha^\dagger$ and the $c^\dagger$. The density of states is shown in Fig. 1.1(b).

1.2 Unconventional superconductivity

In the BCS theory described so far, the spin singlet Cooper pair has no momentum dependence of the superconducting gap. Here, we discuss various unconventional superconductors, which cannot be explained by BCS theory.

1.2.1 Symmetry of wave function of Cooper pairs

A Cooper pair is made up of two electrons, which are Fermions, therefore, the sign of its wave function is reversed when two electrons are exchanged. Since the wave function consists of an orbital part and a spin part, either one is symmetric and the other is antisymmetric.

The orbital part is classified like s-wave, p-wave, d-wave, and f-wave, using the orbital classification by angular momentum in atomic orbitals. s-wave and d-wave are symmetric, and p-wave and f-wave are antisymmetric. Other than the s-wave, the superconducting gap functions have zero points in momentum space, which are called nodes. Since these nodes are required by symmetry, the position of the nodes do not change unless the symmetry of the wave function is changed. Adding to this, superconducting gap function may have anisotropy due to the details of the interaction that forms the Cooper pair. If the node is not required by symmetry, it is called accidental node. Nodes are classified into point nodes and line nodes, depending on the distribution in momentum space.

Since each electron has spin 1/2, the spin part is either an anti-symmetric spin singlet

$$\frac{1}{\sqrt{2}}(|\uparrow\downarrow\rangle - |\downarrow\uparrow\rangle), \tag{1.27}$$

or symmetric spin triplet

$$\begin{cases} |\uparrow\uparrow\rangle \\ \frac{1}{\sqrt{2}}(|\uparrow\downarrow\rangle + |\downarrow\uparrow\rangle) \\ |\downarrow\downarrow\rangle\,. \end{cases} \tag{1.28}$$

Symmetry of orbital and spin parts of wave function is summarized in Tab. 1.2.

Table 1.2: Symmetry of wave function of Cooper pairs.

Orbital	Spin
s, d-wave (symmetric)	singlet (antisymmetric)
p, f-wave (antisymmetric)	triplet (symmetric)

1.2.2 Determination of gap function

Density of states has a gap at $E_{\rm F}$ in a full gap s-wave superconductor as shown in Fig. 1.1(b), while it has a linear energy dependence $N_{\rm s}(E)/N(0) \propto |E|$ in the presence of line nodes. This difference is used to distinguish between full gap and nodal gap states. Several ways of determining the presence of superconducting gap nodes are summarized in Tab. 1.3. The tunneling spectrum measured by scanning tunneling spectroscopy (STS) around zero bias reflects density of states. The presence of a residual value in thermal conductivity divided by temperature, κ/T, at $T \to 0$, κ_0/T, indicates the presence of normal fluid, which can be attributed to the presence of line nodes in the gap function [3]. In other experiments, thermally activated behavior ($\sim \exp(-\Delta/k_{\rm B}T)$) suggests a full gap state, and T-linear (or T^2) temperature dependence suggests the presence of line nodes [4]. It should be noted that accidental nodes can disappear for several reasons including impurity [5] and time-reversal symmetry breaking around twin boundaries [6] (see Sec. 4.1.5 for details).

Table 1.3: Superconducting nodes determined by several properties. The tunneling spectra determined by STS, dI/dV, the thermal conductivity divided by temperature, κ/T, at $T \to 0$, κ_0/T [3], the temperature dependent part of the London penetration depth, $\Delta\lambda(T) = \lambda(T) - \lambda(0)$ [4], the electronic Sommerfeld coefficient, $\gamma = C_{\rm el}/T$, where $C_{\rm el}$ is the electronic specific heat, and the NMR nuclear-spin-lattice relaxation rate, $1/T_1T$, are listed. ω_0 is the nonzero nuclear resonance frequency.

Observable	Full gap	Line nodes
dI/dV	U-shape	V-shape
κ_0/T	zero	finite
$\Delta\lambda$	$(\Delta_0/k_{\rm B}T)^{1/2}\exp(-\Delta_0/k_{\rm B}T)$	T
γ	$(\Delta_0/k_{\rm B}T)^{5/2}\exp(-\Delta_0/k_{\rm B}T)$	T
$1/T_1T$	$(\Delta_0/k_{\rm B}T)\ln(k_{\rm B}T/\omega_0)\exp(-\Delta_0/k_{\rm B}T)$	T^2

The angular dependence of superconducting gap and the positions of nodes can be determined by Bogoliubov quasiparticle interference (BQPI) measured by scanning tunneling microscopy [7], magnetic field angle-resolved specific heat measurements [8], and angle-resolved photoemission spectroscopy (ARPES). In multiband superconductors, the assignment of energy bands and superconducting gaps is nontrivial in BQPI and angle-resolved specific heat measurements. In this sense, ARPES is the most direct probe to determine superconducting gap anisotropy (see Chap. 2 for details).

Experimental techniques for determining the symmetry of the wave function of the spin part of a Cooper pair include NMR Knight shift and the measurement of the upper critical magnetic field. In the case of spin singlet superconductivity, the Knight shift decreases below T_c. On the other hand, in the case of spin triplet superconductivity, the Knight shift may be anisotropic with respect to the magnetic field below T_c.

The upper critical magnetic field is determined by the orbital effect due to Lorentz force, and the Pauli paramagnetic effect due to Zeeman splitting. In the case of spin triplet superconductivity, suppression of superconductivity due to the Pauli paramagnetic effect does not work. Therefore, confirmation of the Pauli paramagnetic effect is against the spin-triplet superconductivity.

1.2.3 Spin fluctuations

In BCS theory, we considered the phonon-mediated attractive interaction between electrons as the Cooper pair scattering, $V(\boldsymbol{k}, \boldsymbol{k}')$ in Eq. (1.1). If $V(\boldsymbol{k}, \boldsymbol{k}')$ is isotropic, $\Delta(\boldsymbol{k})$ has no momentum dependence. On the other hand, if $V(\boldsymbol{k}, \boldsymbol{k}')$ is repulsive, $\Delta(\boldsymbol{k})$ has anisotropy. $\Delta(\boldsymbol{k})$ is determined by the gap equation described in Eq. (1.14)

$$\Delta(\boldsymbol{k}) = -\Sigma_{\boldsymbol{k}'} V(\boldsymbol{k}, \boldsymbol{k}') \frac{\Delta(\boldsymbol{k}')}{2E(\boldsymbol{k}')} \tanh\left[\frac{1}{2}\beta E(\boldsymbol{k}')\right]. \tag{1.29}$$

If $V(\boldsymbol{k}, \boldsymbol{k}') > 0$, $\Delta(\boldsymbol{k})$ must change its sign depend on $\boldsymbol{k}$.

In cuprate superconductors, when moving the FS by $\boldsymbol{q} = \boldsymbol{k}' - \boldsymbol{k} \sim (\pi, \pi)$, it almost overlaps the original one. This is called nesting, and $\boldsymbol{q}$ is called nesting vector. For this $\boldsymbol{q}$, antiferromagnetic fluctuation is strong and $V(\boldsymbol{k}, \boldsymbol{k}')$ has a large value. Therefore, the sign of $\Delta(\boldsymbol{k})$ changes between $\boldsymbol{q} \sim (\pi, \pi)$ and d-wave superconductivity solution is obtained.

1.2.4 Unconventional superconducting materials

Examples of unconventional superconductors are explained in the following.

Cuprate superconductors have high T_c higher than the boiling point of liquid nitrogen (77 K). They have layered structures and the parent material is Mott insulators. One $3d$ orbital of copper constitutes the FS. d-wave superconductivity due to spin fluctuations is generally supported. Iron-based superconductors have layered structures similar to cuprate superconductors, and the spin degree of freedom is related to superconductivity. We describe them in detail in Sec. 1.3.

Heavy Fermion superconductors are a group of compounds containing cerium and uranium. Many have an antiferromagnetic phase or a superconducting phase adjacent

to the ferromagnetic phase. Because of its narrow bandwidth, it is called a “heavy” electron system. Heavy Fermion superconductor $CeCu_2Si_2$ has long been believed to be a d-wave superconductor, but recent evidence is against it [9].

Recently, topological superconductivity is attracting attention [10, 11]. Also, superconductivity was found in "magic angle" twisted bilayer graphene [12] and quasicrstal [13]. Ruthenium oxide Sr_2RuO_4 has been considered to be a triplet p-wave superconductor, but recent reports denies this understanding [14]. Although it is explained within the conventional flamework of superconductivity, the superconducting material with the highest T_c to date is $LaH_{10\pm x}$, which becomes superconducting at 260 K under pressure of 190 GPa [15, 16].

1.3 Iron-based superconductors

The target material in this thesis, $FeSe_{1-x}S_x$, belongs to iron-based superconductors. We explain several important properties of this material group in this section.

1.3.1 Basic properties

Research on iron-based superconductors begins with the discovery of superconductivity in LaFePO by the Hosono group in 2006 [17]. In a short period, the maximum value of T_c rose to 26 K in $LaFeAsO_{1-x}F_x$ [18].

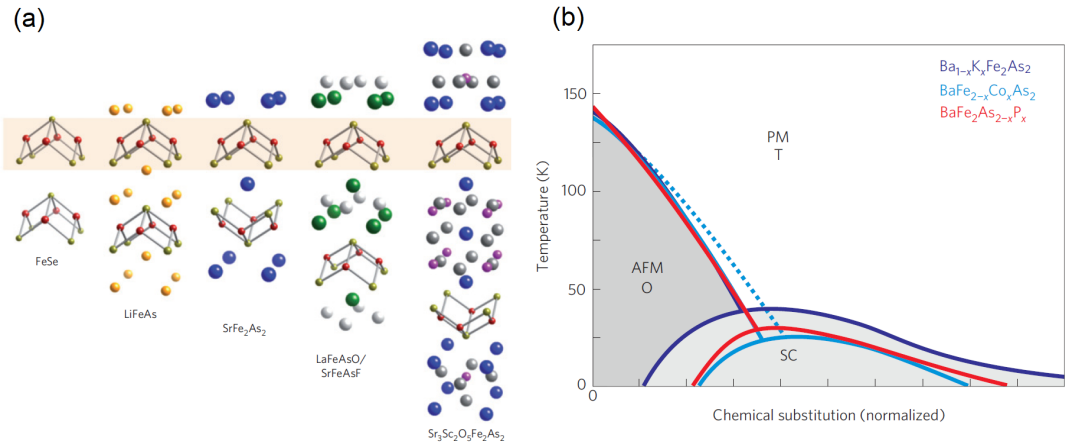

Figure 1.2: Crystal structure and phase diagram of iron-based superconductors [19]. (a) Crystal structure. Fe ions are shown in red and pnictogen/chalcogen anions are shown in gold. (b) Typical phase diagram. Each phase is paramagnetic (PM), tetragonal (T), orthorhombic (O), antiferromagnetic order (AFM), and superconducting phase (SC).

The crystals have layered structures, as shown in Fig. 1.2(a). A two-dimensional plane composed of Fe and pnictogen or chalcogen (Fe-Se (As) layer) is a basic component, and iron-based superconductors are classified according to the number and arrangement of atoms between the layers. A major difference from cuprate superconductors is that multiple Fe $3d$ orbitals are involved in low-energy electronic structures. Although T_c is lower than cuprate superconductors, the role of this multi-orbital property in superconductivity has attracted interests. Figure 1.2(b) shows a typical phase diagram. The high-temperature phase of the parent material is paramagnetic and tetragonal, and the low-temperature phase is orthorhombic with antiferromagnetic order. Chemical substitution suppresses the antiferromagnetic phase and the superconducting phase grows.

1.3.2 Unit cell

Since it is confusing how a unit cell is determined in iron-based superconductors, a brief explanation is given in the following. Figure 1.3(a) shows a typical Fe-Se (As) layer seen from above (c-axis). Se (As) atoms are located above and below the Fe layer, so the unit cell contains two Fe atoms (2 Fe/unit cell). However, a unit cell containing only one Fe atom (1 Fe/unit cell) is also used for simplicity. The Brillouin zone (BZ) of the 2 Fe/unit cell is half the size of that of 1 Fe/unit cell. If antiferromagnetic order exists, one can take AF unit cell and corresponding BZ. Note that in orthorhombic state, the number of Fe atoms in the unit cell does not change.

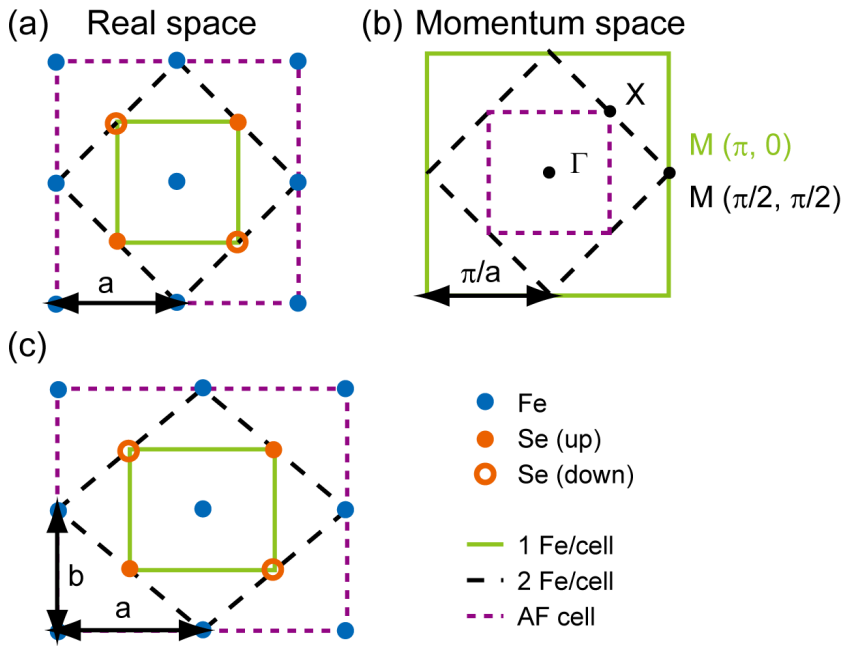

Figure 1.3: Unitcell of iron-based superconductors. 1 and 2 Fe/unit cells, and antiferromagnetic (AF) unit cell are shown. (a) Fe-Se (As) layer seen from above. (b) Corresponding BZ. (c) Same as (a) but in the orthorhombic state ($a > b$).

1.3.3 Superconducting gap symmetry

Figure 1.4 shows candidates for superconducting gap symmetry in iron-based superconductors. $s_{\pm}$-wave superconductivity mediated by spin fluctuations have attracted attention from the beginning. If dominant paring interaction is mediated by spin fluctuation with $\boldsymbol{q} = (\pi, 0), (0, \pi)$, (see Sec. 1.2.3 for details), the gap function has different signs at the hole FS around Γ point and the electron FS around M point. Since iron-based superconductors have multiple Fe $3d$ orbitals near the Fermi level, the electronic structure near the FS changes sensitively depending on the elemental composition and crystal structure, and the gap function depends on material. Therefore, nodal $s_{\pm}$-wave or d-wave are also possible. Nodal $s_{\pm}$-wave is similar to $s_{\pm}$-wave but accidental nodes appear. If orbital fluctuation is dominant, the gap symmetry is s_{++}-wave.

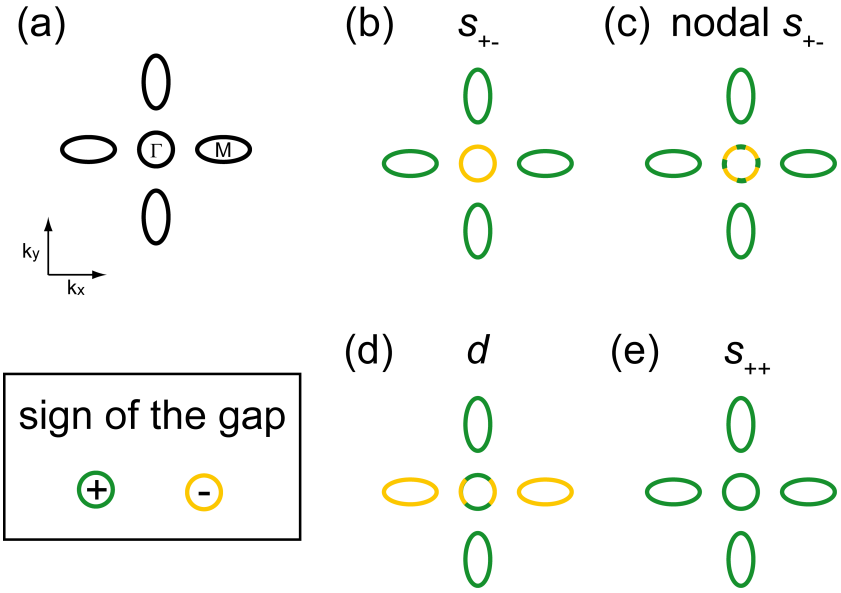

Figure 1.4: Candidates of superconducting gap symmetry in iron-based superconductors. The sign of superconducting gap is color-coded in green (positive) and yellow (negative). (a) FS of a typical iron-based superconductor, consisting of a hole surface around the Γ point and an electron FS around the M point in the BZ. (b) $s_{\pm}$-wave. (c) Nodal $s_{\pm}$-wave. (d) d-wave. (e) s_{++}-wave.

An early study of iron-based superconductors by Kuroki *et. al.*, proposed superconductivity by spin fluctuations (Fig. 1.5) [20]. Five Fe $3d$ orbitals are used to construct a minimal model for $LaFeAsO_{1-x}F_x$. As shown in Fig. 1.5(b), spin fluctuations develop at $\boldsymbol{q} \sim (\pi, 0), (0, \pi)$, and the sign of the superconducting gap changes between the hole FS at the Γ point and the electron FS at the M point. It was supposed to be $s_{\pm}$-wave. Similar superconductivity due to spin fluctuations was also proposed by Mazin *et. al.* [21]. Superconducting gap with $s\pm$-wave symmetry is supported by experiments including scanning tunneling microscopy measurements[22] and inelastic neutron scattering [23]. Adding to spin fluctuations, importance of orbital fluctuations is pointed out [24]. Sev-

eral ARPES reports suggest that orbital fluctuations participate in superconducting pairing [25, 26].

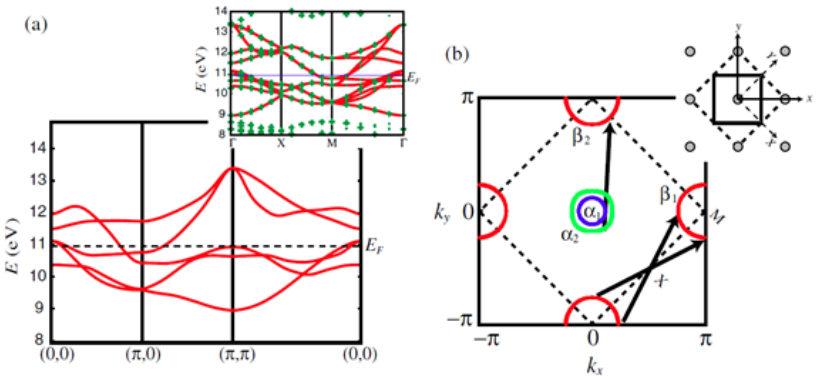

Figure 1.5: Minimal model of band structure and spin fluctuation in $LaFeAsO_{1-x}F_x$ [20]. (a) The band structure of the five-band model in the unfolded BZ, where the interlayer hoppings are included. (b) FS, with the arrows indicating the nesting vectors.

1.3.4 Nematicity

Nematic state is a state that breaks rotational symmetry but preserves translational symmetry [27]. By analogy with classical nematicity in liquids of rod-like molecules, the homogeneous anisotropic phase of strongly quantum mechanical systems is said to be an electronic nematic phase. A metal that undergoes a transition from a tetragonal to an orthorhombic or from an orthorhombic to a monoclinic crystal structure has undergone a nematic transition according to this definition. When the driving force for the symmetry change comes from interesting electronic physics, and especially where the effects of the symmetry breaking are much more pronounced on the electronic structure than on the crystalline structure, the perspective of nematicity is appropriate. Nevertheless, symmetry breaking in the electron fluid necessarily implies symmetry breaking in the crystal structure and vice versa. Nematicity has been observed in two-dimensional electron systems under high magnetic fields, in strontium ruthenate materials, and in cuprate superconductors.

Nematicity is also observed in iron-based superconductors [28]. The resistivity anisotropy induced by an externally imposed lattice distortion (applied to a sample via a piezo stack) was measured [29]. As shown in Fig. 1.6, indeed, the susceptibility of an electronic nematic order parameter diverges on approaching T_s from above, in agreement with the assumption that it drives the structural transition. The nematic susceptibility has been evaluated by various techniques, including the above-described elastoresistivity, the stress-dependent optical reflectivity, the elastic shear modulus and the Raman response.

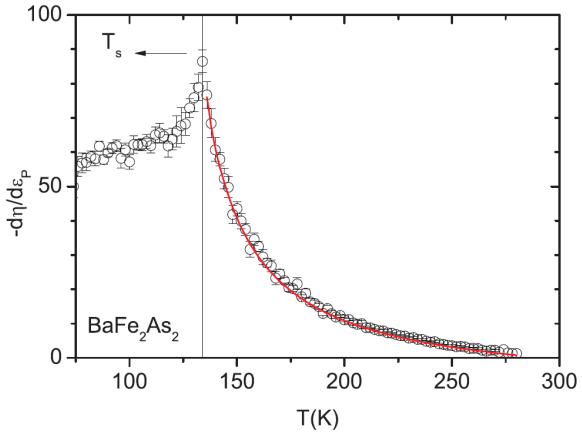

Figure 1.6: Temperature dependence of the nematic response $d\eta/d\varepsilon_P$ of $BaFe_2As_2$ measured by elastoresistivity [29]. Vertical line indicates the structural transition temperature $T_s = 138$ K. Red line shows fit to mean field model. There is no evidence for any additional phase transitions for temperatures above T_s.

2 Angle-resolved photoemission spectroscopy

Angle-resolved photoemission spectroscopy (ARPES) is a powerful probe in condensed matter physics which allows direct observation of band structure in crystals. In this chapter, we describe the principle of ARPES and its experimental details [30–32].

2.1 Principle

Photoemission spectroscopy is based on photoelectric effect. The phenomenon of photoemission was detected by H. Hertz in 1887, and A. Einstein theoretically explained this phenomenon in 1905.

The energy diagram in a sample and a photoemission spectrum is shown in Fig. 2.1. The electrons excited by photoelectric effect are analyzed by their kinetic energy, E_k. Knowing the energy of the light, $\hbar\omega$, and the work function, Φ, one can determine the binding energy of the electron in the sample, $E_{\rm B}$, from the following conservation of energy

$$E_k = \hbar\omega - \Phi - |E_{\rm B}|. \tag{2.1}$$

Photoemission spectroscopy is, therefore, an appropriate probe to observe the band structure in crystals.

2.2 Photoemission process

To understand the photoemission process, one has to calculate the transition probability, w_{fi}, for an optical excitation between the N-electron ground state, Ψ_i^N, and one of the possible final state, Ψ_f^N. This probability is approximated by Fermi's golden rule:

$$w_{fi} = \frac{2\pi}{\hbar} |\, \langle \Psi_f^N | H_{\rm int} | \Psi_i^N \rangle \,|^2 \delta(E_f^N - E_i^N - \hbar\omega), \tag{2.2}$$

where $E_i^N = E_i^{N-1} - |E_{\rm B}^{\boldsymbol{k}}|$ and $E_f^N = E_f^{N-1} + E_k$ are the energy of the initial and the final states of the N-electron system, respectively, and $E_{\rm B}^k$ is the binding energy of

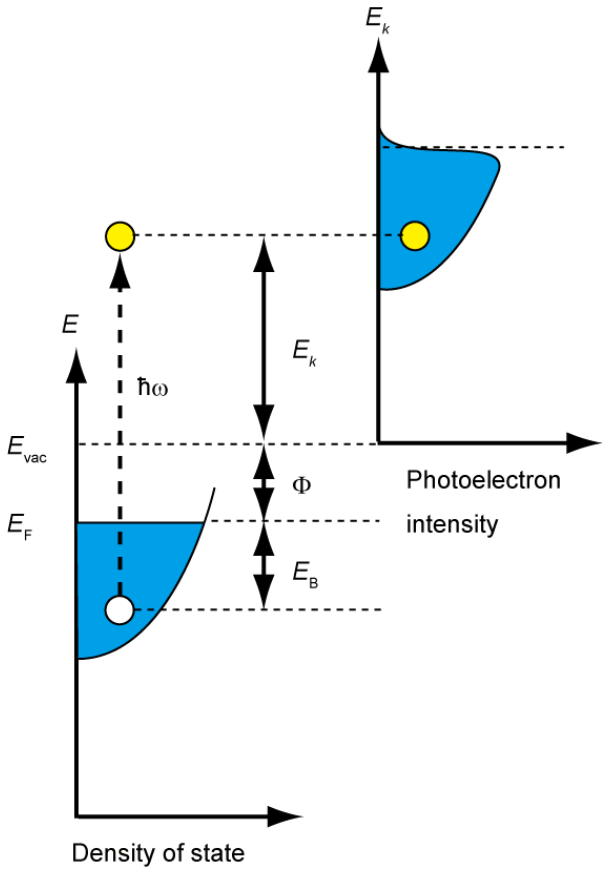

Figure 2.1: Relation between the energy levels in a crystal and the electron energy distribution produced by a photon. See text for details of parameters in the image.

the photoelectron with kinetic energy E_k and momentum $\boldsymbol{k}$. The interaction with the photon is treated as a perturbation theory with the Hamiltonian shown as

$$H_{\text{int}} = -\frac{e}{2mc}(\boldsymbol{A}\cdot\boldsymbol{p}+\boldsymbol{p}\cdot\boldsymbol{A}) = -\frac{e}{mc}\boldsymbol{A}\cdot\boldsymbol{p}, \tag{2.3}$$

where $\boldsymbol{p}$ is the operator of electron momentum and $\boldsymbol{A}$ is the electromagnetic vector potential. Here, scalar potential is chosen to be zero, and quadratic term in $\boldsymbol{A}$ is negligible compared to the linear terms in the linear optical regime. In obtaining Eq. (2.3), the commutation relation, $[\boldsymbol{p},\boldsymbol{A}] = -i\hbar\boldsymbol{\nabla}\cdot\boldsymbol{A}$, and dipole approximation, $\boldsymbol{\nabla}\cdot\boldsymbol{A} = 0$, were used.

For the remaining procedure, one of the methods to treat is so called *one-step model*. In this method, light absorption, photoelectron excitation, and photoelectron detection are included in one coherent process. Bulk state, surface, and vacuum are also included in one Hamiltonian. The one-step model is precise but complicated, therefore, so called *three-step model* is more widely used to understand the results of the photoemission

spectroscopy. In the three-step model, photoemission process is separated into three steps shown in Fig. 2.2: (i) photoexcitation process, (ii) transfer process, and (iii) escape process. This separation is an arbitral one, however, it explains the experimental results very well. These three steps are explained in the following sections.

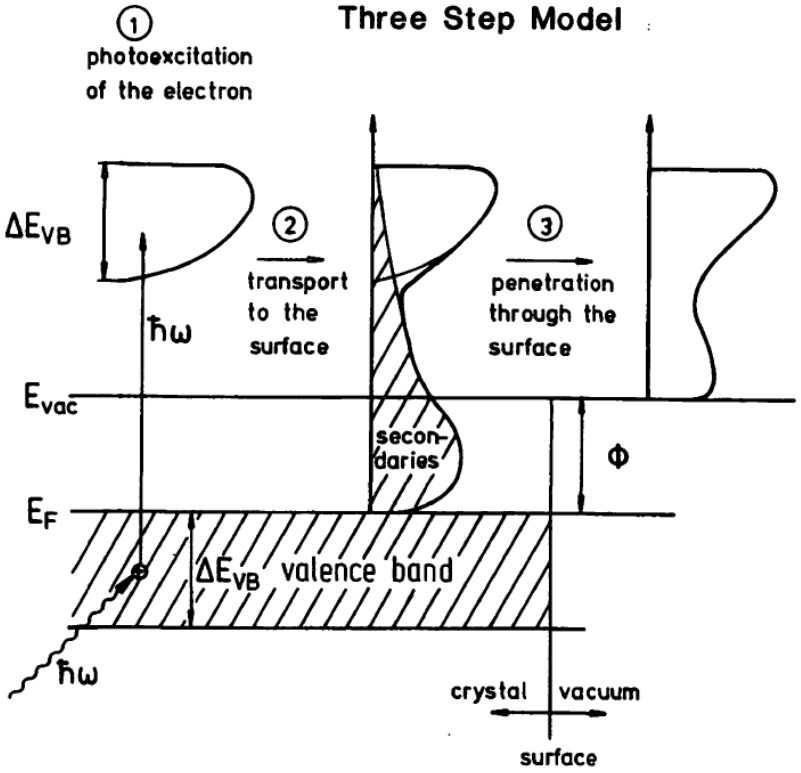

Figure 2.2: Three-step model in photoemission [30].

2.2.1 Photoexcitation process

The first process in the three-step model is the photoexcitation process, in which photons excite electrons in a crystal. This is a transition of electrons to excited states by absorption of light. Photoelectron spectra are mainly determined by this photoexcitation process. In one-electron approximation, where electron-electron correlation is ignored, photoelectron spectra give band structures in valence bands.

To calculate w_{fi} in Eq. (2.2), it is convenient to separate the system into the photoelectron and the $(N-1)$-electron system. Here, we assume that the release of the photoelectron occurs suddenly, and the excited electron and the $(N-1)$-electron system do not interact (sudden approximation). In practice, the sudden approximation is not trivial because the whole system is relaxed during the photoemission process. Under sudden approximation, the final state is given by

$$\Psi_f^N = \mathcal{A}\phi_f^{\boldsymbol{k}}\Psi_f^{N-1}, \tag{2.4}$$

where $\mathcal{A}$ is an antisymmetric operator for the N-electron wave function, $\phi_f^{\boldsymbol{k}}$ is the wave function of the photoelectron with momentum $\boldsymbol{k}$, and Ψ_f^{N-1} is the final state wave function of the $(N-1)$-electron system, which can be chosen as an excited state with eigenfunction, Ψ_m^{N-1} and eigenenergy E_m^{N-1}. The transition probability is obtained by summation for m. For simplicity, the initial state is written as a Slater determinant given by

$$\Psi_i^N = \mathcal{A}\phi_i^k\Psi_i^{N-1}, \tag{2.5}$$

where $\phi_i^{\boldsymbol{k}}$ is a one electron state and Ψ_i^{N-1} is the $(N-1)$-electron system left. By using Eqs. (2.4) and (2.5), the matrix element can be written as

$$\langle\Psi_f^N|H_{\rm int}|\Psi_i^N\rangle = \langle\phi_f^k|H_{\rm int}|\phi_i^k\rangle\,\langle\Psi_f^{N-1}|\Psi_i^{N-1}\rangle\,. \tag{2.6}$$

Total photoelectron intensity, therefore, is given by

$$\begin{aligned} I(\boldsymbol{k}, E_k) &= \sum_{f,i} w_{f,i} \\ &= \frac{2\pi}{\hbar}\sum_{f,i}|M_{f,i}^{\boldsymbol{k}}|^2\sum_m |c_{m,i}|^2\delta(E_k + E_m^{N-1} - E_i^N - \hbar\omega), \end{aligned} \tag{2.7}$$

where $M_{f,i}^{\boldsymbol{k}} = \langle\phi_f^k|H_{\rm int}|\phi_i^k\rangle \propto \langle\phi_f^k|\boldsymbol{A}\cdot\boldsymbol{p}|\phi_i^k\rangle$ is a one electron matrix element, and $|c_{m,i}|^2 = |\,\langle\Psi_m^{N-1}|\Psi_i^{N-1}\rangle\,|^2$ is the probability that the removal of an electron from state i will leave the $(N-1)$-electron system in the excited state m. If electron correlation is ignored, one can think of $\Psi_i^{N-1} = \Psi_{m_0}^{N-1}$ for one state $m = m_0$, and one finds

$$|c_{m,i}|^2 = \begin{cases} 1, & (m = m_0) \\ 0, & (m \neq m_0). \end{cases} \tag{2.8}$$

In this case, if $|M_{\rm B}^{\boldsymbol{k}}|^2 \neq 0$, the photoelectron spectrum is a delta function at Hartree-Fock orbital energy $E_{\rm B}^{\boldsymbol{k}} = -\epsilon_{\boldsymbol{k}}$.

If electron correlation is strong and many $|c_{m,i}|^2$ are finite, Green's function formalism is commonly used to calculate the photoelectron spectra. Note that $\hbar = 1$ in the following in this subsection. One particle Green's function expresses the development of the N-electron system after adding an electron or a hole, which is given by

$$G(\boldsymbol{k},\omega) = \sum_m \frac{|\langle \Psi_m^{N+1}|c_{\boldsymbol{k}\sigma}^\dagger|\Psi_i^N\rangle|^2}{\omega - E_m^{N+1} + E_i^N + i\eta} + \sum_m \frac{\langle \Psi_m^{N-1}|c_{\boldsymbol{k}\sigma}|\Psi_i^N\rangle|^2}{\omega - E_m^{N-1} + E_i^N + i\eta}, \tag{2.9}$$

where $c_{\boldsymbol{k}\sigma}^\dagger(c_{\boldsymbol{k}\sigma})$ is the operator that creates (annihilates) the electron with energy ω, momentum $\boldsymbol{k}$, and spin σ, to N-electron initial state Ψ_i^N, and η is positive infinitesimal. The sum is taken along all possible $(N \pm 1)$-electron eigenstates $\Psi_m^{N\pm1}$ (with eigenenergy $E_m^{N\pm1}$). In the limit $\eta \to 0^+$, one can make use of the identity $(x \pm i\eta)^{-1} = \mathcal{P}(1/x) \mp i\pi\delta(x)$, where $\mathcal{P}$ denotes the principal value, to obtain the one-particle spectral function. Using Green's function, photoelectron spectrum is given by one-particle spectral function

$$A(\boldsymbol{k},\omega) = -\frac{1}{\pi}\,\mathrm{Im}\,G(\boldsymbol{k},\omega). \tag{2.10}$$

At finite temperature, one can use finite temperature formalism of Green's function. In this case, photoelectron intensity is given by

$$I(\boldsymbol{k},\omega) \propto |M_{f,i}^{\boldsymbol{k}}|^2 f(\omega) A(\boldsymbol{k},\omega), \tag{2.11}$$

where $\boldsymbol{k} = \boldsymbol{k}_\parallel$ is the in-plane component of the photoelectron momentum, ω is the energy of the photoelectron measured from Fermi level of the crystal, E_F, and $f(\omega) = (\exp(\omega/k_\mathrm{B}T) + 1)^{-1}$ is Fermi Dirac function. In real measurements, background and broadening of the spectra should be considered as well.

In Green's function formalism, electron correlation can be treated by introducing self energy, $\Sigma(\boldsymbol{k},\omega) = \Sigma'(\boldsymbol{k},\omega) + i\Sigma''(\boldsymbol{k},\omega)$. The real and imaginary parts of self energy contain all the information about energy renormalization and quasiparticle lifetime of electrons with band energy ω and momentum $\boldsymbol{k}$ in many-body systems. The Green's function and the spectral function are written in the form using self-energy as follows

$$\begin{aligned} G(\boldsymbol{k},\omega) &= \frac{1}{\omega - \epsilon_{\boldsymbol{k}} - \Sigma(\boldsymbol{k},\omega)} \\ A(\boldsymbol{k},\omega) &= -\frac{1}{\pi}\frac{\Sigma''(\boldsymbol{k},\omega)}{[\omega - \epsilon_k - \Sigma'(\boldsymbol{k},\omega)]^2 + [\Sigma''(\boldsymbol{k},\omega)]^2}. \end{aligned} \tag{2.12}$$

If electron correlation is ignored, $\Sigma(\boldsymbol{k},\omega) = 0$, and $G(\boldsymbol{k},\omega) = 1/(\omega - \epsilon_k \pm i\eta)$ has a pole. In this case, the spectral function, $A(\boldsymbol{k},\omega) = \delta(\omega - \epsilon_{\boldsymbol{k}})$ represents one electron density of state (Fig(2.3)(a)).

If electron correlation cannot be ignored, quasiparticle, an electron or a hole " dressed by a cloud of virtual excitations " is generated instead of a bare electron or hole. A quasiparticle is similar to a particle in a system without interaction, but has a

renormalized energy $\varepsilon_{\boldsymbol{k}}$, mass m^*, and a finite lifetime $\tau = 1/\Gamma_{\boldsymbol{k}}$. The Green's function and spectral function are separated into coherent pole parts and incoherent smooth parts without poles as follows

$$\begin{aligned} G(\boldsymbol{k},\omega) &= \frac{Z_{\boldsymbol{k}}}{\omega - \varepsilon_{\boldsymbol{k}} + i\Gamma_{\boldsymbol{k}}} + G_{\text{inch}} \\ A(\boldsymbol{k},\omega) &= Z_{\boldsymbol{k}} \frac{\Gamma_{\boldsymbol{k}}/\pi}{(\omega - \varepsilon_{\boldsymbol{k}})^2 + \Gamma_{\boldsymbol{k}}^2} + A_{\text{inch}}, \end{aligned} \tag{2.13}$$

where $Z_{\boldsymbol{k}} = (1 - \partial\Sigma'/\partial\omega)^{-1}$, $\varepsilon_{\boldsymbol{k}} = \varepsilon + \Sigma'$, $\Gamma_{\boldsymbol{k}} = Z_{\boldsymbol{k}}|\Sigma''|$, G_{inch} and A_{inch} are incoherent parts (Fig. 2.3(b)). The energy of the quasiparticle shifts by Σ' from original energy, and the lifetime is determined by Σ''.

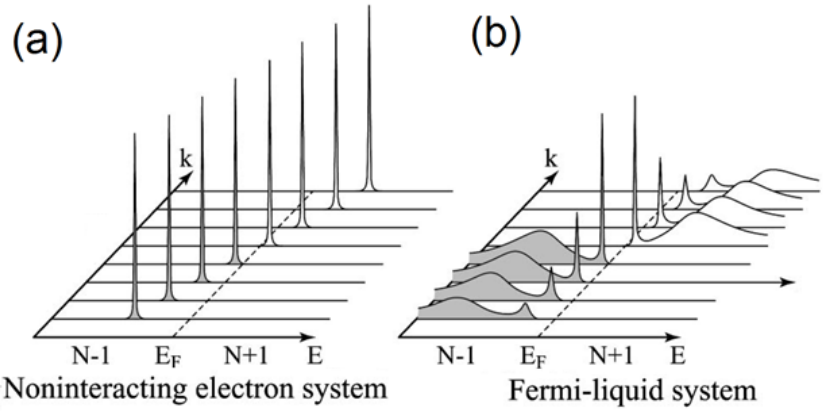

Figure 2.3: Angle-resolved spectra when removing and adding one electron [32]. (a) Noninteracting electron system. (b) Fermi liquid system with electron-electron interaction.

2.2.2 Transfer process and escape process

The second process in the three-step model is the transfer process. After the photoexcitation, some of the excited electrons are transported to the surface. Electrons that have lost energy due to inelastic scatterings by other electrons or nuclei during transport are called secondary electrons. The secondary electrons form a smooth large background on the low energy side of the excited electron population, as shown in Fig. 2.2. Since the excitation light used in photoelectron spectroscopy is between 10 and 10,000 eV, the transition time between the initial and final states is estimated to be about $10^{-18} - 10^{-15}$ seconds. Similarly, the time for which photoelectrons having this level of energy are transported to the surface is estimated to be about 10^{-15} seconds. On the other hand, the time scale for the crystal lattice to oscillate is about 10^{-12} seconds, so the lattice is

considered to be stationary during the photoelectron transport process (Frank-Condon principle).

Since the excitation light used for photoelectron spectroscopy enters the material about $100 - 1000$ Å, most of the electron excitations occur in the bulk rather than near the surface. However, in order for the excited electrons to escape from the material with the information of the band structure, they must reach to the surface without being subjected to inelastic scattering in material. Figure 2.4 shows the average distance (inelastic mean free path) that an electron can travel in a material without scattering. The mean free path is equal to the escape depth when the excited electrons travel in a direction perpendicular to the surface. Note that the reference of the energy of the excited electrons is E_{F}, hence, the horizontal axis is same as photon energy for electrons at E_{F}. The mean free path of electrons is determined by electron-electron and electron-phonon scatterings, and electron-electron scattering is dominant except for very low energies. For the energies of interest here, the electrons in the crystal can be approximately described by a free-electron gas. In this case, mean free path is determined by the plasma frequency which is only function of the electron density. The mean free path follows a "universal" curve since the electron density is roughly equal for all materials. When the electron energy is 20 - 100 eV, the mean free path is 3 - 5 Å, so it is surface sensitive, and when using the 7 eV laser used in this thesis, it is sufficiently bulk sensitive, corresponding to several tens of Å.

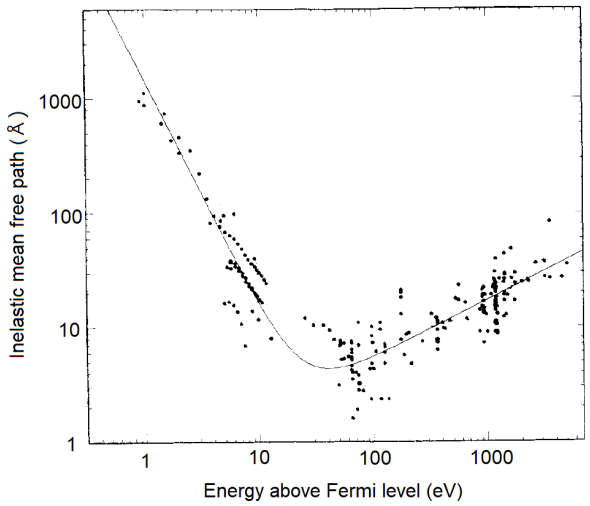

Figure 2.4: Compilation for elements of inelastic mean free path measurements as a function of energy above the E_{F} [33]. The curve is fitting to an empirical function $\lambda = A/E^2 + B\sqrt{E}$, where A and B are fitting parameters.

The last process in the three-step model is the escape process, in which the electrons escape from the surface. Since there is a potential called work function, Φ, on the material surface, excited electrons with energy exceeding this potential can escape into the vacuum. The work function is the energy difference between E_{F} and the vacuum

level, E_{vac}. We describe E_{vac} in more detail in Sec. 2.5.2. The photoelectron spectrum is obtained by measuring the electron kinetic energy distribution.

2.3 Angle-resolved photoemission spectroscopy

By performing ARPES, the band structure and the Fermi surface of the sample are determined experimentally.

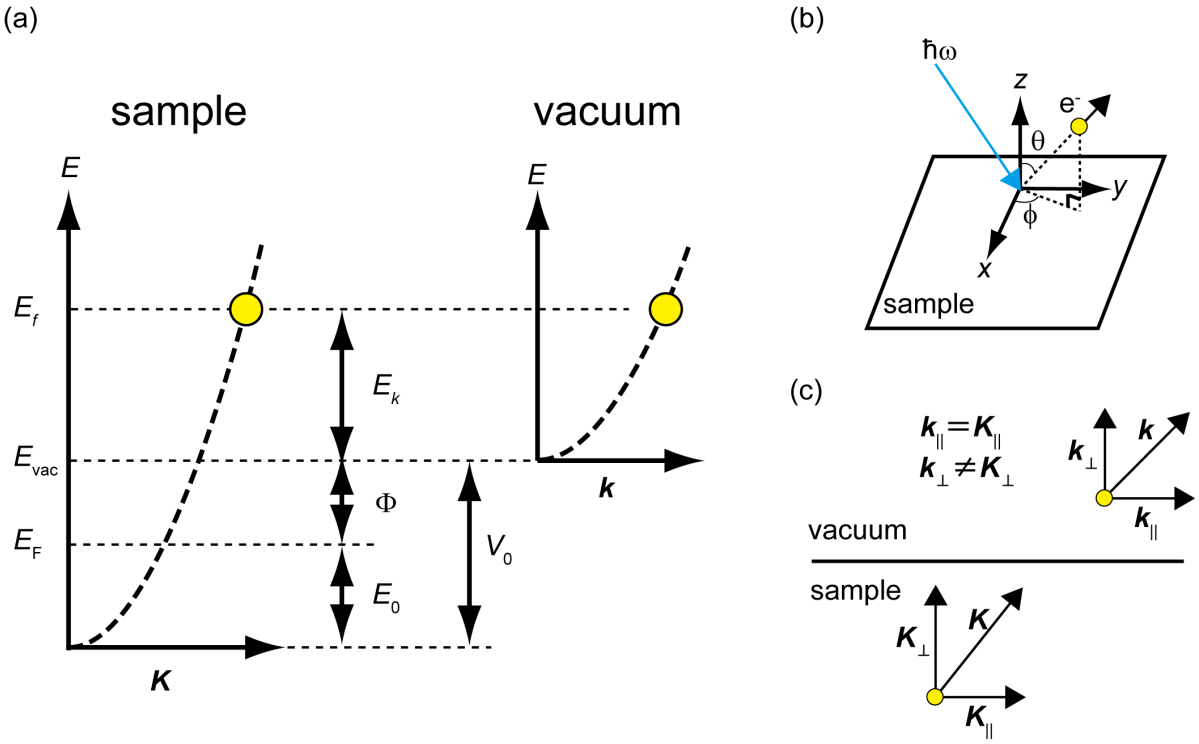

Figure 2.5: Energy and momentum conservation of a photoelectron in the sample and vacuum. (a) Energy conservation. (b) Escape of photoelectron. (c) Momentum conservation. See text for details of parameters in the image.

The energy levels of photoelectrons are shown in Fig. 2.5(a). The final state of the photoexcited electron in the sample is approximated as a free electron (free electron approximation). To calculate the momentum of photoelectron, we take E_{F} as the zero point of energy. The final state energy E_f can be written as

$$E_f = \frac{\hbar^2(K_{\|}^2 + K_{\perp}^2)}{2m} - E_0, \tag{2.14}$$

where $K_{\|}$ and $K_{\perp}$ are parallel and perpendicular components of the momentum of the excited electron in the sample, and E_0 is the energy difference between E_{F} and the

bottom of the energy dispersion in the free electron approximation. The kinetic energy of the photoelectron emitted out of the sample, E_k is given by

$$E_k = E_f - \Phi. \tag{2.15}$$

The components parallel and perpendicular to the sample surface of the momentum of the photoelectrons emitted out of the sample can be written as follows

$$\begin{aligned} \hbar k_{\parallel} &= \sqrt{2mE_k}\sin\theta \\ \hbar k_{\perp} &= \sqrt{2mE_k}\cos\theta, \end{aligned} \tag{2.16}$$

where θ is an angle measured from the crystal surface normal. In case of crystals, since translational symmetry exists in the direction parallel to the surface, photoelectron momentum component which is parallel to the surface is conserved when escaping from the sample surface, i.e.

$$k_{\parallel} = K_{\parallel}. \tag{2.17}$$

This is the most important assumption in ARPES. The relationship between the momentum of initial state and the kinetic energy of photoelectron is obtained from Eqs. (2.14) and (2.17), and is

$$\begin{aligned} \hbar K_{\parallel} &= \sqrt{2mE_k}\sin\theta \\ \hbar K_{\perp} &= \sqrt{2m(E_k\cos^2\theta + V_0)}, \end{aligned} \tag{2.18}$$

where $V_0 = \Phi + E_0$ is inner potential, used as a fitting parameter. Including in-plane momentum of photoelectron, Eq. (2.18) is rewritten as

$$\begin{aligned} \hbar K_x &= \sqrt{2mE_k}\sin\theta\cos\phi \\ \hbar K_y &= \sqrt{2mE_k}\sin\theta\sin\phi \\ \hbar K_z &= \sqrt{2m(E_k\cos^2\theta + V_0)}, \end{aligned} \tag{2.19}$$

where ϕ is an angle within the crystal surface, as shown in Fig. 2.5(b). Equation (2.18) at E_{F} ($E_{\mathrm{B}} = 0$) is rewritten into convenient form

$$K_{\parallel} = \frac{\sqrt{2m}}{\hbar}\sqrt{\hbar\omega - \Phi}\sin\theta \\ = 0.512\sqrt{(\hbar\omega - \Phi)\ [\mathrm{eV}]}\sin\theta \quad [\mathrm{\AA}^{-1}], \tag{2.20}$$

where $m = 0.511$ MeV$/c^2$, $\hbar = 6.58 \times 10^{-16}$ eV·s, and $c = 3.00 \times 10^8$ m/s is the speed of light.

Since the escape depth of photoelectrons is at most several atomic layers, the uncertainty of momentum in the vertical direction is finite due to the uncertainty principle ($\Delta x \Delta k \geq 1$). If the energy of the excitation light is 20-40 eV, the escape depth is about 5 Å, and the momentum in the vertical direction $k_{\perp}$ spreads about 0.2 Å^{-1}. In case of 7 eV excitation light, the escape depth is about several tens of millimeters, and the spread of $k_{\perp}$ is suppressed to 0.1 Å^{-1} or less.

A photoelectron spectrum obtained by measuring the photoelectron energy distribution with the momentum fixed is called Energy Distribution Curve (EDC), and that with the energy fixed is called Momentum Distribution Curve (MDC), as shown in Fig. 2.6.

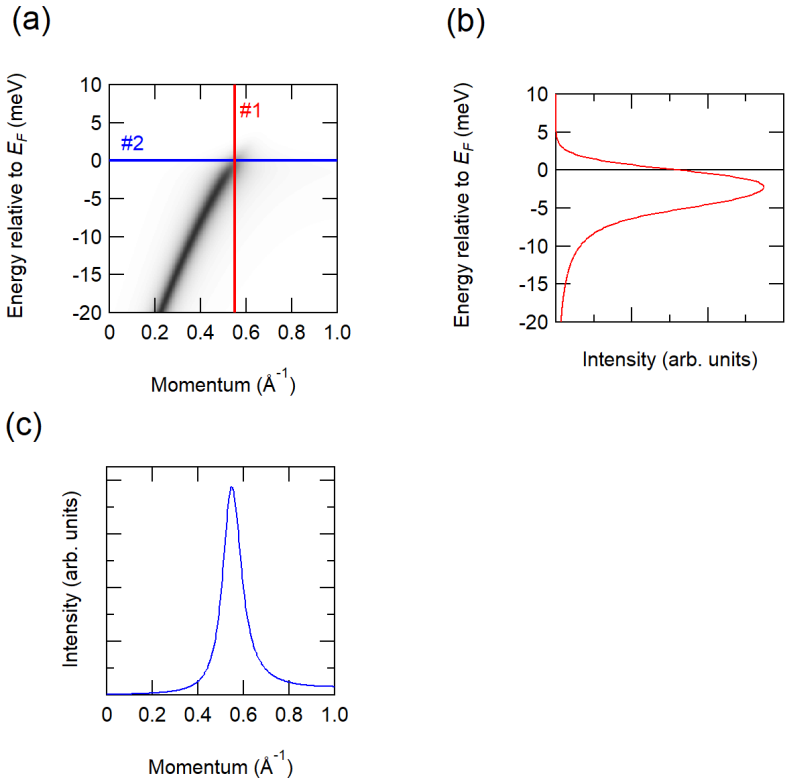

Figure 2.6: Energy distribution curve (EDC) and momentum distribution curve (MDC). (a) A sample dispersion. (b) EDC at #1 in (a). (c) MDC at #2 in (a).

2.4 Selection rule

By switching the polarization of the linearly polarized incident light, the parity of the initial wave function to be observed can be selected (selection rule). The photoelectron intensity takes a finite value only when the matrix element, $M^k_{f,i}$, in Eq. 2.7 is finite. The matrix element is given by

$$M^{\boldsymbol{k}}_{f,i} \propto \langle \phi^k_f | \boldsymbol{A} \cdot \boldsymbol{p} | \phi^k_i \rangle \tag{2.21}$$

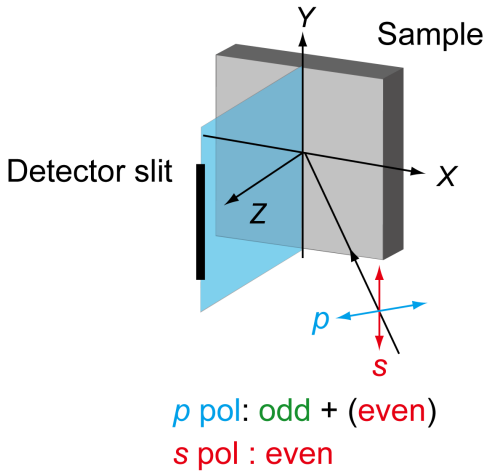

Figure 2.7: Experimental configuration in this thesis. Parity is difined according to a mirror plane $x = 0$.

Consider the parity according to the sample mirror plane $x = 0$ (the blue plane in Fig. 2.7). Photoelectrons that pass through the slit (detector slit) in Fig. 2.7 are detected. Consider the case where the detector slit is included in the mirror plane. Since the detected photoelectron, ϕ^k_f, is assumed to be a free electron plane wave with momentum in the mirror plane, the parity is even. On the other hand, the parity of $\boldsymbol{A} \cdot \boldsymbol{p}$ is the same as the parity of $\boldsymbol{A}$ and is determined in the mirror plane (even) or perpendicular to the mirror plane (odd). Therefore, the matrix elements are finite when

$$\langle \phi^k_f | \boldsymbol{A} \cdot \boldsymbol{p} | \phi^k_i \rangle = \begin{cases} \phi^f_k : \text{ even } \langle + | + | + \rangle & \rightarrow \boldsymbol{A} : \text{ even} \\ \phi^f_k : \text{ odd } \langle + | - | - \rangle & \rightarrow \boldsymbol{A} : \text{ odd.} \end{cases} \tag{2.22}$$

The linear polarizations of light source are classified into p-polarization, which is parallel to the incident plane (ZX plane in Fig. 2.7), and s-polarization, which is perpendicular to the entrance plane ("senkrecht" in German). They are also called L.H. (linear horizontal, corresponding to p-polarization in the configuration shown in Fig. 2.7) and L.V. (linear vertical, s-polarization). If s-polarized light is used, it is possible to observe

an initial state having an odd parity (for example, $3d_{yz}$ orbital) and not to observe an initial state having an even parity (for example, $3d_{zx}$ orbital).

2.5 Detection of photoelectrons

2.5.1 Analyzer

Two dimensional hemispherical analyzers are widely used to analyze photoelectrons. Photoelectrons emitted from a sample travel through vacuum into an electron analyzer. Firstly, electrons travel into electron lens, where electrons are retarded, then they go through an analyzer slit to enter the electron analyzer. A hemispherical electron analyzer is made up of two bowls, and voltage is applied between the outer sphere (radius R_2) and the sphere (radius R_1). Electrons with a specific kinetic energy determined by this voltage can reach the other side of the analyzer. Those electrons are multiplied by a multi-channel plate (MCP), turned into light by a fluorescent screen, and those lights are counted by a CCD or scientific complementary metal oxide semiconductor (sCMOS) camera. This system enables two dimensional measurement (energy and momentum) at once.

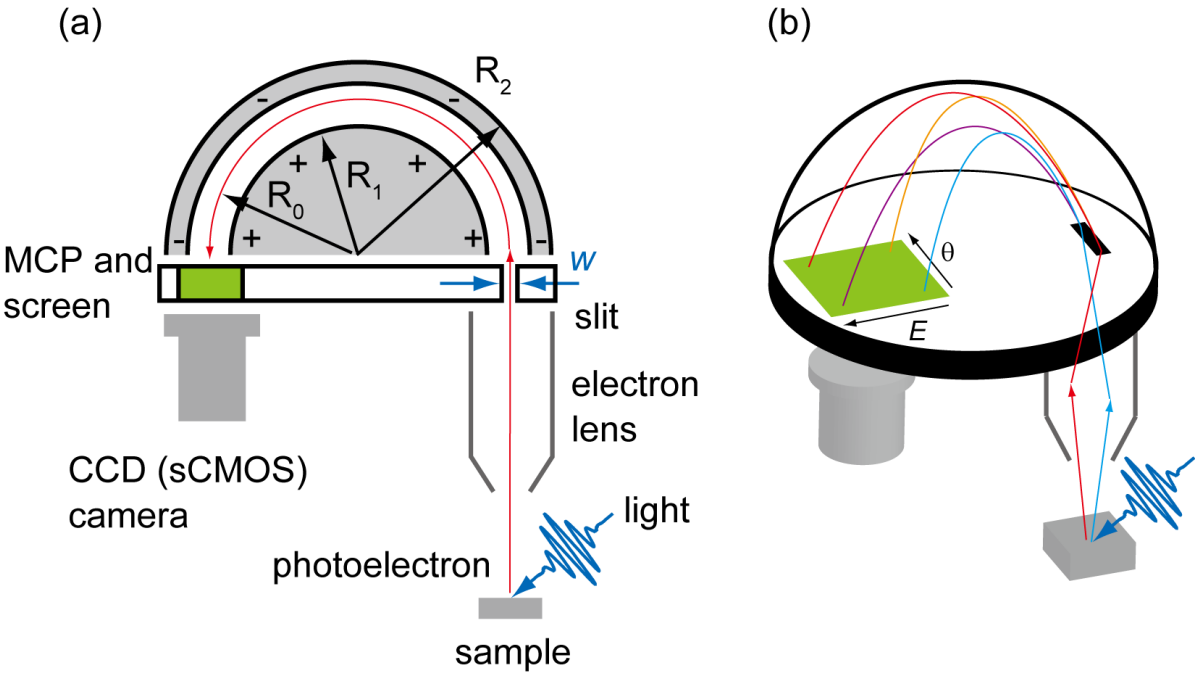

Figure 2.8: Schematic images of Photoelectron analyzer. (a) Side view. (b) Three dimensional view.

The energy resolution of the electron analyzer, Δ_{a}, is approximated as

$$\Delta_{\mathrm{a}} = \frac{wE_{\mathrm{p}}}{2R_0}, \tag{2.23}$$

where w is the slit width of the entrance of the electron analyzer, E_{p} is the kinetic energy of photoelectrons which enters the electron analyzer (pass energy), and $R_0 = (R_1+R_2)/2$ is the average radius of the hemisphere. One can reduce w to obtain better resolution, but the number of photoelectrons that go into the analyzer decreases, which leads to a longer measurement time.

2.5.2 Energy levels in detecting photoelectrons

In consideration of energy levels of sample and detector, one must distinguish the *vacuum level of a finite-size sample*, $E_{\mathrm{vac}}(s)$, and the *vacuum level at infinity*, $E_{\mathrm{vac}}(\infty)$, (Fig. 2.9(a) [34]). $E_{\mathrm{vac}}(s)$ is defined as the energy of an electron at rest just outside the surface of the crystal. In the case of a metal, this distance is also the one where there is no effect of image forces, i.e., where the image potential is essentially zero. This vacuum level is a characteristic of the surface, and depends sensitively on the atomic, chemical, and band structures of the outer atomic layers of the crystal. $E_{\mathrm{vac}}(\infty)$ is defined as the energy of an electron at rest at infinity distance from the surface. This energy level is invariant, but experimentally not accessible. The energy difference between $E_{\mathrm{vac}}(s)$ and $E_{\mathrm{vac}}(\infty)$ stems from the contributions of surface dipoles to the work function, as shown in Fig. 2.9(b). The surface dipole on metals normally raises the energy of the vacuum level, as it is caused by spilling of the electronic charge density out of the surface, leaving a positive charge inside.

Figure 2.9(c) shows energy levels in detecting photoelectron. If the sample under investigation is a metal E_{F} matches between the sample and the detector since they are in electronic contact. The reference of kinetic energy at the detector is the vacuum level of the detector, $E_{\mathrm{vac}}(d)$. The minimum kinetic energy arriving at the detector, $E_k(d)^{\mathrm{min}}$, is given by

$$E_k(d)^{\mathrm{min}} = \Phi_{\mathrm{s}} - \Phi_{\mathrm{d}}, \tag{2.24}$$

where Φ_{s} and Φ_{d} are the work function of the sample and that of the detector, respectively. On the other hand, the photoelectrons with initial state at E_{F} give the maximum kinetic energy at the detector

$$E_k(d)^{\mathrm{max}} = \hbar\omega - \Phi_{\mathrm{d}}. \tag{2.25}$$

Note that $E_k(d)^{\mathrm{max}}$ is independent of samples, since Φ_{d} is the property of the analyzer. This means that one can refer E_{F} of gold as the reference of E_{F} of the sample, as long as they are in electronic contact. Both $E_k(d)^{\mathrm{min}}$ and $E_k(d)^{\mathrm{max}}$ are not related to $E_{\mathrm{vac}}(\infty)$.

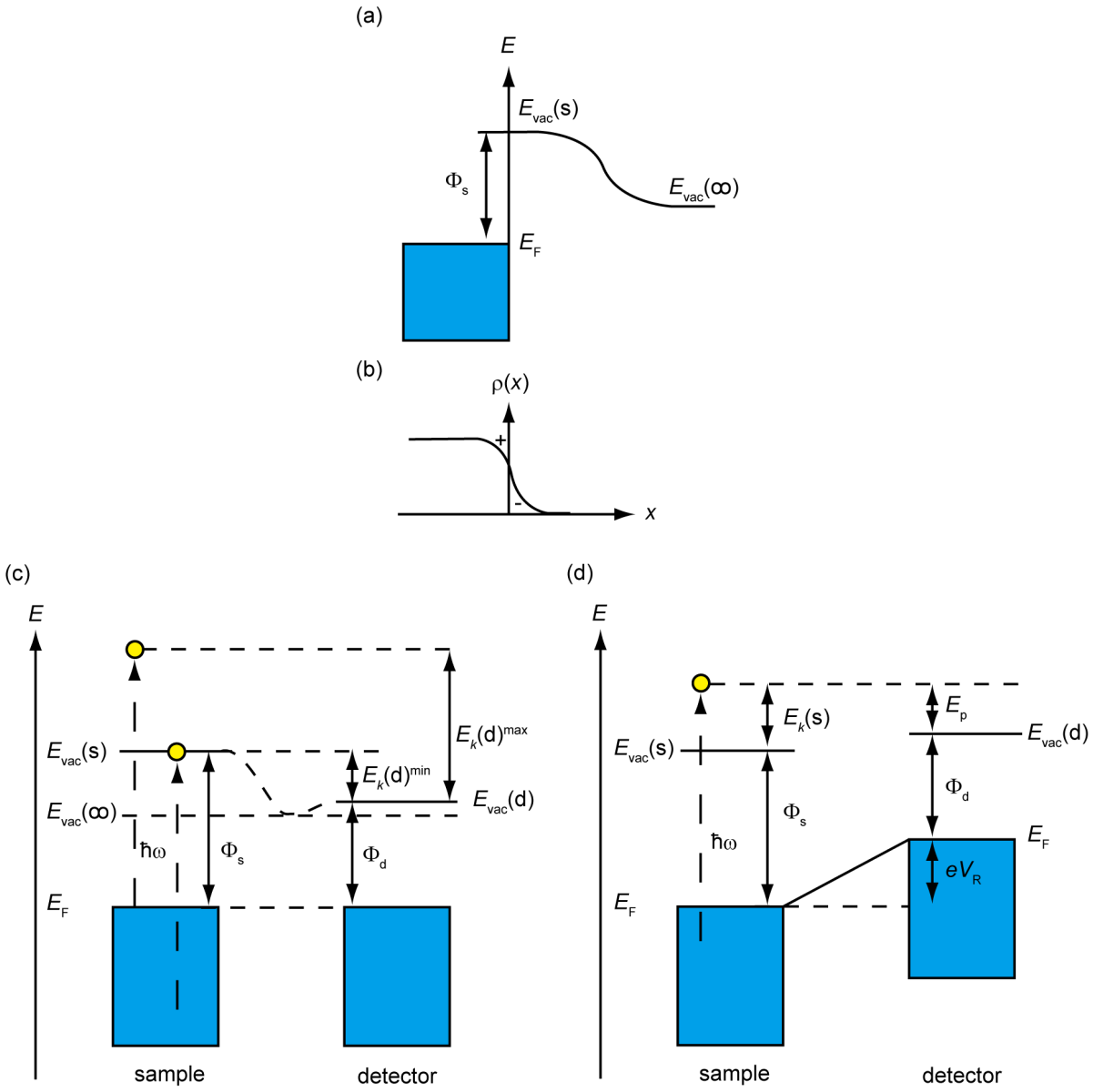

Figure 2.9: Photoelectron detection. (a) Energy diagram of vacuum level. Vacuum level close to the surface, $E_{\rm vac}(s)$, work function, Φ_m, and vacuum level at infinity, $E_{\rm vac}(\infty)$ are shown. (b) Position dependence of electron distribution density, $\rho(x)$. Inside (outside) the sample is $x < 0$ ($x > 0$). (c) Energy diagram of the sample and the detector. (d) Energy diagram when voltage is applied to the detector. See text for details of parameters in the image.

The energy resolution of the electron analyzer in Eq. (2.23) is proportional to $E_{\rm p}$, therefore, electrons are retarded at the electron lens to obtain better energy resolution as shown in Fig. 2.9(d). $E_{\rm p}$ is given by

$$E_{\rm p} = E_k(s) + \Phi_{\rm s} - \Phi_{\rm d} - eV_{\rm R}, \tag{2.26}$$

where $E_k(s)$ is the kinetic energy of photoelectron measured from $E_{\rm vac}(s)$, and $V_{\rm R}$ is retardation potential.

Note that the kinetic energy, E_k, the work function, Φ, and the vacuum level $E_{\rm vac}$ discussed in other sections are those at the sample unless explicitly stated.

2.6 Evaluation of superconducting gap

As introduced in Sec. 1.1, the superconducting gap, Δ, is an order parameter that characterizes the superconducting state. Here, we explain how the superconducting gap can be evaluated from ARPES measurements. The reference of energy is set to $E_{\rm F}$. As shown in Eq. (1.8), the Bogoliubov quasiparticle dispersion, $E(k)$, with respect to momentum k is given by

$$E(k) = \sqrt{\xi(k)^2 + |\Delta(k)|^2}, \tag{2.27}$$

where $\xi(k)$ is quasiparticle dispersion in the normal state. The corresponding spectral function is given by

$$A(k,\omega) = \frac{1}{\pi}\left\{\frac{|u_k|^2\Sigma''}{[\omega - E(k)]^2 + \Sigma''^2} + \frac{|v_k|^2\Sigma''}{[\omega + E(k)]^2 + \Sigma''^2}\right\}, \tag{2.28}$$

where ω is the kinetic energy of the photoelectron, Σ'' is the broadening factor due to the quasiparticle lifetime, and u_k and v_k are the coherence factors which obey the relation

$$u_{\boldsymbol{k}}^2 = \frac{1}{2}\left[1 + \frac{\xi(\boldsymbol{k})}{E(\boldsymbol{k})}\right], \quad |v_{\boldsymbol{k}}^2| = \frac{1}{2}\left[1 - \frac{\xi(\boldsymbol{k})}{E(\boldsymbol{k})}\right], \tag{2.29}$$

as in Eq. (1.7). Figure 2.10 shows calculated spectral function. In crystals, $f(\omega)A(k,\omega)$ gives distribution of electrons. The symmetrization of the spectra is used to obtain the spectral function from measured data and to visualize SC gap. From Eqs (2.28) and (2.29), at Fermi momenta $k_{\rm F}$, $A(k_{\rm F},-\omega) = A(k_{\rm F},\omega)$. We obtain the spectral function by adding raw EDC at $k_{\rm F}$ and reversed spectra with respect to $E_{\rm F}$ as follows

$$\begin{aligned} &f(\omega)A(k_{\rm F},\omega) + f(-\omega)A(k_{\rm F},-\omega) \\ &= f(\omega)A(k_{\rm F},\omega) + [1 - f(\omega)]A(k_{\rm F},\omega) \\ &= A(k_{\rm F},\omega). \end{aligned} \tag{2.30}$$

To quantify SC gap size, fitting to the BCS spectral function shown in Eq. (2.28) is used. The BCS spectral function is multiplied by $f(\omega)$, convoluted with a Gaussian corresponding to the experimental energy resolution, and the integral (Shirley-type) background is added. Since the contribution from the background is quite small in the vicinity of E_{F}, the estimated gap size from the fitting should not be affected by the background. Dynes' function can be also used to quantify SC gap size [35, 36]. The Dynes' function is the BCS excitation spectrum (Eq. (1.26)) broadened by finite-lifetime effect, which is given by

$$\rho(E) = \left| \Re \left[\frac{E - i\Gamma}{\sqrt{(E - i\Gamma)^2 - \Delta^2}} \right] \right|, \tag{2.31}$$

where Γ is lifetime of the quasiparticle. Strictly, as a fitting function for the ARPES EDCs in the SC state, the BCS spectral function is more appropriate than the Dynes ' function. However, the Dynes' function is sometimes easier in practical because it is not necessary to consider a background function and the momentum resolution.

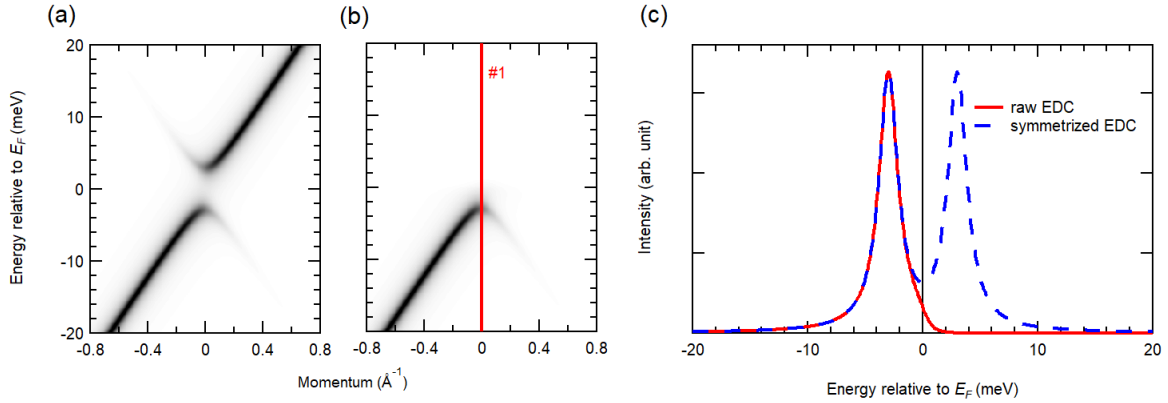

Figure 2.10: Spectral function in the superconducting state. (a) Spectral function calculated using Eq. (2.28), with $\Delta = 3$ meV and $\Sigma'' = 1$ meV. (b) Same as (a) but multiplied by $f(\omega)$. (c) Red line is raw EDC at #1 in (a), and blue dotted line is symmetrized EDC using Eq. (2.30).

3 Ultrahigh resolution and ultralow temperature laser ARPES

In the early 2000s, Prof. S. Shin's group started applying a vacuum ultraviolet (VUV) laser to high energy resolution PES [37–39]. In 2012, Okazaki *et. al.* developed a laser ARPES system achieving 70 μeV and 1 K [36]. This is the main system used in this thesis. The sections about the realization of both high resolution and low temperature, and test measurements are excluded, since we will publish these parts in a journal in near future.

3.1 Measurement examples

In this section, we present the examples of the ARPES results obtained by the laser ARPES system explained in this chapter. This system achieves very high energy resolution and very low temperature, therefore, one can study superconductivity with a very low T_c and fine structures in band dispersions.

3.1.1 Iron-based superconductor $FeTe_{0.55}Se_{0.45}$

Topological superconductors are predicted to host exotic Majorana states that obey non-Abelian statistics and can be used to implement a topological quantum computer. Most of the proposed topological superconductors are realized in difficult-to-fabricate heterostructures at very low temperatures. Zhang *et. al.* found a topological superconductivity on the surface of an iron-based superconductor $FeTe_{0.55}Se_{0.45}$ [10].

Figure 3.1(a) shows the Dirac-cone-type surface band observed around the Brillouin zone center. An isotropic superconducting gap is observed at the Fermi surface of the surface state (Fig. 3.1(b) and (c)). This topological superconductivity is also supported by first-principles calculations of band structures and helical spin polarization observed by the spin ARPES measurements.

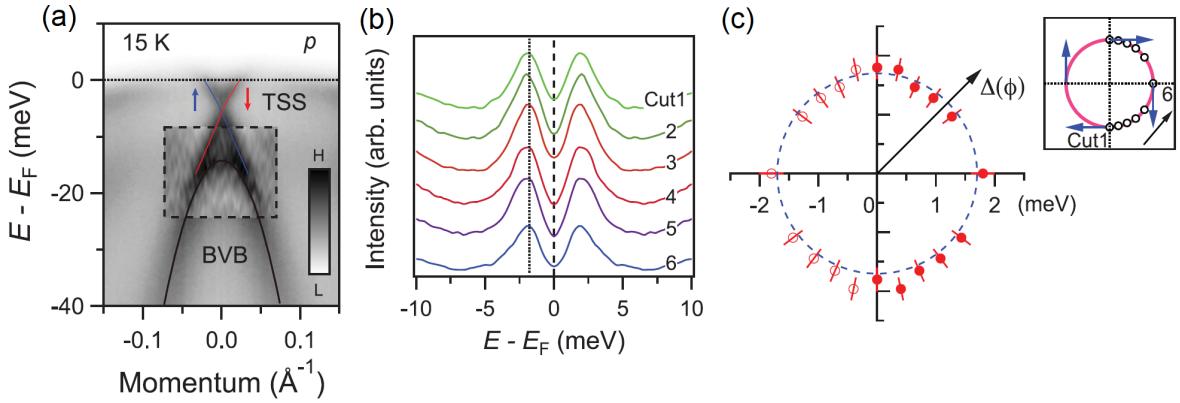

Figure 3.1: Dirac-cone-type band and its superconductivity of $FeTe_{0.55}Se_{0.45}$ [10]. (a) Band dispersion around the Brillouin zone center. (b) Symmetrized EDCs at different Fermi momenta recorded at 2.4 K. (c) Polar representation of the superconducting gap size.

3.1.2 heterostructure film Bi_2Se_3/Nb

Topological superconductivity can be also realized in the heterostructure of a topological insulator film and a simple isotropic *s*-wave superconductor substrate. Flötotto *et. al.* observed the superconductivity of the surface state of Bi_2Se_3/Nb [11].

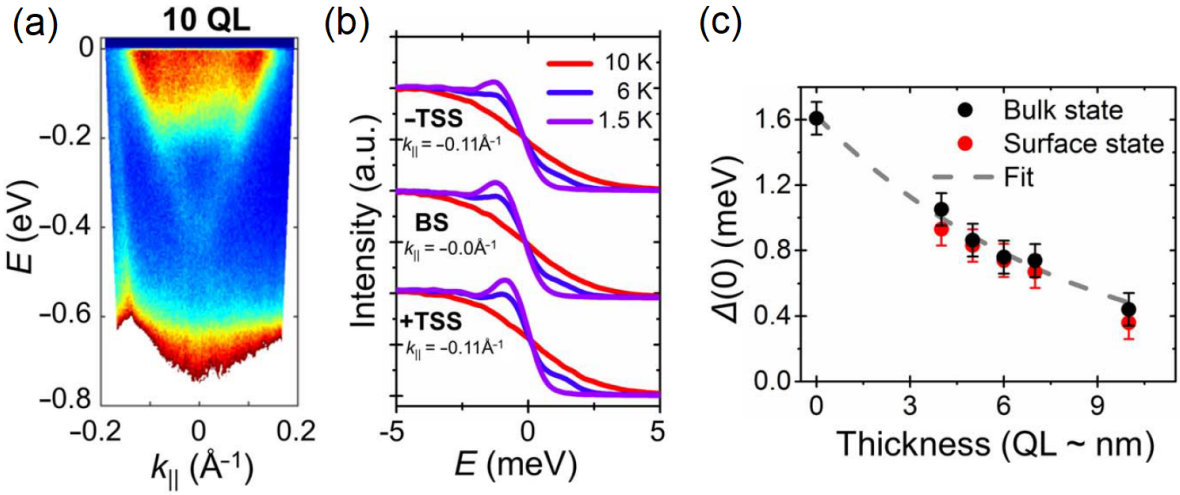

Figure 3.2: Superconductivity of topological states of Bi_2Se_3/Nb [11]. (a) Band dispersion of a sample with a 10-quintuple layers (QL) film. (b) EDCs at three selected momenta corresponding to bulk states (BS), topological surface states with positive and negative momentum (±TSS). (c) The zero temperature gap $\Delta(0)$ for a BS and TSS as a function of film thickness.

A novel "flip-chip" technique enables to cleave ultrathin Bi_2Se_3 film at a predetermined thickness in terms of quintuple layers. Figures 3.2(a) and (b) show a clear Dirac-

cone surface state, and the coherence peaks of superconductivity below T_c of niobium (9.4 K). The zero temperature gap $\Delta(0)$ is determined by the temperature dependence of the superconducting gap at each thickness, and summarized in Fig. 3.2(c).

3.2 Summary

The values achieved in this ARPES system are summarized in Tab. 3.1. To our knowledge, the total energy resolution of 70 μeV is the best among ARPES systems all over the world. The combination of good energy resolution and cooling performance enable us to explore fine electronic structures in low temperature phase.

Table 3.1: The values achieved in the laser ARPES system.

Photon energy	6.994, 5.8 eV
Lowest temperature	1 K
Total energy resolution	70 μeV
Spot size	180 μm
Light polarization	p, s, $\sigma+$, $\sigma-$

4 Superconducting gap anisotropy of FeSe

In this chapter, we present our research on superconducting gap of FeSe. In Sec. 4.1, we describe previous research on FeSe in both normal and superconducting state. After Sec. 4.2, we present our results.

4.1 Previous research

4.1.1 Single crystals

Superconductivity in FeSe was first reported in 2008 [40]. At first, excess iron was mixed in the sample, and it was difficult to grow pure single crystals for precise measurements. However, a method to produce pure single crystalline FeSe by chemical vapor transport was established in 2013 by Böhmer *et. al.* [41]. Fig. 4.1(a) shows the crystal structure of FeSe, which is the simplest among iron-based superconductors.

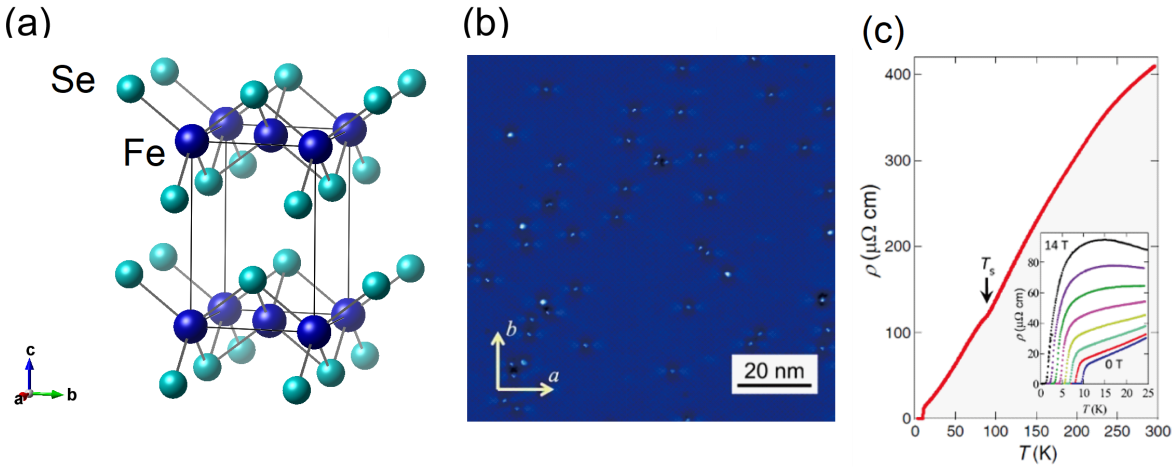

Figure 4.1: Crystal structure and phase transition of FeSe. (a) Crystal structure. Deep blue (light blue) circles represent Fe (Se) atoms. The flame corresponds to 2 Fe/unit cell. (b) STM topograph at 1.5 K. White bright spots are impurities or defects [42]. (c) Temperature dependence of the in-plane resistivity. The structural transition occurs at $T_s \sim 90$ K.

The lattice constants are $a = 3.7707(12)$ Å and $c = 5.521(3)$ Å, which is determined by X-ray powder diffraction [41]. Structural optimization shows Fe : Se = 0.995(4) :

1, a stoichiometric composition within the error bar. The structural phase transition occurs at $T_s = 90\tilde{K}$, and the symmetry of the crystal structure changes from tetragonal ($P4/nmm$) to orthorhombic ($Cmma$). The orthorhombic order parameter $\delta(= |a - b|/(a + b) \approx |a - b|/2a)$ is estimated to be 0.2 % at absolute zero temperature. Single crystals with very good quality are obtained, demonstrated by large residual resistivity ratio (> 40) [42]. From the STM measurement shown in Fig. 4.1(b), it is known that the concentration of impurities and defects is very small, less than 1 for 2000 iron atoms.

The superconducting transition temperature, T_c, of the bulk FeSe is about 9.5 K at atmospheric pressure, as shown in Fig. 4.1(c) [42]. Under pressure, T_c increases upto 37 K at 9 GPa [43]. In single-layer FeSe grown on $SrTiO_3$ substrate, T_c estimated by ARPES is above 60 K [44]. T_c also increases by intercalating a spacer layer between layers, for example, in $Li_x(NH_2)_y(NH_3)_{1-y}Fe_2Se_2$ ($x \sim 0.6, y \sim 0.2$), $T_c \sim 43$ K [45].

4.1.2 Nematicity without magnetism

Nematicity is a state that breaks rotational symmetry but preserves translational symmetry. In FeSe, nematic state appears without antiferromagnetic ordering, unlike other iron-based superconductors.

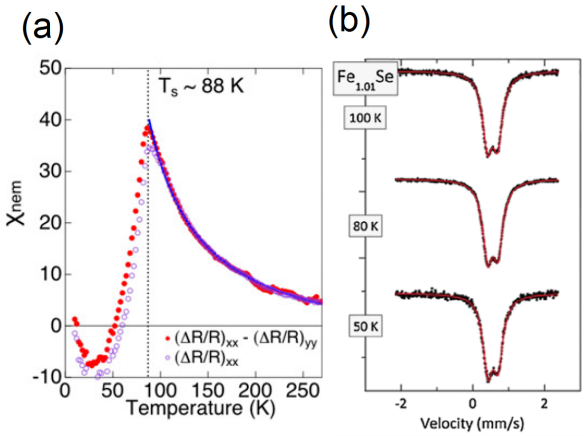

Figure 4.2: Nematicity of FeSe. (a) Temperature dependence of the nematic susceptibility [46]. (b) Temperature dependence of Mössbauer spectra [47].

The divergence of nematic susceptibility is observed in FeSe by the elastoresistivity measurements [46], as shown in Fig. 4.2(a). This demonstrates the existence of nematic fluctuations. In many iron-based superconductors, structural transition, nematicity, and antiferromagnetic ordering occur at temperatures close to each other [19]. When the antiferromagnetic ordering sets in, band folding occurs via the ordering wave vector [48, 49], which makes the band structure complicated. In case of FeSe, however, antiferromagnetic order does not appear as demonstrated by Mössbauer spectra shown in Fig. 4.2(b). This allows us to examine the relationship between nematicity and superconductivity.

Absence of antiferromagnetic order is attributed to the frustration of magnetic fluctuations [50, 51]. The band structure also changes significantly due to nematicity. It is discussed in Sec. 4.1.3, mainly in Fig. 4.5 and Fig. 4.6. Nematicity without antiferromagnetism makes FeSe an ideal material to study the relationship between nematicity and superconductivity.

4.1.3 Band structure

Figure 4.3(a) shows the Density functional theory (DFT) band calculation of FeSe [52]. The calculation was performed within the local-density approximation. The experimental lattice parameters were employed and the chalcogen height was relaxed via energy minimization. It is expected that there are a hole band near the Γ point and an electron band near the M point. Figures 4.3(b) and (c) show the band structure measurement by ARPES and a comparison between the data and DFT calculations [53]. Only one Fermi surface (FS) has been observed, while three hole FSs are expected in DFT calculations. Compared to DFT calculations, the observed bands become flatter (renormalization) and shift in energy due to electron correlation. Experimentally determined renormalization and shift of energy are band-dependent.

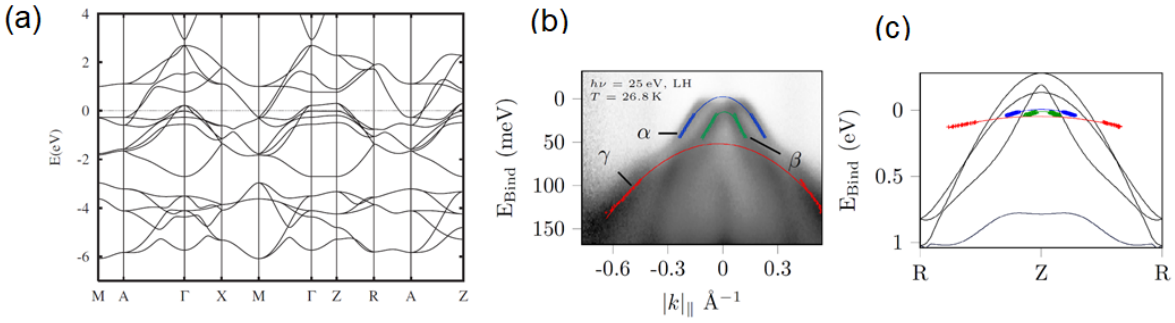

Figure 4.3: Renormalization of band structure in FeSe. (a) Band structure in DFT calculation [52]. (b) Energy momentum cut taken in Z-R direction. (c) Comparison of calculated (solid black lines) and experimental (colored, with markers) dispersions. (b) and (c) are adopted from Ref. [53].

Temperature dependence of FSs observed by ARPES is shown in Fig. 4.4. The band structure has four-fold symmetry above T_s. Below T_s, orbital polarization occurs in the degenerate bands, and elliptical FSs from two different twin domains overlap in momentum space.

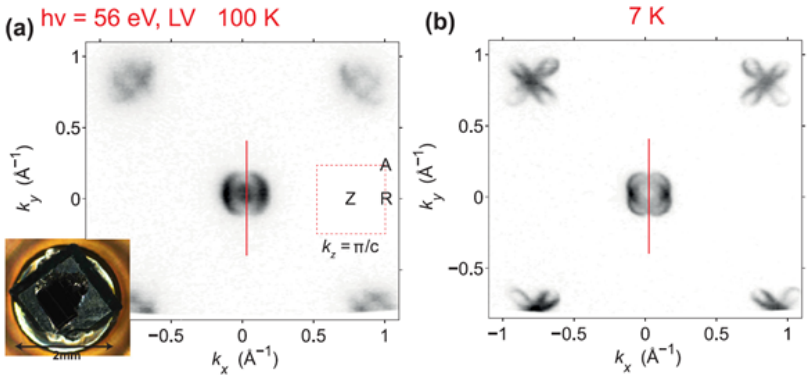

Figure 4.4: Temperature dependence of FSs of FeSe above and below T_s (= 90 K), measured by ARPES. (a) and (b) are taken at 100 K and 7 K, respectively [54].

Many studies reported that the $3d_{yz}$ and $3d_{zx}$ bands of iron split around T_s at M point and the splitting become as large as 50 meV [55–61], as shown in Fig. 4.5. Since this polarization is sufficiently larger than the magnitude of the splitting expected from the crystal field splitting due to the structural transition, it was interpreted as the orbital order derived from the electron system. Some other studies proposed different interpretations with the splitting between $3d_{yz}$ and $3d_{zx}$ smaller than 10 meV [54, 62, 63].

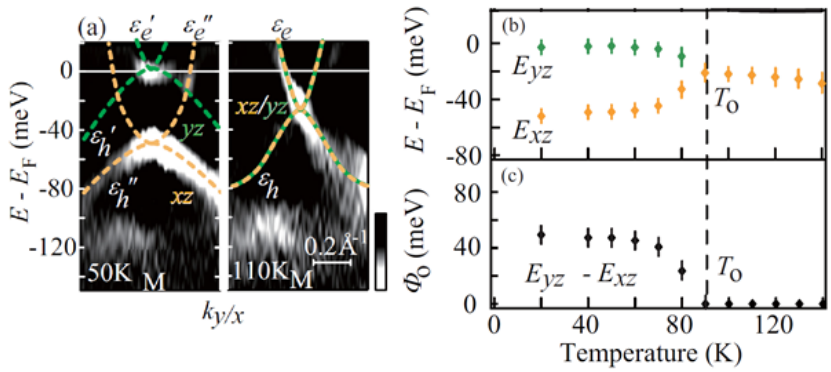

Figure 4.5: Orbital ordering of FeSe observed around M point by ARPES [55]. (a) Temperature dependence of the energy second derivative image. (b) Temperature dependence of d_{xz}/d_{yz} orbitals energy position. (c) Temperature dependence of order parameter $\Phi_0 = E_{yz} - E_{xz}$.

At the Γ point, ARPES measurement using uniaxial tensile strain shows that the $3d_{yz}$ band and $3d_{zx}$ bands, which are degenerated above T_s, are polarized below T_s to

form an elliptic FS (Fig. 4.6 [63, 64]). This elliptical FS consists mostly of $3d_{xz}$.

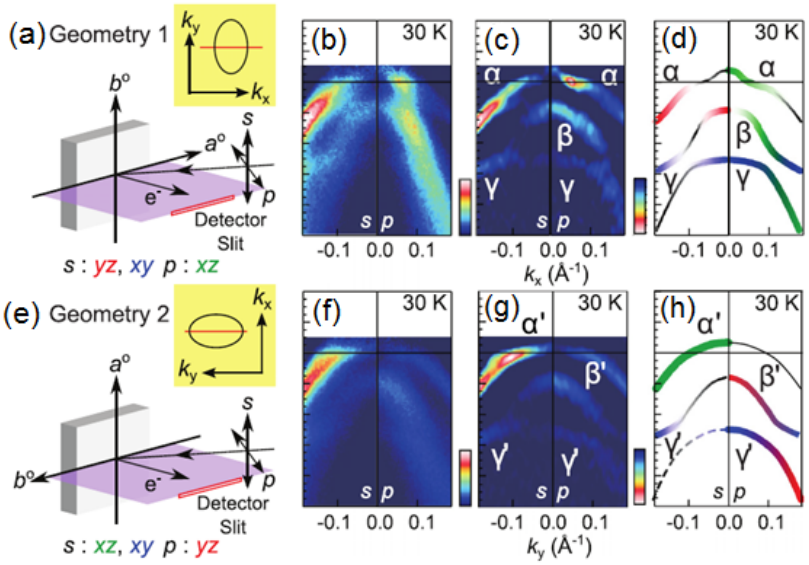

Figure 4.6: Band structure at Γ point of FeSe investigated by detwinned ARPES [64]. (a) Experimental geometries. (b) and (c) $E-k$ image divided by the Fermi Dirac function and its energy second derivative detected in Geometry 1 at 30 K (in nematic state). (d) Schematic band dispersions and their orbital characters. (e) Same as (a) but the sample axes are rotated by 90° in-plane. (f)-(h) Same as (b)-(d) but taken in Geometry 2.

Based on the orbital ordering scenario, the FSs above and below T_s are summarized in Fig. 4.7 [64]. Similar non-equivalent occupancy of electrons has been observed in other iron-based superconductors, for example, $Ba(Fe,Co)_2As_2$ [48] and NaFeAs [65].

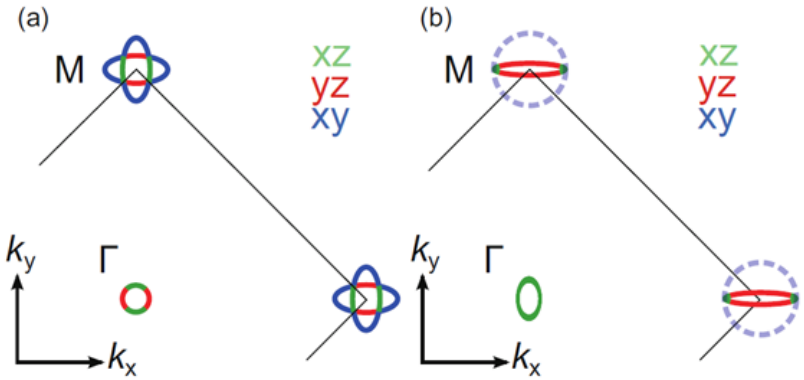

Figure 4.7: (a) and (b) Schematic FSs obtained by ARPES on detwinned FeSe in the tetragonal and orthorhombic phase, respectively [64].

4.1.4 Superconducting state

A node is a point in momentum space where the superconducting gap is zero. It is important to determine if superconducting gap nodes exist or not, for clarifying the mechanism of superconductivity. Low energy excitation of quasiparticles has been measured to determine the existence of nodes.

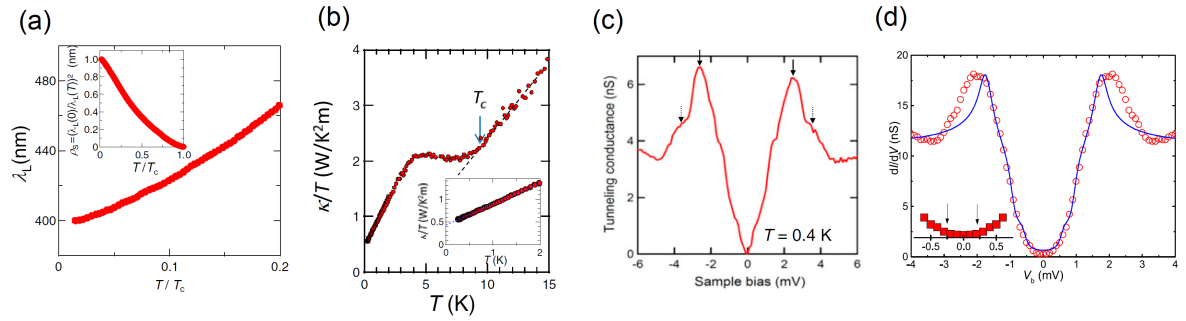

Figure 4.8: Measurements on superconducting gap nodes of FeSe. (a) Temperature dependence of the London penetration length. (b) Temperature dependence of the in-plane thermal conductivity. (c) Tunneling spectrum taken at 0.4 K. (a)-(c) are adopted from Ref. [42]. (d) Tunneling spectrum reported by a different group at 0.35 K [66].

Figures 4.8(a)-(c) suggest existence of line nodes, while Fig. 4.8(d) suggests full gap state without nodes. Nodes are suggested if there are low energy excitations near zero temperature. As shown in Fig. 4.8(a), the London penetration depth shows $\lambda_L \propto T^{1.4}$ at $T/T_c < 0.2$, which suggests line nodes [42]. A residual thermal conductivity divided by temperature, κ/T, at $T \to 0$, κ_0/T, is finite, suggesting line nodes (Fig. 4.8(b)). The tunneling spectrum measured by scanning tunneling spectroscopy (STS) is V-shaped, suggesting the presence of line nodes (Fig. 4.8(c)). Different reports shows, however, very small κ_0/T [67] and U-shaped tunneling spectrum (Fig. 4.8(d) [66]), which corresponds to full gap state without nodes. Reports on superconducting gap nodes are summarized in Tab. 4.1. The conclusions are different between different probes and reports. This may come from different amount of impurities [5] and/or twin boundaries [6] (see Sec. 4.1.5 for details) in different samples.

Table 4.1: Reports on superconducting gap nodes of FeSe. ◯ is nodal, △ is nodal or deep minima, and × is nodeless.

STS	Penetration depth	Specific heat	Thermal conductivity	Reference
			×	[68]
◯				[69]
◯	◯		◯	[42]
		△		[70]
	△			[71]
	×			[72]
			×	[67]
×		△		[66]

The temperature dependence of the upper critical magnetic field suggests spin-singlet superconductivity, as shown in Fig. 4.9 [73, 74]. The upper critical magnetic field, determined by ρ_n (black) and $0.9\rho_n$ (red), is considered close to the actual value. The temperature dependence of the upper critical magnetic field is suppressed more than the curve by Werthamer, Helfand, Hohenberg (WHH) theory. It is because of the spin paramagnetic effect, which is ignored in WHH theory. In spin-triplet superconductivity, the spin directions of electrons constituting the Cooper pair are aligned, so the superconductivity is not suppressed by the spin paramagnetic effect derived from Zeeman splitting. Thus, the presence of the spin paramagnetic effect suggests spin singlet superconductivity in FeSe.

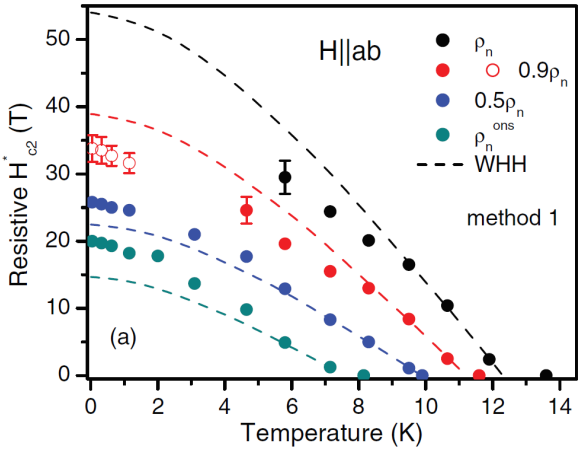

Figure 4.9: Temperature dependence of in-plane upper critical magnetic field measured by magnetoresistance [73].

4.1.5 Time-reversal symmetry breaking around twin boundaries

A steady wave function can be written as

$$\Psi(t) = e^{-iEt/\hbar}\Psi', \tag{4.1}$$

where E is the eigenenergy and Ψ' is time independent wave function. If $\Im(E) \neq 0$,

$$\Psi(-t)^* \neq \Psi(t), \tag{4.2}$$

which means time-reversal symmetry breaking. In other words, time-reversal symmetry is broken if the imaginary part of SC gap is finite.

The position dependence of the tunneling spectra near twin boundaries (TBs) were examined in detail by STS measurements [6]. Figure 4.10(b) shows that the quasiparticle weight near the Fermi level is almost completely removed close to TBs. This is qualitatively reproduced by a phenomenological model in which superconducting gap is represented by a sum of the isotopic component Δ_{iso} and the fourfold nodal component $\Delta_{4\phi}$. The sign of one component is reversed in two adjacent domains across TBs (Fig. 4.10(c)). If the imaginary part of $\Delta_{4\phi}$ is finite during this sign change as shown in Fig. 4.10(d), the local density of states in this model (Fig. 4.10(e)) explains observation of the node removal. When the imaginary part of the superconducting gap is finite, time-reversal symmetry is broken. It is noted that the gap nodes are affected by the TB over a distance more than $10\xi_{ab}$, where $\xi_{ab} \sim 5$ nm is the in-plane coherence length.

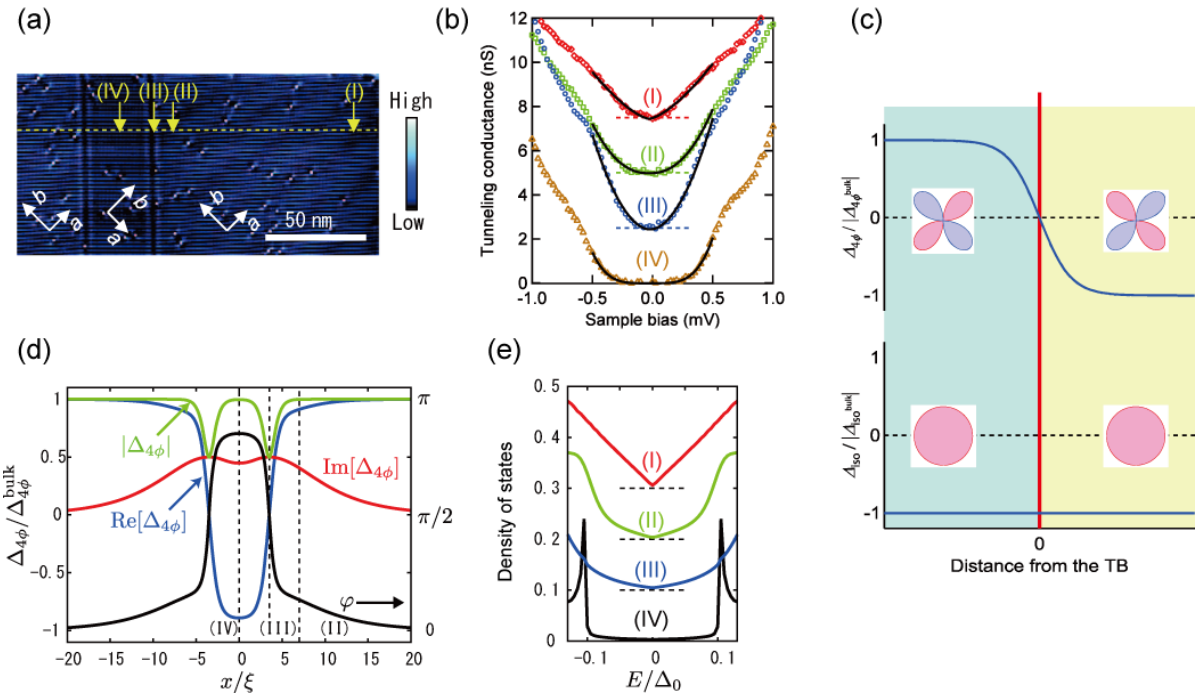

Figure 4.10: Time-reversal symmetry breaking near twin boundaries (TBs) in FeSe. (a) STM image at 1.5 K with double TBs. (b) Tunneling spectra at the representative points (I)-(IV) indicated in (a). (c) Schematic illustration of the phases of the superconducting gaps across the TB shown by the red line. The model superconducting gap is represented by a sum of the isotopic component Δ_{iso} and the fourfold nodal component $\Delta_{4\phi}$. (d) A model order parameter $\Delta_{4\phi}(x)$ with double TBs located at $x = \pm 3.5\xi$. (e) The local density of states in the bulk, (I), at $x = 7\xi$, and (II)-(IV) indicated in (d).

4.2 Motivation

As reviewed in Sec. 4.1, FeSe is an ideal material to study the relationship between nematicity and superconductivity, since it does not show antiferromagnetism like other iron-based superconductors. Also, there are disagreements about the existence of superconducting gap nodes. To study these issues, we measured the superconducting gap anisotropy at the hole Fermi surface (FS) at the Brillouin zone center by laser ARPES.

We used laser ARPES system described in Chap. 3. The overall energy resolution was set to $\sim$ 1.3 meV to obtain large photoemission counts. The error bars of the superconducting gap size were determined from the stability of E_{F} position, and evaluated to be 200 μeV.

4.3 Structural twins and polarization selection rule

Since it is important for understanding the experimental results, structural twins and polarization selection rule of ARPES are summarized in this section. The formation of twins accompanying the structural transition is summarized in Fig. 4.11. Above structural transition temperature (T_{s} = 90 K), the crystal structure is tetragonal (fourfold symmetry). The d_{zx} and d_{yz} orbitals are degenerate and the hole FS at the Γ point is circular. At T_{s}, the crystal structure becomes orthorhombic (twofold symmetric), and d_{zx} and d_{yz} orbital polarization occurs. As explained in Sec 4.1.3, this is interpreted as an orbital order derived by the electron system. For the domain with longer axis along x direction (domain 1), the FS becomes an ellipse extending in the k_y direction, and the d_{zx} orbital mainly forms the FS. There is an orthorhombic crystal rotated 90° from domain 1, which we call domain 2, because the orthorhombic crystal has an arbitrary direction in the x direction or the y direction. The formation of twins is generally unavoidable unless uniaxial strain is applied (detwinning). When measuring twinned samples, the elliptical FSs rotated 90° relative to each other are superimposed.

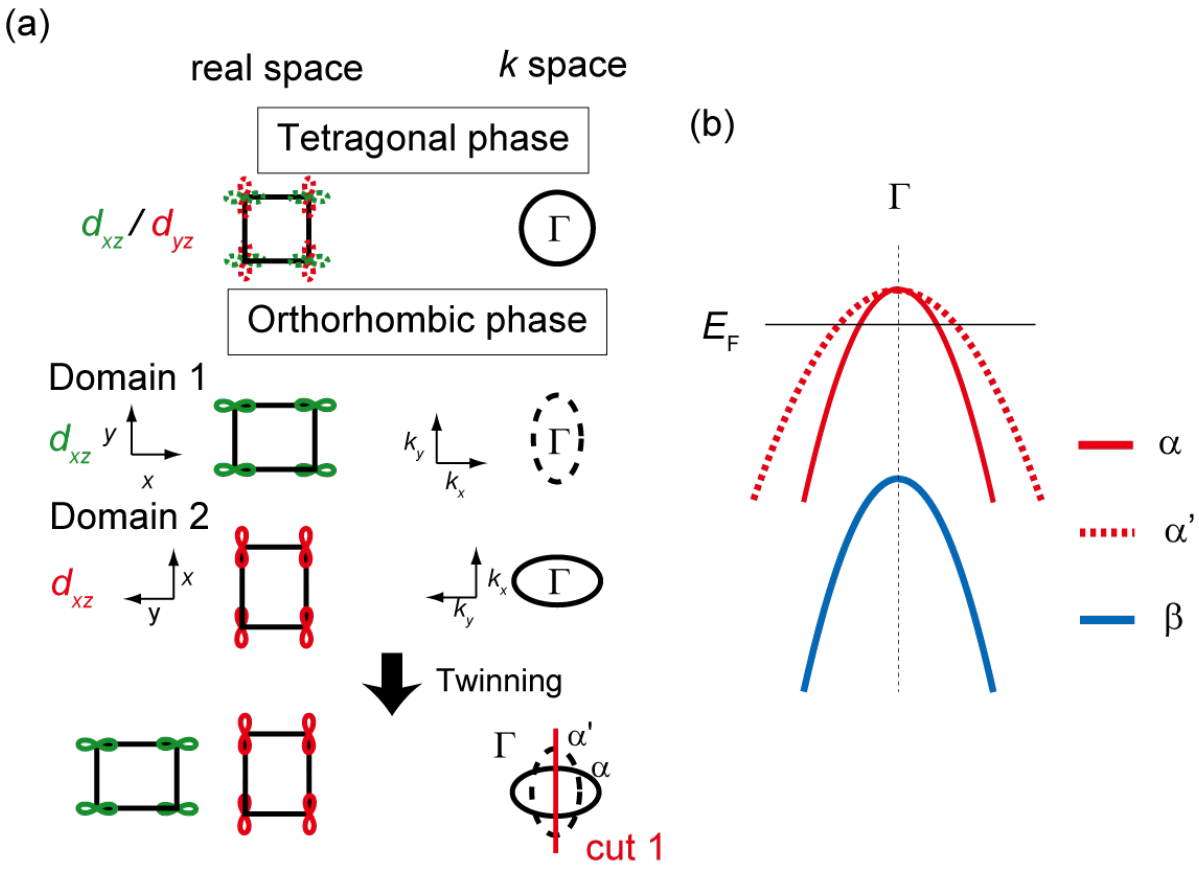

Figure 4.11: Band assignment for the twinned FeSe in the orthorhombic phase. (a) Relationship between the crystal orientation and the FS shape around the Brillouin-zone center. In the tetragonal phase, the dominant orbital character of Fe 3d is d_{xz}/d_{yz} and the FS is circular, whereas in the orthorhombic phase, the dominant orbital character is d_{xz} and the FS is elliptical. In the orthorhombic phase, the crystal is twinned and the elliptical FSs overlap. (b) Band dispersions around the zone center along the cut 1 in (a). Due to the existence of the multiple twin domains, two dispersions are observed along the cut 1, and these are labeled as α and α'. The dispersion below E_{F} is labeled as β.

The parity selection rule enables orbital-selective observations in ARPES, as explained in Sec. 2.4. The experimental configuration is shown in Fig. 4.12. We select $yz(zx)$ plane as a mirror plane for the domain 1(2), and parity is defined with regard to this mirror plane. Each iron $3d$ orbital can be classified into even or odd parity. For the domain 1, d_{zx} orbital has odd and d_{yz} orbital has even parity. When the detector slit is in the mirror plane (an analyzer normal configuration), a photoelectron which enters the detector slit has even parity. In the analyzer normal configuration, the transition matrix elements are finite only when the initial state and incident light has the same parity. p-polarized light probes d_{zx} orbital since it has odd parity portion, while s-polarized light probes only d_{yz} orbital since it has only even parity. The domain 2 is rotated to 90 degrees from the domain 1, and the parity selection rule for d_{zx} and d_{yz} becomes opposite (note that each axis is fixed to the sample).

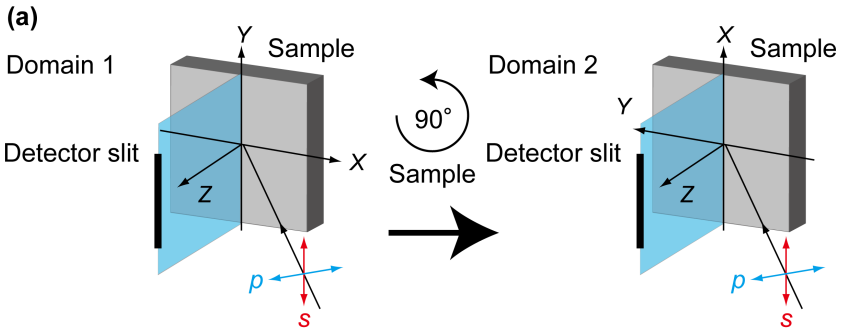

p pol.: odd + (even)

s pol.: even

(b)

	Domain 1	Domain 2
XZ	odd	even
YZ	even	odd

Figure 4.12: Experimental configuration. (a) Schematic illustration of experimental configuration for two domains below T_s. Axis of each orbital is fixed to sample. (b) Parity for each orbital in each domain.

4.4 Results

4.4.1 Comprehensive band structure

Before the main results of 7 eV laser ARPES, overall band structure is discussed in this section. Figure 4.13 shows the FS of $FeSe_{0.87}S_{0.13}$, taken with a helium discharge lamp (21.2 eV). It is a substituted material, but the characters of the band structure are similar [75]. Bands around Z (Γ) point are hole like, and those around A (M) point are electron like [57]. We focused on the hole bands at the Brillouin-zone center in the main results, since A (M) point is not accessible with low photon energy of 7 eV.

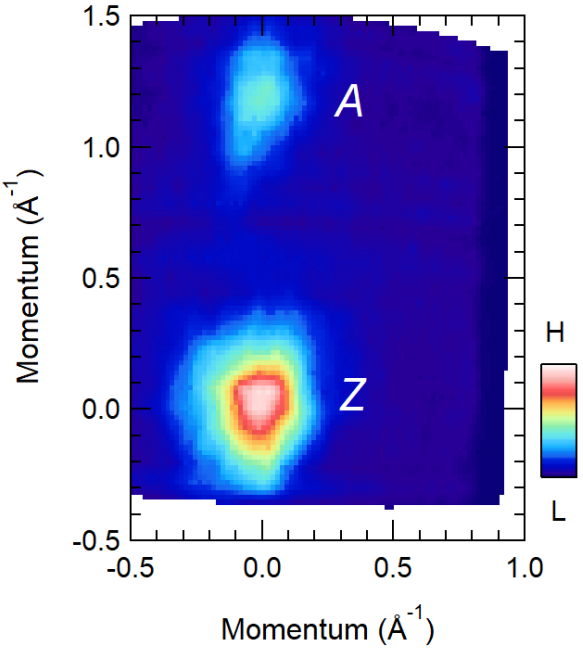

Figure 4.13: FS of $FeSe_{0.87}S_{0.13}$ observed by helium discharge lamp. Plots of the ARPES intensity at E_F as a function of the two-dimensional wavevector measured with a helium discharge lamp (21.2 eV), taken at 15 K.

To estimate k_z measured by 7 eV laser, we performed measurements at One-Cube beamline at the BESSY II light source in Germany, as shown in Fig. 4.14. Two hole bands are seen in spectra taken with 7 eV and synchrotron light source, as shown in Figs. 4.14(a)-(c). Note that hole bands originated from structural twinning are resolved in spectra taken with 7 eV. Figure 4.14(d) shows k_z dependence of energy distribution curves (EDCs) at $k_x = k_y = 0$. We determined 23 (37) eV point corresponds to Z (Γ) point, which is in good agreements in a previous report [57]. We estimated k_z position observed by 7 eV in two methods. Firstly, we compared the incident energy dependence of the hole band below $E_{\rm F}$, β band, and the results of 7 eV (18 meV below $E_{\rm F}$), as shown in Fig. 4.14(d). The β band top measured by 7 eV corresponds to that measured by 28 eV, which is between Γ and Z point but closer to Z point. Secondly, we estimated k_z by free electron approximation. From Eq. 2.19, k_z of the initial state is given by

$$\hbar k_z = \sqrt{2m(E_k \cos^2\theta + V_0)}, \tag{4.3}$$

where $E_k = \hbar\omega - \Phi - |E_{\rm B}|$ is the kinetic energy of the photoelectron, $\hbar\omega$ is the incident energy, Φ is the work function, $|E_{\rm B}|$ is the binding energy, and θ is the emission angle measured from the crystal surface normal. V_0 is the inner potential, used as a fitting parameter. Using $c = 5.521\mathring{A}^{-1}$ as the length of c-axis of the unit cell [41], k_z corresponds to vertical emission ($\theta = 0$) at $E_{\rm F}$ ($E_{\rm B} = 0$) is given by

$$\begin{aligned} k_z &= \frac{c}{\pi}\frac{\sqrt{2m}}{\hbar}\sqrt{\hbar\omega - \Phi + |E_{\rm B}| + V_0} \\ &= 0.90\sqrt{(\hbar\omega + V_0 - \Phi)\ [\text{eV}]}\ \left[\frac{\pi}{c}\right], \end{aligned} \tag{4.4}$$

If we assume $V_0 - \Phi = 8$ eV, Eq. 4.4 gives $k_z = 6.0$ (Γ point) at 37 eV, and $k_z = 5.0$ (Z point) at 23 eV. This is in good agreement with current results, as shown in Fig. 4.14(e). At 7 eV, k_z is estimated to be 3.5 (between Γ and Z point). The free electron approximation, in which photoelectrons do not interact with the sample, is not trivial in case of low energy excitation such as 7 eV. However, analysis using β band and free electron approximation are in good agreement.

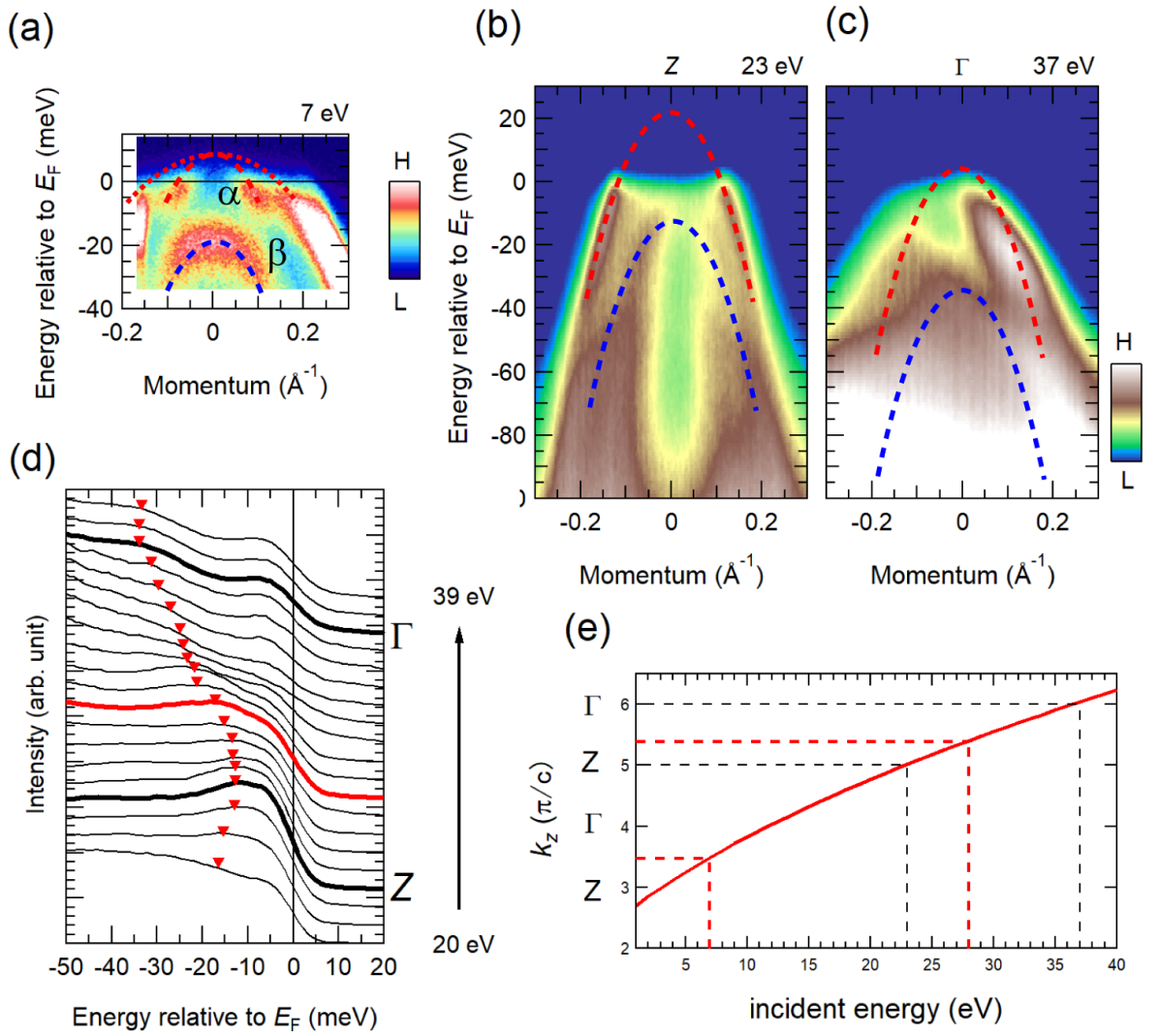

Figure 4.14: k_z dependence and estimation of k_z measured by 7 eV. (a) ARPES intensity plot parallel to Γ-M line, taken with 7 eV laser, s-polarization (L.V.), and at 25 K. Dotted curves of α and β bands are guides for the eye. (b),(c) Same as (a), but taken with synchrotron light source at 23 and 37 eV, respectively. Incident light is p-polarized (L.H.), energy resolution is 12 meV, and measurement temperature is 1.3 K. (d) Incident energy dependence of EDCs at $k_x = k_y = 0$ from 20 to 39 eV. Red triangle shows band top of β band in each spectrum. The red curve (28 eV) is estimated to be at the same k_z with that of 7 eV. (e) Incident energy dependence of k_z estimated by free electron approximation. Red dotted lines represent k_z measured by 7 and 28 eV.

4.4.2 Superconducting gap of twinned multi-domain FeSe

In this section, we examine normal state band structures and superconducting gap of twinned FeSe. Figures 4.15(c) and (f) show the FS maps at the Brillouin-zone center measured at 15 K ($> T_c$), taken with p- and s- polarized incident light. Two FSs were observed and their shapes were two-fold symmetric and elliptical. They are rotated to each other by 90 degrees and elongated along the k_y and k_x directions, respectively. Photoemission intensity of the FS elongated along the k_y (k_x) direction was higher for p- (s-) polarization. Observed polarization dependence can be explained by the orbital character of these two FSs due to twinning. Due to the parity selection rule explained in Sec. 4.3, p- (s-) polarized light predominantly observes orbital with odd (even) parity. Considering orbital components of the FS determined by the previous work [64], the FS of two domains can be selectively observed by p- (s-) polarized light as shown in Figs. 4.15(c) and (f). In Figs. 4.15(d) and (g), one can see that a hole band crosses the Fermi level (E_F) at different Fermi wavevector k_F positions for each polarization. The different k_F positions of the observed bands correspond to those of the major and minor axes of the elliptical FS. The k_F positions are determined from MDCs at E_F.

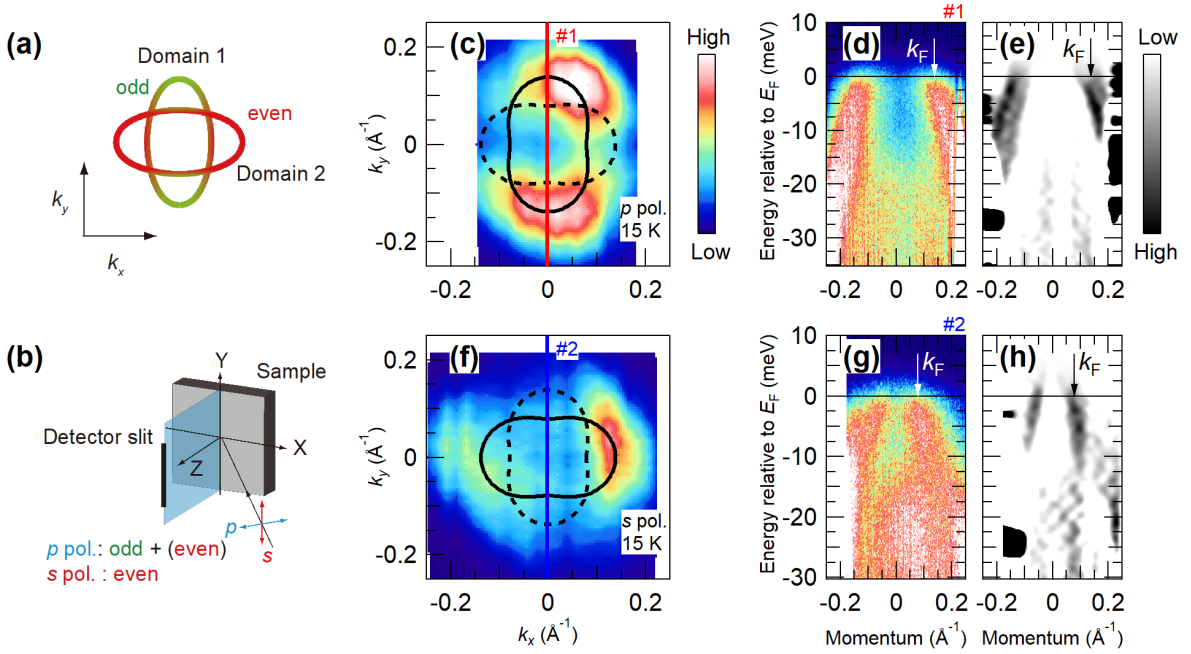

Figure 4.15: Electronic structure of the twinned FeSe at 15 K in the orbital ordered state. (a) Schematic FSs at the zone center. x and y are coordinates along the crystal axes of the orthorhombic setting. Due to the orbital ordering, two elliptical FSs are overlapped. Portions of the orbital contributions in those FSs are indicated by red and green for even and odd parity with respect to the mirror plane defined in (b), respectively. (b) Experimental configuration. A mirror plane is defined to be parallel to the detector slit. Definition of p- and s-polarized light and sample axes is shown. (c) Plots of the ARPES intensity at E_F as a function of the two-dimensional wavevector measured with p-polarized light. The intensity is obtained by integrating the spectra within $\pm$ 3 meV with respect to E_F. The experimental FS (solid ellipse) and a duplicate rotated by 90° caused by twin domains (dashed ellipse) are shown. (d) ARPES intensity plot, (e) Momentum second derivative of (d) at #1 in (c). The arrow indicates a k_F position. (f)-(h) The same as (c)-(e) but taken with s-polarized light reflecting the other domain.

Figures 4.16(b) and (e) show the EDCs at k_F below and above T_c taken with p- and s-polarized light, respectively. Each EDC is identified with a FS angle θ, and the k_F positions are shown in Figs. 4.16(a) and (d). To cancel out the effect of the Fermi-Dirac cutoff, the EDCs were symmetrized with respect to E_F, and the results are shown in Figs. 4.16(c) and (f). Sharp superconducting coherence peaks can be recognized very clearly in the spectra below T_c. The vertical dashed line in Fig. 4.16(c) indicates the peak position of the EDC at $\theta = 91°$, which is at the end of major axis of the elliptical FS. The EDC at $\theta = 61°$, for example, has a higher peak energy, indicating a finite SC gap anisotropy. In order to quantify the SC gap sizes, we fitted the spectra to the BCS spectral function and the results are shown as the solid lines (see Sec. 2.6 for details of the fitting function). The observed spectra are well reproduced by the fitting function, indicating reliability of the obtained SC gap sizes.

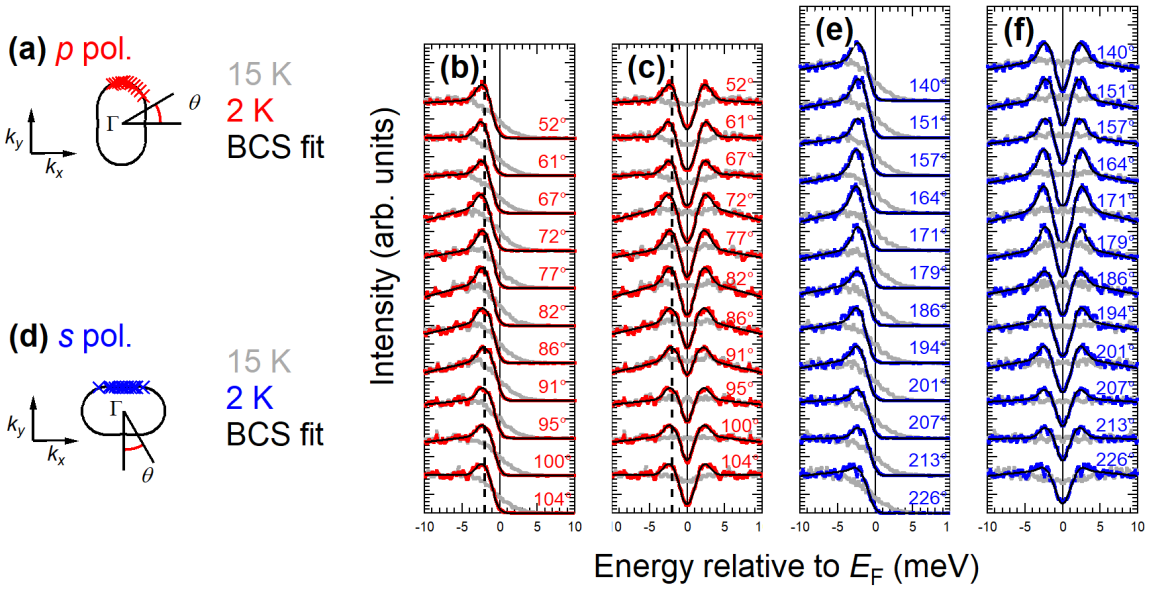

Figure 4.16: Superconducting gap anisotropy of twinned FeSe. (a) Definition of FS angle in case of p-polarized light. Red points indicate the k_F positions where EDCs in (b) and (c) are taken. (b) EDCs at various k_F points along the FS at 15 K (gray) and 2 K (red). Black lines show the fits to the BCS fitting function. FS angle defined in (a) is shown for each EDC. (c) The same as (b) but symmetrized with respect to E_F. (d)-(f) The same as (a)-(c) but taken with s-polarized light.

4.4.3 Detwinning measurements

We observed the normal state FS of single domain by detwinning, as shown in Fig. 4.17. Detwinning is the alignment of the direction of the orthorhombic crystal by applying uniaxial tensile strain to the sample [55, 64, 76]. Absence of the elliptical FS for s-polarized light, which shows a striking difference from the results for the twinned sample (Fig. 4.15), confirms that the sample was successfully detwinned. The strain necessary to detwin a crystal is estimated to be around 0.7 MPa in case of another iron-based superconductor $BaFe_2As_2$, using a Belleville washer in neutron scattering experiments [77]. We tried to obtain the gap structure of the detwinned samples, but unfortunately, we found that precise measurements to obtain the gap structure within the error bar of 200 μeV were very difficult with the detwinning device. This is probably because the stability of the Fermi level (E_F) position becomes worse and the lowest achievable temperature becomes slightly higher due to the worse electrical and thermal conductance of the sample holder attached with the detwinning device.

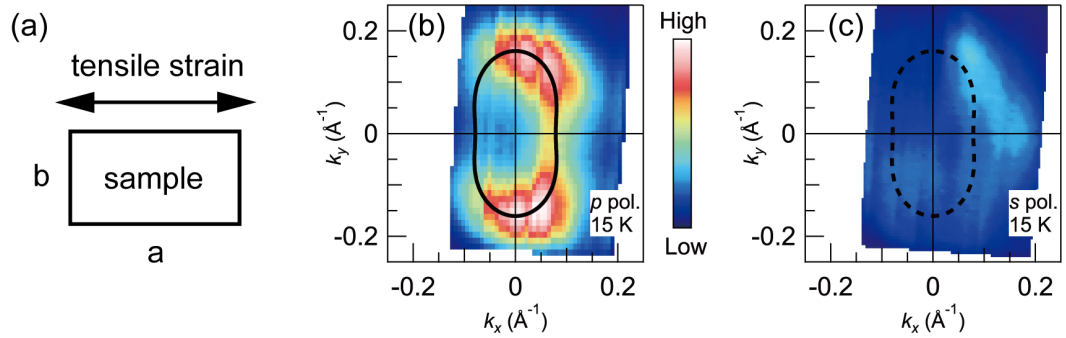

Figure 4.17: FS maps for the detwinned sample. (a) Schematic illustration of the experimental configuration. Uniaxial tensile strain was induced to the sample to align the direction of the orthorhombic crystal ($a > b$). (b) Plots of the ARPES intensity at E_F for the detwinned FeSe as a function of the two-dimensional wavevector measured with p-polarized light. The intensity is obtained by integrating the spectra within 3 meV with respect to E_F. The black ellipse indicates the experimental FS. (c) Same as (b) but taken with s-polarized light. The black dotted ellipse indicates absence of the FS.

4.4.4 Superconducting gap of single-domain FeSe

We present data of accidental single-domain sample in this section. Figure 4.18 shows the results for another sample, which has a different intensity ratio between two polarizations from Fig. 4.15. The observed FSs are shown in Figs. 4.18(a) and (b). The intensity of the FS observed by s-polarized light is much weaker compared to that by p-polarized light, and this intensity difference is similar to that of the detwinned sample shown in Fig. 4.17. By contrast, Figs. 4.15(c) and (f) show similar intensity of the FS between s- and p- polarized light. Considering this difference, the results shown in Fig. 4.18 can be interpreted as observation of the single-domain region, although any intentional uniaxial tensile strain was not applied to the sample. This is probably owing to the small laser spot size ($\sim$ 200 μm) and the large domain size of the cleaved surface. Similar results for the observation of the single-domain region has been reported for FeSe by Raman scattering [78] and ARPES [63].

Figure 4.18(d) shows the E-k image below T_c (2 K) of cut #3 indicated in Fig. 4.18(a), symmetrized with respect to E_F. This shows no detectable gap, which may demonstrate the existence of SC gap nodes. Figures 4.18(f) and (g) show the EDCs at k_F and symmetrized EDCs with respect to E_F, respectively, taken with p-polarized light. Each EDC is identified with a FS angle θ, and the momentum positions in the FS is shown in Fig. 4.18(e). It is clear from the spectra that the SC gap becomes smaller as θ reaches to 90°. Furthermore, the spectra around $\theta = 90°$ show an undetectable gap, and thus, nodes may exist around $\theta = 90°$. On the other hand, since the experimental observation limit is estimated to be $\sim$ 0.2 meV, the SC gap minimum is at least smaller than 0.2 meV.

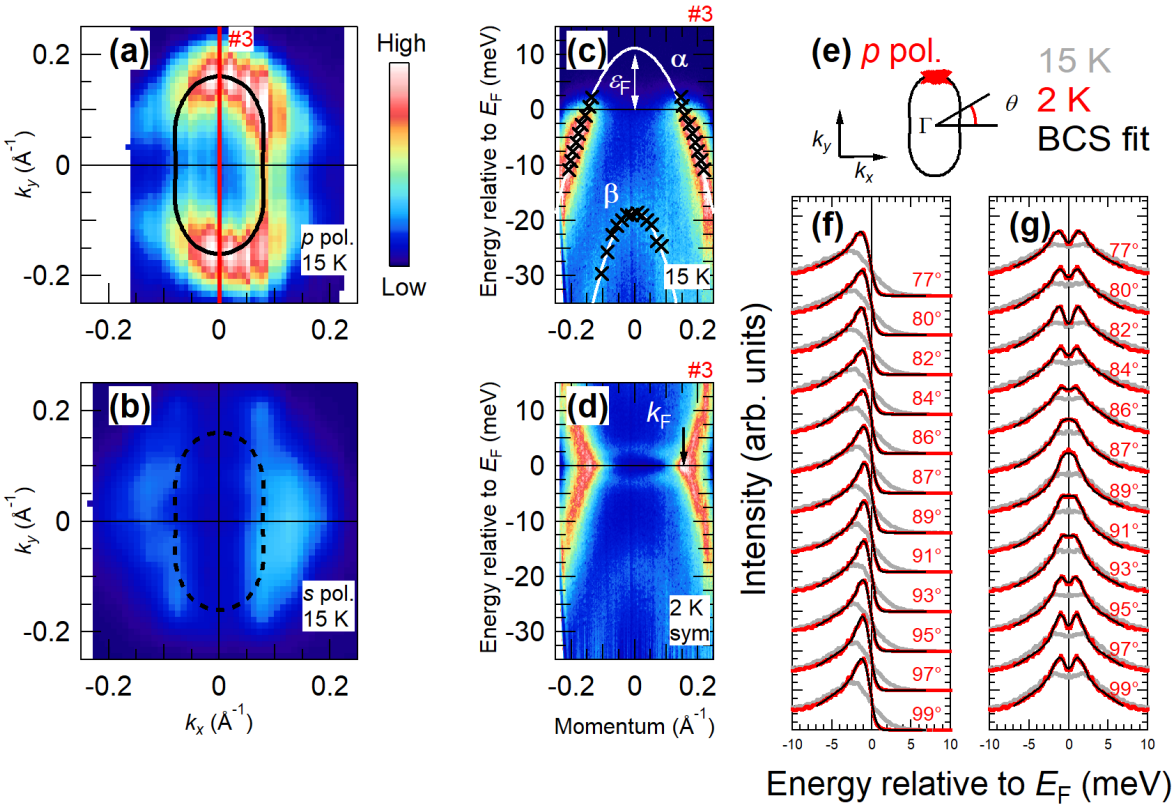

Figure 4.18: Superconducting gap anisotropy of single-domain FeSe without uniaxial tensile strain. (a) Plots of the ARPES intensity at E_F of FeSe as a function of the two-dimensional wavevector measured with p-polarized light. The intensity is obtained by integrating the spectra within 3 meV with respect to E_F. Black ellipse indicates the experimental FS. (b) Same as (a) but measured with s-polarized light. (c) ARPES intensity plot above T_c (15 K) at the momentum line shown in (a), taken with p-polarized light. Black markers represent the experimental band dispersion determined from momentum distribution curves and EDCs for the α and β band. The Fermi energy ε_F is shown for the α band. (d) The same as (c) but taken below T_c (2 K) and the data is symmetrized with respect to E_F. The black arrow indicates the k_F position. (e) Definition of FS angle. The red points indicate the k_F values where EDCs in (f) and (g) are taken. (f) EDCs at different k_F values along the FS at 15 K (gray) and 2 K (red). Black lines show the fits to the BCS fitting function. The FS angles defined in (e) is shown for each EDC. (g) Same as (f) but symmetrized at E_F.

4.4.5 Distribution of twin domains in real space

In this section, we examine the distribution of twin domains, to support our observation of accidental single domain in Sec. 4.4.4. We observed domain structures by polarization microscope [79]. Using this technique, twin boundaries can be visualized due to the difference of reflectivity along orthorhombic crystal axes. In the multi-domain sample, line structures were observed in the orthorhombic phase as shown in Fig. 4.19(c), and they are tilted by 45° to the orthorhombic crystal axes. Above T_s, the crystal becomes tetragonal, and these line structures were not observed as shown in Fig. 4.19(b). Therefore, these structures correspond to twin boundaries as reported by Tanatar *et. al.* [80]. Note that the domains smaller than 1 μm is difficult to observed by optical microscope. On the other hand, no line structure was observed in the single domain sample as shown in Fig. 4.19(e).

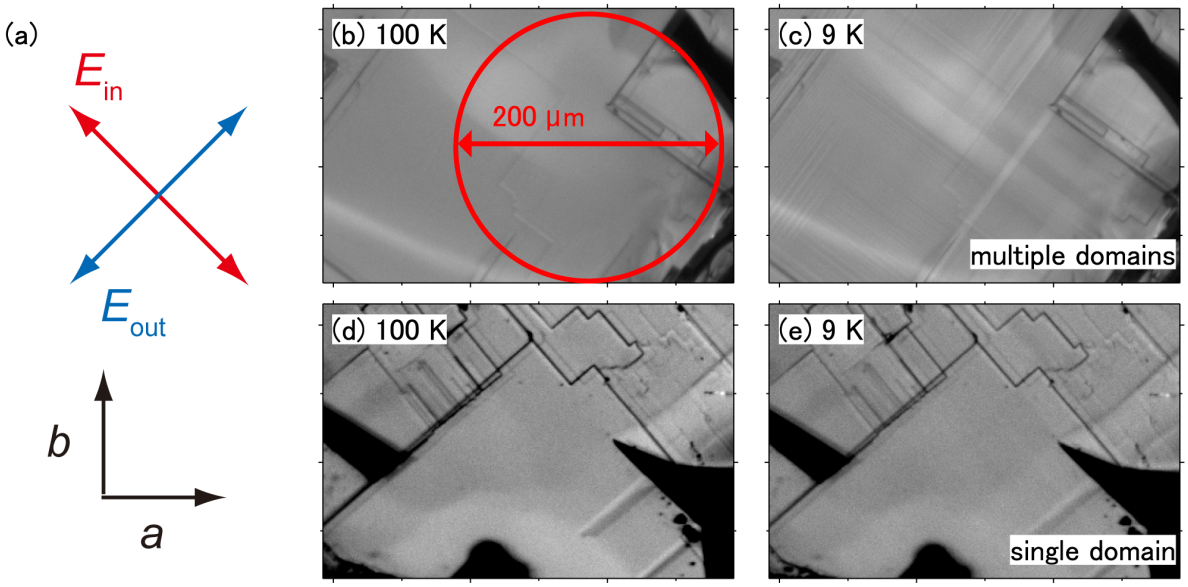

Figure 4.19: Polarization microscope images of sample surfaces. (a) Direction of polarizations for the incident and detected light with respect to the orthorhombic crystal axes. Polarizations of the incident and detected light ($E_{\rm in}$ and $E_{\rm out}$) are indicated by red and blue arrows, respectively. (b), (c) Images of the multi-domain sample taken by polarization microscope at 100 K (b) and 9 K (c), respectively. The red circle corresponds to the spot size of the incident laser ($\sim$ 200 μm). Diagonal line structures in (c) correspond to twin boundaries. (d), (e) Images of the single-domain sample at 100 K (d) and 9 K (e), respectively.

Figure 4.20 shows the position and polarization dependence of ARPES spectra. At the spot 1 schematically drawn in Fig. 4.20(g), the ARPES images taken with p- and s-polarized light show different dispersions as shown in Figs. 4.20(a) and (b), respectively, similar to the results of the multi-domain sample shown in Figs. 4.15(d) and (g). On the other hand, at the spot 2, the ARPES intensity is very weak for s-polarized light compared to p-polarized light as shown in Figs. 4.20(c) and (d). The intensity of the MDC taken at the spot 2 with s-polarized is very weak compared to the others and has no peak as shown in Figs. 4.20(e) and (f). These differences demonstrate that both of multi- and single-domain regions exist on one cleaved surface.

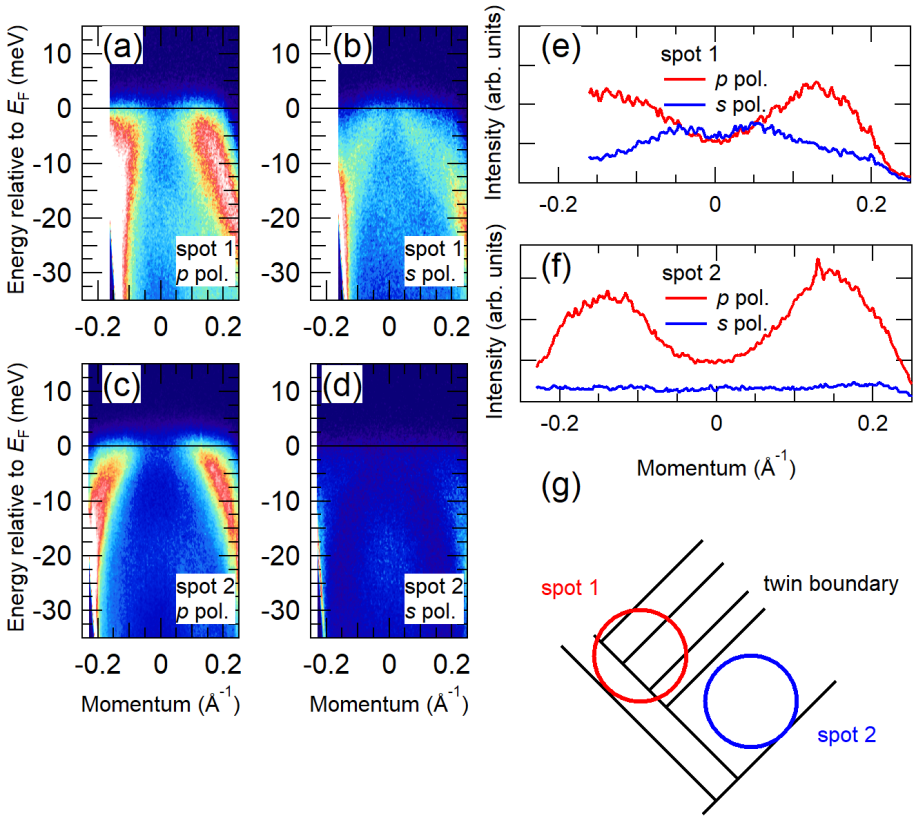

Figure 4.20: Position and polarization dependence of the ARPES spectra. (a), (b) ARPES intensity plots along the k_y direction taken at the spot 1 with p- and s- polarized light, respectively. (c), (d) Same as (a) and (b) but taken at the spot 2, which is 400 μm away from the spot 1. (e), (f) Momentum distribution curves taken with p- and s- polarized light at the spot 1 and 2, respectively. The energy integration window was $\pm$ 3 meV with respect to E_F. (g) Schematic image of the sample surface and the spots 1 and 2. The solid lines indicate twin boundaries.

4.4.6 Summary of superconducting gap anisotropy

We summarize the results of superconducting gap anisotropy in this section. Figure 4.21 shows the obtained SC gap anisotropy. The results from the multi- and single-domain samples are shown together. For the multi-domain samples, the results with p- and s-polarized light are shown together, considering that each polarization shows a higher intensity for the domain rotated to each other by 90 degrees. We fitted the results of the multi-domain samples to the following two-fold symmetric formula of the summation of harmonic series

$$\Delta(\theta) = |A + B\cos(2\theta) + C\cos(4\theta) + D\cos(6\theta) + E\cos(8\theta)|, \tag{4.5}$$

and the obtained fitting parameters were $A = 1.19$ meV, $B = 0.079$ meV, $C = 0.02$ meV, $D = 0.228$ meV, and $E =$ -0.141 meV.

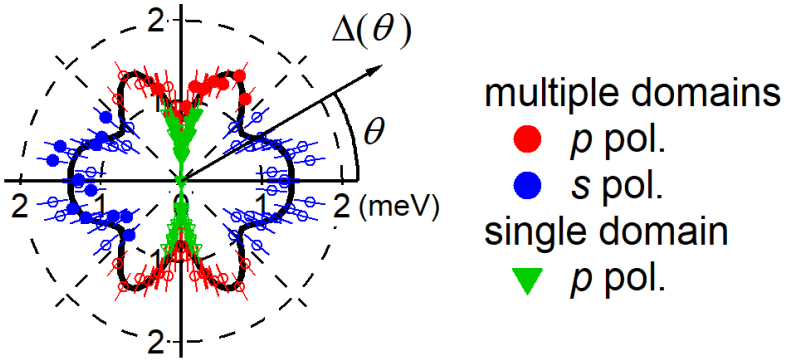

Figure 4.21: Superconducting gap anisotropy of the elliptical FS. Results of the multi-domain sample with p- (red circle) and s- (blue circle) polarized light are shown together, considering that each polarization predominantly probes different domains. Results of the single-domain sample (green triangle) are also shown. Solid symbols are obtained from BCS spectra fitting of the spectra and open symbols are symmetrized by taking into account the orthorhombic crystal symmetry. Error bars are determined by the systematic and statistical error of the calibrated E_{F} positions. The black curve is fitting of the gap anisotropy of the multi-domain samples to Eq. 4.5.

The observed SC gap anisotropy shows two major characteristics. Firstly, it shows two-fold symmetry. The orbital ordering makes the electronic structure two-fold symmetric, and the SC gap anisotropy follows the symmetry. The SC gap at $\theta = 90°$ shows a minimum, while that at $\theta = 0°$ shows a maximum. This clearly demonstrates the breaking of the four-fold symmetry of the SC gap anisotropy. Fitting of the SC gap anisotropy also shows the breaking of the four-fold symmetry as well. Secondly, the observed SC

gap anisotropy shows sharp anisotropy around $\theta = 90°$. The gap shows a sharp drop toward $\theta = 90°$. In contrast, the anisotropy becomes very weak around $\theta = 180°$. These two observations show necessity for considering the four-fold symmetry breaking due to the orbital ordering when one pursues the mechanism of superconductivity in FeSe. Additionally, there are local minima around $\theta = \pm 45°$ and $\pm 135°$. The breaking of four-fold symmetry in SC gap anisotropy is consistent with very recent reports of ARPES on similar compound $FeSe_{0.93}S_{0.07}$ [81] and Bogoliubov quasiparticle interference (BQPI) measurements on FeSe [7]. Theoretically, two-fold symmetry of SC gap anisotropy is explained based on spin fluctuations with orbital selectivity [82, 83], cooperation between spin and orbital fluctuations [84], or orbital nematic fluctuations [85].

The observed SC gap anisotropy summarized in Fig. 4.22(a) shows a considerable difference between the multi- and single-domain samples. The results for the multi-domain samples show finite gaps at any θ, while those for the single-domain samples show an undetectable gap around $\theta = 90°$. The difference of the SC gap size between the multi- and single-domain samples away from $\theta = 90°$ becomes small, and it is almost within error bars at $\theta = 80°$ and $100°$.

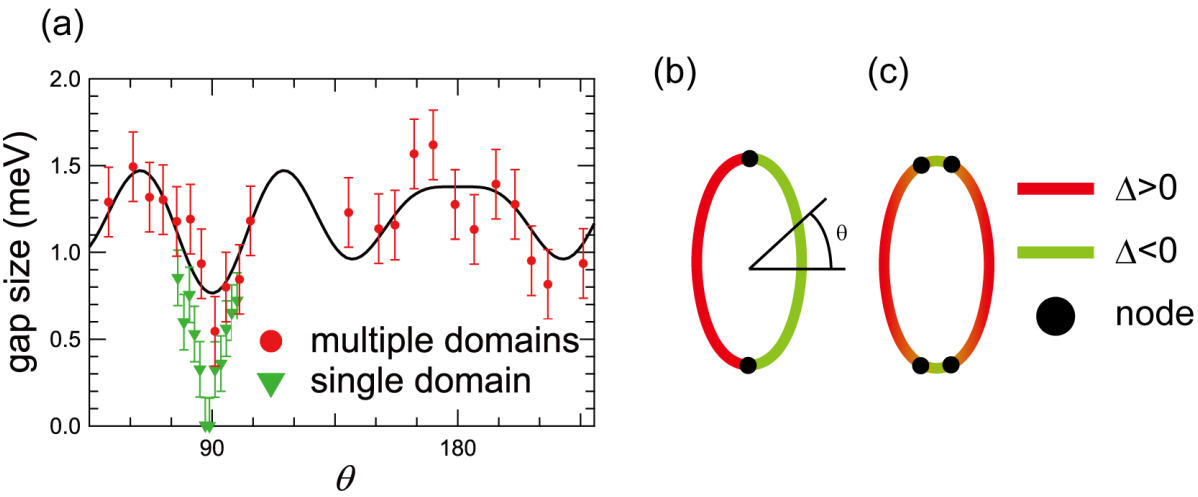

Figure 4.22: Superconducting gap anisotropy of multi- and single-domain FeSe. (a) Superconducting gap anisotropy of the elliptical FS, shown in Cartesian coordinates. Results of the multi-domain samples (red circle) and single-domain samples (green triangle) are shown together. Error bars are determined by the systematic and statistical error of the calibrated E_F positions. The black curve is fitting of the gap anistropy of the multi-domain samples to Eq. 4.5. Schematic description of gap signs on the Γ-centered FS assuming (b) a single node and (c) two nodes at each vertex of the major axis ($\theta = \pm 90°$). The Red (green) line indicates $\Delta > 0$ (< 0), and the black circles are the positions of nodes.

4.5 Discussion

We discuss the reason of the difference in superconducting gap anisotropy between multi- and single-domain samples in this section. Superconducting gap symmetry is also commented.

It is not likely that this different gap anisotropy is caused by the difference of disorder level among the pieces of samples. Teknowijoyo *et. al.* have reported from the London penetration depth measurements that the gap minimum increases by ~ 0.05 meV after introducing point-like disorder by electron irradiation [71], when the created Frenkel pairs of interstitial and vacancies is estimated to be ~ 0.05 % per Fe and per Se (0.1 % total pairs per formula). For our single crystals, the number of impurities and defects was confirmed to be less than 0.05 % per Fe by scanning tunneling microscope topography [6, 42], and thus, the increase of the gap minimum due to impurities and defects is expected to be less than ~ 0.05 meV, much smaller than the difference of the gap minimum at $\theta = 90^\circ$ between the multi- and single-domain samples (~ 0.5 meV).

Alternatively, SC gap anisotropy could be affected by existence of twin boundaries. As explained in Sec. 4.1.5, time-reversal symmetry is broken and a fully gapped state is observed over a distance several times larger than the coherence length near twin boundaries [6]. Because there should exist many twin boundaries within the laser spot for the multi-domain samples, the SC gap anisotropy for the multi-domain samples could reflect a fully gapped state due to time-reversal symmetry breaking. This could settle a contradiction between the different results of superconducting gap nodes, which is discussed in Sec. 4.1.4. Whereas measurements by several probes suggest presence of line nodes [42], other reports suggest a full gap state without superconducting gap nodes [66, 67]. This difference might be due to the density of twin boundaries. Moreover, the difference of the SC gap anisotropy between the multi- and single-domain samples around $\theta = 90^\circ$ is consistent with the theoretically calculated node disappearance due to time-reversal symmetry breaking [86]. Therefore, the difference of the SC gap anisotropy between the multi- and single-domain samples is considered as the effect of time-reversal symmetry breaking near twin boundaries.

According to the superconducting gap determined from BQPI [7], significantly anisotropic gap has been suggested for the zone-centered hole FS. Although the gap nodes were not observed by BQPI, since its reason might be due to the finite scanned area for the Fourier transform, our results should be totally consistent with the gap anisotropy determined from BQPI. If a single node is assumed at the vertex, this means that a sign change occurs at each vertex of the major axis ($\theta = \pm 90^\circ$) as schematically shown in Fig. 4.22(b). Although the signed values of the SC gap should become more continuous at $\theta = \pm 90^\circ$ in this case, the SC gap symmetry is considered as p-wave. This would be difficult to expect because there is no theoretical argument for p-wave pairing in this system and this seems inconsistent with the temperature dependence of the upper critical field [73, 74]. Thus, two nodes are assumed to exist at each vertex of the major axis ($\theta = \pm 90^\circ$) as shown in Fig. 4.22(c), similar to KFe_2As_2, which shows an

octet-line node structure where two nodes exist within the narrow FS angle range [36]. In this case, the sign changes occur twice around the vertices and the sign of the gap is consistent with the s-wave symmetry.

4.6 Summary

We performed laser ARPES measurements on single crystalline FeSe to study the superconducting gap anisotropy of the zone-centered hole FS. We observed that the four-fold symmetry is significantly broken in the superconducting gap anisotropy, which is considered to be due to the orbital ordering. We also found that the superconducting gap nodes are not observed for the multi-domain sample, but they exist at the vertices of the major axis of the elliptical FS for the single-domain sample. This is attributed to breaking of time-reversal symmetry at the twin boundaries and our results reveal the effects of time-reversal symmetry breaking on the nodal superconducting gap anisotropy.

After our paper was accepted [87], magnetic field angle-resolved specific heat measurements on gap structure of FeSe was reported [8]. Also, after the publication, ARPES measurements of superconducting gap of FeSe were reported by several groups [88–90]. All of them observed two-fold symmetric anisotropy.

5 BCS-BEC crossover in $FeSe_{1-x}S_x$

This chapter describes our research on BCS-BEC crossover in $FeSe_{1-x}S_x$. This chapter is excluded since we will publish these results in a journal in near future.

6 Conclusion

In this thesis, we present our discovery of the novel superconducting states in single crystalline $FeSe_{1-x}S_x$ arising from nematicity, by using the ultralow temperature and ultrahigh resolution laser ARPES. Followings are the main results about FeSe (Chapter 4) and $FeSe_{1-x}S_x$ (Chapter 5).

In FeSe, we observed the superconducting gap anisotropy at the Brillouin-zone center with multiple twin domains (multi-domain sample) and that with a single large domain within the laser spot (single-domain sample). It is shown that the superconducting gap anisotropy breaks four-fold symmetry, reflecting the orbital order. The superconducting gap anisotropy is different between multi- and single-domain samples, and we attributed this difference to time-reversal symmetry breaking around the twin boundaries, which has been reported in scanning tunneling spectroscopy measurements. Our results suggest that the intrinsic gap anisotropy has two nodes close to the end of the long axis of the elliptical Fermi surface. This result is the first observation of the angular dependent superconducting gap with time-reversal symmetry breaking around twin boundaries, which was enabled by the direct comparison between the data of multi- and single-domain samples.

In $FeSe_{1-x}S_x$, we found evidence of the systematic evolution of BCS-BEC crossover. The details of our findings are excluded since we will publish these results in near future.

We point out that both discoveries were made possible by high cooling power and high energy resolution of our laser ARPES system. By discovering the novel superconducting states, we demonstrated the capability of laser ARPES and the nontrivial roles that nematicity plays in iron-based superconductors. The limitation of our research, however, is that we cannot access the electron bands around the M point at the Brillouin zone corner since we used 7 eV laser. There is no ARPES system both with high energy resolution comparable to our system and high enough excitation energy to reach the M point to our knowledge. It is highly desired in near future to combine a laser with higher excitation energy, 11 eV laser [91] for example, and our knowledge of cooling system.

Bibliography

[1]M. Tinkham, *Introduction to Superconductivity*, Second edition (Dover Books on Physics, 2004).

[2]青木秀夫, **物性科学入門シリーズ　超伝導入門**, 第 2 版 (裳華房, 2010).

[3]G. R. Stewart, "Superconductivity in iron compounds", Rev. Mod. Phys. **83**, 1589–1652 (2011), https://link.aps.org/doi/10.1103/RevModPhys.83.1589.

[4]C. J. Lapp, G. Börner, and C. Timm, "Experimental consequences of Bogoliubov Fermi surfaces", Phys. Rev. B **101**, 024505 (2020), https://link.aps.org/doi/10.1103/PhysRevB.101.024505.

[5]Y. Mizukami, M. Konczykowski, Y. Kawamoto, S. Kurata, S. Kasahara, K. Hashimoto, V. Mishra, A. Kreisel, Y. Wang, P. J. Hirschfeld, Y. Matsuda, and T. Shibauchi, "Disorder-induced topological change of the superconducting gap structure in iron pnictides", Nat. Commun. **5**, 5657 (2014), http://dx.doi.org/10.1038/ncomms6657.

[6]T. Watashige, Y. Tsutsumi, T. Hanaguri, Y. Kohsaka, S. Kasahara, A. Furusaki, M. Sigrist, C. Meingast, T. Wolf, H. v. Löhneysen, T. Shibauchi, and Y. Matsuda, "Evidence for time-reversal symmetry breaking of the superconducting state near twin-boundary interfaces in FeSe revealed by scanning tunneling spectroscopy", Phys. Rev. X **5**, 031022 (2015), http://dx.doi.org/10.1103/PhysRevX.5.031022.

[7]P. O. Sprau, A. Kostin, A. Kreisel, A. E. Böhmer, V. Taufour, P. C. Canfield, S. Mukherjee, P. J. Hirschfeld, B. M. Andersen, and J. C. S. Davis, "Discovery of orbital-selective Cooper pairing in FeSe", Science **357**, 75–80 (2017), http://science.sciencemag.org/content/357/6346/75.

[8]Y. Sun, S. Kittaka, S. Nakamura, T. Sakakibara, K. Irie, T. Nomoto, K. Machida, J. Chen, and T. Tamegai, "Gap structure of FeSe determined by angle-resolved specific heat measurements in applied rotating magnetic field", Phys. Rev. B **96**, 220505 (2017), https://link.aps.org/doi/10.1103/PhysRevB.96.220505.

[9]T. Yamashita, T. Takenaka, Y. Tokiwa, J. A. Wilcox, Y. Mizukami, D. Terazawa, Y. Kasahara, S. Kittaka, T. Sakakibara, M. Konczykowski, S. Seiro, H. S. Jeevan, C. Geibel, C. Putzke, T. Onishi, H. Ikeda, A. Carrington, T. Shibauchi, and Y. Matsuda, "Fully gapped superconductivity with no sign change in the prototypical heavy-fermion $CeCu_2Si_2$", Sci. Adv. **3**, e1601667 (2017), https://advances.sciencemag.org/content/3/6/e1601667.

[10]P. Zhang, K. Yaji, T. Hashimoto, Y. Ota, T. Kondo, K. Okazaki, Z. Wang, J. Wen, G. D. Gu, H. Ding, and S. Shin, "Observation of topological superconductivity on the surface of an iron-based superconductor", Science **360**, 182–186 (2018), http://science.sciencemag.org/content/360/6385/182.

[11]D. Flötotto, Y. Ota, Y. Bai, C. Zhang, K. Okazaki, A. Tsuzuki, T. Hashimoto, J. N. Eckstein, S. Shin, and T.-C. Chiang, "Superconducting pairing of topological surface states in bismuth selenide films on niobium", Sci. Adv. **4**, eaar7214 (2018), http://advances.sciencemag.org/content/4/4/eaar7214.abstract.

[12]Y. Cao, V. Fatemi, S. Fang, K. Watanabe, T. Taniguchi, E. Kaxiras, and P. Jarillo-Herrero, "Unconventional superconductivity in magic-angle graphene superlattices", Nature **556**, 43–50 (2018), https://doi.org/10.1038/nature26160.

[13]K. Kamiya, T. Takeuchi, N. Kabeya, N. Wada, T. Ishimasa, A. Ochiai, K. Deguchi, K. Imura, and N. K. Sato, "Discovery of superconductivity in quasicrystal", Nature Communications **9**, 154 (2018), https://doi.org/10.1038/s41467-017-02667-x.

[14]A. Pustogow, Y. Luo, A. Chronister, Y.-S. Su, D. A. Sokolov, F. Jerzembeck, A. P. Mackenzie, C. W. Hicks, N. Kikugawa, S. Raghu, E. D. Bauer, and S. E. Brown, "Constraints on the superconducting order parameter in Sr_2RuO_4 from oxygen-17 nuclear magnetic resonance", Nature **574**, 72–75 (2019), https://doi.org/10.1038/s41586-019-1596-2.

[15]M. Somayazulu, M. Ahart, A. K. Mishra, Z. M. Geballe, M. Baldini, Y. Meng, V. V. Struzhkin, and R. J. Hemley, "Evidence for Superconductivity above 260 K in Lanthanum Superhydride at Megabar Pressures", Phys. Rev. Lett. **122**, 027001 (2019), https://link.aps.org/doi/10.1103/PhysRevLett.122.027001.

[16]A. P. Drozdov, P. P. Kong, V. S. Minkov, S. P. Besedin, M. A. Kuzovnikov, S. Mozaffari, L. Balicas, F. F. Balakirev, D. E. Graf, V. B. Prakapenka, E. Greenberg, D. A. Knyazev, M. Tkacz, and M. I. Eremets, "Superconductivity at 250 K in lanthanum hydride under high pressures", Nature **569**, 528–531 (2019), https://doi.org/10.1038/s41586-019-1201-8.

[17]Y. Kamihara, H. Hiramatsu, M. Hirano, R. Kawamura, H. Yanagi, T. Kamiya, and H. Hosono, "Iron-Based Layered Superconductor: LaOFeP", J. Am. Chem. Soc. **128**, 10012–10013 (2006), http://dx.doi.org/10.1021/ja063355c.

[18]Y. Kamihara, T. Watanabe, M. Hirano, and H. Hosono, "Iron-based layered superconductor $La[O_{1-x}F_x]FeAs$ ($x = 0.05$-0.12) with $T_c = 26$ K", J. Am. Chem. Soc. **130**, 3296–3297 (2008), http://dx.doi.org/10.1021/ja800073m.

[19]J. Paglione and R. L. Greene, "High-temperature superconductivity in iron-based materials", Nat. Phys. **6**, 645–658 (2010), http://dx.doi.org/10.1038/nphys1759.

[20]K. Kuroki, S. Onari, R. Arita, H. Usui, Y. Tanaka, H. Kontani, and H. Aoki, "Unconventional Pairing Originating from the Disconnected Fermi Surfaces of Superconducting $LaFeAsO_{1-x}F_x$", Phys. Rev. Lett. **101**, 087004 (2008), http://dx.doi.org/10.1103/PhysRevLett.101.087004.

[21]I. I. Mazin, D. J. Singh, M. D. Johannes, and M. H. Du, "Unconventional Superconductivity with a Sign Reversal in the Order Parameter of $LaFeAsO_{1-x}F_x$", Phys. Rev. Lett. **101**, 057003 (2008), http://dx.doi.org/10.1103/PhysRevLett.101.057003.

[22]T. Hanaguri, S. Niitaka, K. Kuroki, and H. Takagi, "Unconventional s-Wave Superconductivity in Fe(Se,Te)", Science **328**, 474–476 (2010), http://www.sciencemag.org/content/328/5977/474.abstract.

[23]A. D. Christianson, E. A. Goremychkin, R. Osborn, S. Rosenkranz, M. D. Lumsden, C. D. Malliakas, I. S. Todorov, H. Claus, D. Y. Chung, M. G. Kanatzidis, R. I. Bewley, and T. Guidi, "Unconventional superconductivity in $Ba_{0.6}K_{0.4}Fe_2As_2$ from inelastic neutron scattering", Nature **456**, 930–932 (2008), http://dx.doi.org/10.1038/nature07625.

[24]H. Kontani and S. Onari, "Orbital-Fluctuation-Mediated Superconductivity in Iron Pnictides: Analysis of the Five-Orbital Hubbard-Holstein Model", Phys. Rev. Lett. **104**, 157001 (2010), http://dx.doi.org/10.1103/PhysRevLett.104.157001.

[25]T. Shimojima, F. Sakaguchi, K. Ishizaka, Y. Ishida, T. Kiss, M. Okawa, T. Togashi, C.-T. Chen, S. Watanabe, M. Arita, K. Shimada, H. Namatame, M. Taniguchi, K. Ohgushi, S. Kasahara, T. Terashima, T. Shibauchi, Y. Matsuda, A. Chainani, and S. Shin, "Orbital-Independent Superconducting Gaps in Iron Pnictides", Science **332**, 564–567 (2011), http://dx.doi.org/10.1126/science.1202150.

[26]Y. Ota, K. Okazaki, Y. Kotani, T. Shimojima, W. Malaeb, S. Watanabe, C.-T. Chen, K. Kihou, C. H. Lee, A. Iyo, H. Eisaki, T. Saito, H. Fukazawa, Y. Kohori, and S. Shin, "Evidence for excluding the possibility of *d*-wave superconducting-gap symmetry in Ba-doped KFe_2As_2", Phys. Rev. B **89**, 081103 (2014), http://dx.doi.org/10.1103/PhysRevB.89.081103.

[27]E. Fradkin, S. A. Kivelson, M. J. Lawler, J. P. Eisenstein, and A. P. Mackenzie, "Nematic Fermi Fluids in Condensed Matter Physics", Annu. Rev. Condens. Matter Phys. **1**, 153–178 (2010), https://doi.org/10.1146/annurev-conmatphys-070909-103925.

[28]A. E. Böhmer and C. Meingast, "Electronic nematic susceptibility of iron-based superconductors", C. R. Phys. **17**, 90–112 (2015), http://dx.doi.org/10.1016/j.crhy.2015.07.001.

[29]J.-H. Chu, H.-H. Kuo, J. G. Analytis, and I. R. Fisher, "Divergent nematic susceptibility in an iron arsenide superconductor", Science **337**, 710–712 (2012), http://www.sciencemag.org/content/337/6095/710.abstract.

[30]S. Hüfner, *Photoelectron spectroscopy: principles and applications*, Third edition (Springer, 2003).

[31]高橋隆, **光電子固体物性**, 初版 (朝倉書店, 2011).

[32]A. Damascelli, Z. Hussain, and Z.-X. Shen, "Angle-resolved photoemission studies of the cuprate superconductors", Rev. Mod. Phys. **75**, 473–541 (2003), http://link.aps.org/doi/10.1103/RevModPhys.75.473.

[33]M. P. Seah and W. A. Dench, "Quantitative electron spectroscopy of surfaces: A standard data base for electron inelastic mean free paths in solids", Surf. Interface Anal. **1**, 2–11 (1979), http://dx.doi.org/10.1002/sia.740010103.

[34]D. Cahen and A. Kahn, "Electron Energetics at Surfaces and Interfaces: Concepts and Experiments", Adv. Mat. **15**, 271–277 (2003), https://onlinelibrary.wiley.com/doi/abs/10.1002/adma.200390065.

[35]R. C. Dynes, V. Narayanamurti, and J. P. Garno, "Direct Measurement of Quasiparticle-Lifetime Broadening in a Strong-Coupled Superconductor", Phys. Rev. Lett. **41**, 1509–1512 (1978), https://link.aps.org/doi/10.1103/PhysRevLett.41.1509.

[36]K. Okazaki, Y. Ota, Y. Kotani, W. Malaeb, Y. Ishida, T. Shimojima, T. Kiss, S. Watanabe, C.-T. Chen, K. Kihou, C. H. Lee, A. Iyo, H. Eisaki, T. Saito, H. Fukazawa, Y. Kohori, K. Hashimoto, T. Shibauchi, Y. Matsuda, H. Ikeda, H. Miyahara, R. Arita, A. Chainani, and S. Shin, "Octet-line node structure of superconducting order parameter in KFe_2As_2", Science **337**, 1314–1317 (2012), http://www.sciencemag.org/content/337/6100/1314.abstract.

[37]T. Kiss, F. Kanetaka, T. Yokoya, T. Shimojima, K. Kanai, S. Shin, Y. Onuki, T. Togashi, C. Zhang, C. T. Chen, and S. Watanabe, "Photoemission Spectroscopic Evidence of Gap Anisotropy in an f -Electron Superconductor", Phys. Rev. Lett. **94** (2005), http://dx.doi.org/10.1103/PhysRevLett.94.057001.

[38]T. Kiss, T. Shimojima, K. Ishizaka, A. Chainani, T. Togashi, T. Kanai, X.-Y. Wang, C.-T. Chen, S. Watanabe, and S. Shin, "A versatile system for ultrahigh resolution, low temperature, and polarization dependent Laser-angle-resolved photoemission spectroscopy", Rev. Sci. Instrum. **79**, 023106 (2008), http://dx.doi.org/10.1063/1.2839010.

[39]T. Shimojima, K. Okazaki, and S. Shin, "Low-temperature and high-energy-resolution laser photoemission spectroscopy", J. Phys. Soc. Jpn. **84**, 072001 (2015), http://dx.doi.org/10.7566/JPSJ.84.072001.

[40]F.-C. Hsu, J.-Y. Luo, K.-W. Yeh, T.-K. Chen, T.-W. Huang, P. M. Wu, Y.-C. Lee, Y.-L. Huang, Y.-Y. Chu, D.-C. Yan, and M.-K. Wu, "Superconductivity in the PbO-type structure α-FeSe", Proc. Natl. Acad. Sci. USA **105**, 14262–14264 (2008), http://www.pnas.org/content/105/38/14262.abstract.

[41]A. E. Böhmer, F. Hardy, F. Eilers, D. Ernst, P. Adelmann, P. Schweiss, T. Wolf, and C. Meingast, "Lack of coupling between superconductivity and orthorhombic distortion in stoichiometric single-crystalline FeSe", Phys. Rev. B **87**, 180505 (2013), http://dx.doi.org/10.1103/PhysRevB.87.180505.

[42]S. Kasahara, T. Watashige, T. Hanaguri, Y. Kohsaka, T. Yamashita, Y. Shimoyama, Y. Mizukami, R. Endo, H. Ikeda, K. Aoyama, T. Terashima, S. Uji, T. Wolf, H. von Löhneysen, T. Shibauchi, and Y. Matsuda, "Field-induced superconducting phase of FeSe in the BCS-BEC cross-over", Proc. Natl. Acad. Sci. USA **111**, 16309–16313 (2014), http://dx.doi.org/10.1073/pnas.1413477111.

[43]S. Medvedev, T. M. McQueen, I. A. Troyan, T. Palasyuk, M. I. Eremets, R. J. Cava, S. Naghavi, F. Casper, V. Ksenofontov, G. Wortmann, and C. Felser, "Electronic and magnetic phase diagram of β-$Fe_{1.01}Se$ with superconductivity at 36.7 K under pressure", Nat. Mater. **8**, 630–633 (2009), http://dx.doi.org/10.1038/NMAT2491.

[44]S. He, J. He, W. Zhang, L. Zhao, D. Liu, X. Liu, D. Mou, Y.-B. Ou, Q.-Y. Wang, Z. Li, L. Wang, Y. Peng, Y. Liu, C. Chen, L. Yu, G. Liu, X. Dong, J. Zhang, C. Chen, Z. Xu, X. Chen, X. Ma, Q. Xue, and X. J. Zhou, "Phase diagram and electronic indication of high-temperature superconductivity at 65K in single-layer FeSe films", Nat. Mater. **12**, 605–610 (2013), http://dx.doi.org/10.1038/nmat3648.

[45]M. Burrard-Lucas, D. G. Free, S. J. Sedlmaier, J. D. Wright, S. J. Cassidy, Y. Hara, A. J. Corkett, T. Lancaster, P. J. Baker, S. J. Blundell, and S. J. Clarke, "Enhancement of the superconducting transition temperature of FeSe by intercalation of a molecular spacer layer", Nat. Mater. **12**, 15–19 (2013), http://dx.doi.org/10.1038/nmat3464.

[46]S. Hosoi, K. Matsuura, K. Ishida, H. Wang, Y. Mizukami, T. Watashige, S. Kasahara, Y. Matsuda, and T. Shibauchi, "Nematic quantum critical point without magnetism in $FeSe_{1-x}S_x$ superconductors", Proc. Natl. Acad. Sci. USA **113**, 8139–8143 (2016), http://www.pnas.org/content/113/29/8139.abstract.

[47]T. M. McQueen, A. J. Williams, P. W. Stephens, J. Tao, Y. Zhu, V. Ksenofontov, F. Casper, C. Felser, and R. J. Cava, "Tetragonal-to-orthorhombic structural phase transition at 90 K in the superconductor $Fe_{1.01}Se$", Phys. Rev. Lett. **103**, 057002 (2009), http://dx.doi.org/10.1103/PhysRevLett.103.057002.

[48]M. Yi, D. Lu, J.-H. Chu, J. G. Analytis, A. P. Sorini, A. F. Kemper, B. Moritz, S.-K. Mo, R. G. Moore, M. Hashimoto, W.-S. Lee, Z. Hussain, T. P. Devereaux, I. R. Fisher, and Z.-X. Shen, "Symmetry-breaking orbital anisotropy observed for detwinned $Ba(Fe_{1-x}Co_x)_2As_2$ above the spin density wave transition", Proc. Natl. Acad. Sci. USA **108**, 6878–6883 (2011), http://www.pnas.org/content/108/17/6878.abstract.

[49]M. Yi, D. H. Lu, R. G. Moore, K. Kihou, C.-H. Lee, A. Iyo, H. Eisaki, T. Yoshida, A. Fujimori, and Z.-X. Shen, "Electronic reconstruction through the structural and magnetic transitions in detwinned NaFeAs", New J. Phys. **14**, 073019 (2012), http://stacks.iop.org/1367-2630/14/i=7/a=073019.

[50]J. K. Glasbrenner, I. I. Mazin, H. O. Jeschke, P. J. Hirschfeld, R. M. Fernandes, and R. Valentí, "Effect of magnetic frustration on nematicity and superconductivity in iron chalcogenides", Nat. Phys. **11**, 953–958 (2015), http://dx.doi.org/10.1038/NPHYS3434.

[51]F. Wang, S. A. Kivelson, and D.-H. Lee, "Nematicity and quantum paramagnetism in FeSe", Nat. Phys. **11**, 959–963 (2015), https://doi.org/10.1038/nphys3456.

[52]A. Subedi, L. Zhang, D. J. Singh, and M. H. Du, "Density functional study of FeS, FeSe, and FeTe: Electronic structure, magnetism, phonons, and superconductivity", Phys. Rev. B **78**, 134514 (2008), http://dx.doi.org/10.1103/PhysRevB.78.134514.

[53]J. Maletz, V. B. Zabolotnyy, D. V. Evtushinsky, S. Thirupathaiah, A. U. B. Wolter, L. Harnagea, A. N. Yaresko, A. N. Vasiliev, D. A. Chareev, A. E. Böhmer, F. Hardy, T. Wolf, C. Meingast, E. D. L. Rienks, B. Büchner, and S. V. Borisenko, "Unusual band renormalization in the simplest iron-based superconductor $FeSe_{1-x}$", Phys. Rev. B **89**, 220506 (2014), http://dx.doi.org/10.1103/PhysRevB.89.220506.

[54]M. D. Watson, T. K. Kim, L. C. Rhodes, M. Eschrig, M. Hoesch, A. A. Haghighirad, and A. I. Coldea, "Evidence for unidirectional nematic bond ordering in FeSe", Phys. Rev. B **94**, 201107 (2016), http://link.aps.org/doi/10.1103/PhysRevB.94.201107.

[55]T. Shimojima, Y. Suzuki, T. Sonobe, A. Nakamura, M. Sakano, J. Omachi, K. Yoshioka, M. Kuwata-Gonokami, K. Ono, H. Kumigashira, A. E. Böhmer, F. Hardy, T. Wolf, C. Meingast, H. v. Löhneysen, H. Ikeda, and K. Ishizaka, "Lifting of xz/yz orbital degeneracy at the structural transition in detwinned FeSe", Phys. Rev. B **90**, 121111 (2014), http://dx.doi.org/10.1103/PhysRevB.90.121111.

[56]P. Zhang, T. Qian, P. Richard, X. P. Wang, H. Miao, B. Q. Lv, B. B. Fu, T. Wolf, C. Meingast, X. X. Wu, Z. Q. Wang, J. P. Hu, and H. Ding, "Observation of two distinct d_{xz}/d_{yz} band splittings in FeSe", Phys. Rev. B **91**, 214503 (2015), http://dx.doi.org/10.1103/PhysRevB.91.214503.

[57]M. D. Watson, T. K. Kim, A. A. Haghighirad, N. R. Davies, A. McCollam, A. Narayanan, S. F. Blake, Y. L. Chen, S. Ghannadzadeh, A. J. Schofield, M. Hoesch, C. Meingast, T. Wolf, and A. I. Coldea, "Emergence of the nematic electronic state in FeSe", Phys. Rev. B **91**, 155106 (2015), http://dx.doi.org/10.1103/PhysRevB.91.155106.

[58]K. Nakayama, Y. Miyata, G. N. Phan, T. Sato, Y. Tanabe, T. Urata, K. Tanigaki, and T. Takahashi, "Reconstruction of Band Structure Induced by Electronic Nematicity in an FeSe Superconductor", Phys. Rev. Lett. **113**, 237001 (2014), http://dx.doi.org/10.1103/PhysRevLett.113.237001.

[59]L. Fanfarillo, J. Mansart, P. Toulemonde, H. Cercellier, P. Le Fèvre, F. Bertran, B. Valenzuela, L. Benfatto, and V. Brouet, "Orbital-dependent Fermi surface shrinking as a fingerprint of nematicity in FeSe", Phys. Rev. B **94**, 155138 (2016), http://link.aps.org/doi/10.1103/PhysRevB.94.155138.

[60]S. Huh, J. Seo, B. Kim, S. Cho, J. Jung, S. Kim, Y. Koh, C. Kwon, J. Kim, W. Kyung, J. D. Denlinger, Y. Kim, B. Chae, N. Kim, Y. Kim, and C. Kim, "Lifted electron pocket and reversed orbital occupancy imbalance in FeSe", ArXiv e-prints (2019), https://arxiv.org/abs/1903.08360.

[61]M. Yi, H. Pfau, Y. Zhang, Y. He, H. Wu, T. Chen, Z. R. Ye, M. Hashimoto, R. Yu, Q. Si, D.-H. Lee, P. Dai, Z.-X. Shen, D. H. Lu, and R. J. Birgeneau, "Nematic Energy Scale and the Missing Electron Pocket in FeSe", Phys. Rev. X **9**, 041049 (2019), https://link.aps.org/doi/10.1103/PhysRevX.9.041049.

[62]A. Fedorov, A. Yaresko, T. K. Kim, Y. Kushnirenko, E. Haubold, T. Wolf, M. Hoesch, A. Grüneis, B. Büchner, and S. V. Borisenko, "Effect of nematic ordering on electronic structure of FeSe", Sci. Rep. **6**, 36834 (2016), http://dx.doi.org/10.1038/srep36834.

[63]M. D. Watson, A. A. Haghighirad, L. C. Rhodes, M. Hoesch, and T. K. Kim, "Electronic anisotropies revealed by detwinned angle-resolved photo-emission spectroscopy measurements of FeSe", New J. Phys. **19**, 103021 (2017), http://stacks.iop.org/1367-2630/19/i=10/a=103021.

[64]Y. Suzuki, T. Shimojima, T. Sonobe, A. Nakamura, M. Sakano, H. Tsuji, J. Omachi, K. Yoshioka, M. Kuwata-Gonokami, T. Watashige, R. Kobayashi, S. Kasahara, T. Shibauchi, Y. Matsuda, Y. Yamakawa, H. Kontani, and K. Ishizaka, "Momentum-dependent sign inversion of orbital order in superconducting FeSe", Phys. Rev. B **92**, 205117 (2015), http://dx.doi.org/10.1103/PhysRevB.92.205117.

[65]Y. Zhang, C. He, Z. R. Ye, J. Jiang, F. Chen, M. Xu, Q. Q. Ge, B. P. Xie, J. Wei, M. Aeschlimann, X. Y. Cui, M. Shi, J. P. Hu, and D. L. Feng, "Symmetry breaking via orbital-dependent reconstruction of electronic structure in detwinned NaFeAs", Phys. Rev. B **85**, 085121 (2012), http://dx.doi.org/10.1103/PhysRevB.85.085121.

[66]L. Jiao, C.-L. Huang, S. Rößler, C. Koz, U. K. Rößler, U. Schwarz, and S. Wirth, "Superconducting gap structure of FeSe", Sci. Rep. **7**, 44024 (2017), http://dx.doi.org/10.1038/srep44024.

[67]P. Bourgeois-Hope, S. Chi, D. A. Bonn, R. Liang, W. N. Hardy, T. Wolf, C. Meingast, N. Doiron-Leyraud, and L. Taillefer, "Thermal conductivity of the iron-based superconductor FeSe: nodeless gap with a strong two-band character", Phys. Rev. Lett. **117**, 097003 (2016), http://link.aps.org/doi/10.1103/PhysRevLett.117.097003.

[68]J. K. Dong, T. Y. Guan, S. Y. Zhou, X. Qiu, L. Ding, C. Zhang, U. Patel, Z. L. Xiao, and S. Y. Li, "Multigap nodeless superconductivity in $FeSe_x$: Evidence from quasiparticle heat transport", Phys. Rev. B **80**, 024518 (2009), http://dx.doi.org/10.1103/PhysRevB.80.024518.

[69]C.-L. Song, Y.-L. Wang, P. Cheng, Y.-P. Jiang, W. Li, T. Zhang, Z. Li, K. He, L. Wang, J.-F. Jia, H.-H. Hung, C. Wu, X. Ma, X. Chen, and Q.-K. Xue, "Direct Observation of Nodes and Twofold Symmetry in FeSe Superconductor", Science **332**, 1410–1413 (2011), http://dx.doi.org/10.1126/science.1202226.

[70]L. Wang, F. Hardy, T. Wolf, P. Adelmann, R. Fromknecht, P. Schweiss, and C. Meingast, "Superconductivity-enhanced nematicity and "s+d" gap symmetry in $Fe(Se_{1-x}S_x)$", Phys. Status Solidi B (2016), http://dx.doi.org/10.1002/pssb.201600153.

[71]S. Teknowijoyo, K. Cho, M. A. Tanatar, J. Gonzales, A. E. Böhmer, O. Cavani, V. Mishra, P. J. Hirschfeld, S. L. Bud'ko, P. C. Canfield, and R. Prozorov, "Enhancement of superconducting transition temperature by pointlike disorder and anisotropic energy gap in FeSe single crystals", Phys. Rev. B **94**, 064521 (2016), http://link.aps.org/doi/10.1103/PhysRevB.94.064521.

[72]M. Li, N. R. Lee-Hone, S. Chi, R. Liang, W. N. Hardy, D. A. Bonn, E. Girt, and D. M. Broun, "Superfluid density and microwave conductivity of FeSe superconductor: ultra-long-lived quasiparticles and extended s -wave energy gap", New J. Phys. **18**, 082001 (2016), http://stacks.iop.org/1367-2630/18/i=8/a=082001.

[73]S. I. Vedeneev, B. A. Piot, D. K. Maude, and A. V. Sadakov, "Temperature dependence of the upper critical field of FeSe single crystals", Phys. Rev. B **87**, 134512 (2013), http://link.aps.org/doi/10.1103/PhysRevB.87.134512.

[74]T. Terashima, N. Kikugawa, A. Kiswandhi, E.-S. Choi, J. S. Brooks, S. Kasahara, T. Watashige, H. Ikeda, T. Shibauchi, Y. Matsuda, T. Wolf, A. E. Böhmer, F. Hardy, C. Meingast, H. v. Löhneysen, M.-T. Suzuki, R. Arita, and S. Uji, "Anomalous Fermi surface in FeSe seen by Shubnikov de Haas oscillation measurements", Phys. Rev. B **90**, 133517 (2014), http://dx.doi.org/10.1103/PhysRevB.90.144517.

[75]M. D. Watson, T. K. Kim, A. A. Haghighirad, S. F. Blake, N. R. Davies, M. Hoesch, T. Wolf, and A. I. Coldea, "Suppression of orbital ordering by chemical pressure in $FeSe_{1-x}S_x$", Phys. Rev. B **92**, 121108 (2015), http://dx.doi.org/10.1103/PhysRevB.92.121108.

[76]Y. Kim, H. Oh, C. Kim, D. Song, W. Jung, B. Kim, H. J. Choi, C. Kim, B. Lee, S. Khim, H. Kim, K. Kim, J. Hong, and Y. Kwon, "Electronic structure of detwinned $BaFe_2As_2$ from photoemission and first principles", Phys. Rev. B **83**, 064509 (2011), http://dx.doi.org/10.1103/PhysRevB.83.064509.

[77]C. Dhital, Z. Yamani, W. Tian, J. Zeretsky, A. S. Sefat, Z. Wang, R. J. Birgeneau, and S. D. Wilson, "Effect of Uniaxial Strain on the Structural and Magnetic Phase Transitions in $BaFe_2As_2$", Phys. Rev. Lett. **108**, 087001 (2012), http://link.aps.org/doi/10.1103/PhysRevLett.108.087001.

[78]Y. Hu, X. Ren, R. Zhang, H. Luo, S. Kasahara, T. Watashige, T. Shibauchi, P. Dai, Y. Zhang, Y. Matsuda, and Y. Li, "Nematic magnetoelastic effect contrasted between $Ba(Fe_{1-x}Co_x)_2As_2$ and FeSe", Phys. Rev. B **93**, 060504 (2016), http://link.aps.org/doi/10.1103/PhysRevB.93.060504.

[79]M. Tokunaga, T. Kihara, Y. Mizuguchi, and Y. Takano, "Field-Induced Magnetostructural Transitions in Antiferromagnetic $Fe_{1+y}Te_{1-x}S_x$", J. Phys. Soc. Jpn. **81**, 063703 (2012), http://dx.doi.org/10.1143/JPSJ.81.063703.

[80]M. A. Tanatar, A. E. Böhmer, E. I. Timmons, M. Schütt, G. Drachuck, V. Taufour, K. Kothapalli, A. Kreyssig, S. L. Bud'ko, P. C. Canfield, R. M. Fernandes, and R. Prozorov, "Origin of the Resistivity Anisotropy in the Nematic Phase of FeSe", Phys. Rev. Lett. **117**, 127001 (2016), http://link.aps.org/doi/10.1103/PhysRevLett.117.127001.

[81]H. C. Xu, X. H. Niu, D. F. Xu, J. Jiang, Q. Yao, Q. Y. Chen, Q. Song, M. Abdel-Hafiez, D. A. Chareev, A. N. Vasiliev, Q. S. Wang, H. L. Wo, J. Zhao, R. Peng, and D. L. Feng, "Highly anisotropic and twofold symmetric superconducting gap in nematically ordered $FeSe_{0.93}S_{0.07}$", Phys. Rev. Lett. **117**, 157003 (2016), http://link.aps.org/doi/10.1103/PhysRevLett.117.157003.

[82]A. Kreisel, B. M. Andersen, P. O. Sprau, A. Kostin, J. C. S. Davis, and P. J. Hirschfeld, "Orbital selective pairing and gap structures of iron-based superconductors", Phys. Rev. B **95**, 174504 (2017), https://link.aps.org/doi/10.1103/PhysRevB.95.174504.

[83]J.-H. She, M. J. Lawler, and E.-A. Kim, "Quantum Spin Liquid Intertwining Nematic and Superconducting Order in FeSe", Phys. Rev. Lett. **121**, 237002 (2018), https://link.aps.org/doi/10.1103/PhysRevLett.121.237002.

[84]Y. Yamakawa and H. Kontani, "Nematicity, magnetism, and superconductivity in FeSe under pressure: Unified explanation based on the self-consistent vertex correction theory", Phys. Rev. B **96**, 144509 (2017), https://link.aps.org/doi/10.1103/PhysRevB.96.144509.

[85]T. Agatsuma and H. Yamase, "Structure of the pairing gap from orbital nematic fluctuations", Phys. Rev. B **94**, 214505 (2016), http://link.aps.org/doi/10.1103/PhysRevB.94.214505.

[86]S. Maiti and A. V. Chubukov, "$s + is$ state with broken time-reversal symmetry in Fe-based superconductors", Phys. Rev. B **87**, 144511 (2013), http://link.aps.org/doi/10.1103/PhysRevB.87.144511.

[87]T. Hashimoto, Y. Ota, H. Q. Yamamoto, Y. Suzuki, T. Shimojima, S. Watanabe, C. Chen, S. Kasahara, Y. Matsuda, T. Shibauchi, K. Okazaki, and S. Shin, "Superconducting gap anisotropy sensitive to nematic domains in FeSe", Nat. Commun. **9**, 282 (2018), https://doi.org/10.1038/s41467-017-02739-y.

[88]Y. S. Kushnirenko, A. V. Fedorov, E. Haubold, S. Thirupathaiah, T. Wolf, S. Aswartham, I. Morozov, T. K. Kim, B. Büchner, and S. V. Borisenko, "Three-dimensional superconducting gap in FeSe from angle-resolved photoemission spectroscopy", Phys. Rev. B **97**, 180501 (2018), https://link.aps.org/doi/10.1103/PhysRevB.97.180501.

[89]D. Liu, C. Li, J. Huang, B. Lei, L. Wang, X. Wu, B. Shen, Q. Gao, Y. Zhang, X. Liu, Y. Hu, Y. Xu, A. Liang, J. Liu, P. Ai, L. Zhao, S. He, L. Yu, G. Liu, Y. Mao, X. Dong, X. Jia, F. Zhang, S. Zhang, F. Yang, Z. Wang, Q. Peng, Y. Shi, J. Hu, T. Xiang, X. Chen, Z. Xu, C. Chen, and X. J. Zhou, "Orbital Origin of Extremely Anisotropic Superconducting Gap in Nematic Phase of FeSe Superconductor", Phys. Rev. X **8**, 031033 (2018), https://link.aps.org/doi/10.1103/PhysRevX.8.031033.

[90]L. C. Rhodes, M. D. Watson, A. A. Haghighirad, D. V. Evtushinsky, M. Eschrig, and T. K. Kim, "Scaling of the superconducting gap with orbital character in FeSe", Phys. Rev. B **98**, 180503 (2018), https://link.aps.org/doi/10.1103/PhysRevB.98.180503.

[91]Y. He, I. M. Vishik, M. Yi, S. Yang, Z. Liu, J. J. Lee, S. Chen, S. N. Rebec, D. Leuenberger, A. Zong, C. M. Jefferson, R. G. Moore, P. S. Kirchmann, A. J. Merriam, and Z.-X. Shen, "Invited Article: High resolution angle resolved photoemission with tabletop 11 eV laser", Rev. Sci. Instrum. **87**, 011301 (2016), https://doi.org/10.1063/1.4939759.

Publication list

[1] **T. Hashimoto**, Y. Ota, H. Q. Yamamoto, Y. Suzuki, T. Shimojima, S. Watanabe, C. Chen, S. Kasahara, Y. Matsuda, T. Shibauchi, K. Okazaki and S. Shin, "Superconducting gap anisotropy sensitive to nematic domains in FeSe", Nat. Commun. **9**, 282 (2018).
https://doi.org/10.1038/s41467-017-02739-y.

[2] P. Zhang, K. Yaji, **T. Hashimoto**, Y. Ota, T. Kondo, K. Okazaki, Z. Wang, J. Wen, G. D. Gu, H. Ding and S. Shin, "Observation of topological superconductivity on the surface of an iron-based superconductor", Science **360**, 182–186 (2018).
http://science.sciencemag.org/content/360/6385/182.

[3] D. Flötotto, Y. Ota, Y. Bai, C. Zhang, K. Okazaki, A. Tsuzuki, **T. Hashimoto**, J. N. Eckstein, S. Shin and T.-C. Chiang, "Superconducting pairing of topological surface states in bismuth selenide films on niobium", Sci. Adv. **4**, eaar7214 (2018).
http://advances.sciencemag.org/content/4/4/eaar7214.

[4] T. Suzuki, T. Someya, **T. Hashimoto**, S. Michimae, M. Watanabe, M. Fujisawa, T. Kanai, N. Ishii, J. Itatani, S. Kasahara, Y. Matsuda, T. Shibauchi, K. Okazaki and S. Shin, "Photoinduced possible superconducting state with long-lived disproportionate band filling in FeSe", Commun. Phys. **2**, 115 (2019).
https://doi.org/10.1038/s42005-019-0219-4.

Acknowledgement

I would like to thank the many collaborators and friends who have made my research life so wonderful. First and foremost, I would like to express my gratitude towards my supervisor Prof. Shik Shin. Thanks to always having the best research environment, I was able to have a fulfilling research life. I would like to thank Prof. Kozo Okazaki for giving me advice about the interpretation of experimental data, writing papers, and handling of our laser ARPES system.

I would like to thank Dr. Yuichi Ota for supporting me handling the laser ARPES system. I would like to thank Prof. Takeshi Kondo for giving me chances to join beamtimes in synchrotron radiation facilities. I would like to thank Dr. Yukiaki Ishida for advice about measurements and research. I would like to thank Dr. Kenta Kuroda and Dr. Bareille Cédric for supporting measurements using synchrotron light sources. I would like to thank Dr. Toshiyuki Taniuchi and Dr. Peng Zhang for teaching me experience and knowledge about experiments. I would like to thank Dr. Takeshi Suzuki and Dr. Shunsuke Sakuragi for lots of advice and encouragements.

I am grateful to Prof. Yuji Matsuda, Dr. Shigeru Kasahara, Dr. Tatsuya Watashige, Prof. Takasada Shibauchi, Dr. Yuta Mizukami, and Dr. Kohei Matsuura for supplying high-quality single crystals of $FeSe_{1-x}S_x$. I am grateful to Dr. Takahiro Shimojima and Mr. Yuya Suzuki for teaching me the techniques of detwinning measurements. I am grateful to Prof. Masashi Tokunaga and Dr. Shiro Kawachi for supporting polarization microscope measurements. I am grateful to Prof. Chuangtian Chen for high-quality KBBF crystals and to Prof. Shuntaro Watanabe for the prism-coupling technique of KBBF crystals to produce 7 eV laser. I am grateful to Dr. Emile Rienks for supporting measurements in BESSY II. I am grateful to Prof. Hiroshi Kontani and Prof. Ryotaro Arita for fruitful discussions and comments.

I am indebted to members of Prof. Shin, Prof. Okazaki, and Prof. Kondo groups, for good times and support. I would like to thank Dr. Haruyoshi Yamamoto, Mr. Akihiro Tsuzuki, Mr. Tsubaki Nagashima, Mr. Sahand Najafzadeh, Dr. Weilu Zhang, and Mrs. Akiko Fukushima for supporting measurements. I would like to thank Dr. Takashi Yamamoto, Dr. Haruyoshi Yamamoto, Dr. Mitsuhiro Nakayama, Dr. Shuntaro Akebi, Dr. Hirohito Motoyui, Mr. Masaru Okada, Mr. Kairi Morozumi, Mr. Yu Ogawa, Mr. Junpei Kawakita, Mr. Ryo Noguchi, Mr. So Kunisada, Mr. Shoya Michimae, Mrs. Mari Watanabe, Mr. Daiki Matsumaru, Mr. Ren Qianhui, Mr Xu Jiadi, Mr. Yuji Okuda, Mr. Liu Kecheng, Dr. Walid Malaeb, and Dr. Tetsuro Shirasawa for encouragements.

I am grateful to Prof. Kozo Okazaki, Prof. Takasada Shibauchi, Prof. Kenichiro Hashimoto, Prof. Kyoko Ishizaka, and Prof. Tsuyoshi Kimura for productive comments as referees for this thesis. I am grateful to Prof. Kazushi Kanoda for giving me advice about research and career.

I would like to express my special thanks to Mrs. Sachiko Shinei and Mrs. Yoshie Kaneko for their help with paperwork.

I acknowledge the JSPS Research Fellowship for Young Scientists (DC2) and financial support from JSPS through the program for Leading Graduate School, MERIT (Materials Education Program for the Future Leaders in Research, Industry, and Technology).

Last but not least, I would like to thank my parents, and my sister, for personal and financial support during my graduate studies.